



FINAL REPORT

INVESTIGATION OF LIGHT HYDROCARBON FUELS WITH FLUORINE-OXYGEN MIXTURES AS LIQUID ROCKET PROPELLANTS

Prepared for
NATIONAL AERONAUTICS AND SPACE ADMINISTRATION
CONTRACT NAS3-10294

Pratt & Whitney Aircraft
FLORIDA RESEARCH AND DEVELOPMENT CENTER
BOX 2681, WEST PALM BEACH, FLORIDA 33402

DIVISION OF UNITED AIRCRAFT CORPORATION
**U
A[®]**

FINAL REPORT

INVESTIGATION OF LIGHT HYDROCARBON FUELS WITH FLUORINE-OXYGEN MIXTURES AS LIQUID ROCKET PROPELLANTS

Prepared for
NATIONAL AERONAUTICS AND SPACE ADMINISTRATION
CONTRACT NAS3-10294
15 NOVEMBER 1968

PRATT & WHITNEY AIRCRAFT
PROGRAM MANAGER
A. I. MASTERS

TECHNICAL MANAGEMENT
JOHN W. GREGORY
LIQUID ROCKET TECHNOLOGY BRANCH
NASA LEWIS RESEARCH CENTER
CLEVELAND, OHIO

Pratt & Whitney Aircraft
FLORIDA RESEARCH AND DEVELOPMENT CENTER

BOX 2691, WEST PALM BEACH, FLORIDA 33402

U
A_®
DIVISION OF UNITED AIRCRAFT CORPORATION

FOREWORD

This report was prepared by Pratt & Whitney Aircraft Division of United Aircraft Corporation under Contract NAS3-10294, "Investigation of Light Hydrocarbon Fuels with Fluorine-Oxygen Mixtures as Liquid Rocket Propellants." The contract was administered by the Lewis Research Center of the National Aeronautics and Space Administration, Cleveland, Ohio. This report is the final report on the subject contract and summarizes the technical work conducted during the period 30 June 1967 to 31 May 1968. The NASA Project Manager for the contract was Mr. John W. Gregory.

The following Applied Research personnel at Pratt & Whitney Aircraft's Florida Research and Development Center contributed to the technical effort and preparation of this report: A. I. Masters (Program Manager), and J. E. Colbert — program direction; P. A. Thomas and C. D. Baldwin — design and test; and W. R. Kaminski, J. E. Jackson, G. P. Beduerftig, M. L. Johnson, and A. P. Genchi — heat transfer analysis. In addition, many groups and individuals outside the Applied Research project group made contributions to the program, most notably: M. H. Staggs and R. H. Henson — test facility operations; and J. B. Anderson and J. R. Bush — analog simulation.

ABSTRACT

The feasibility of regeneratively cooling a flox-methane engine with bulk boiling methane was shown analytically and demonstrated experimentally. Both supplementary and regeneratively cooled simulated altitude tests were run at nominally 5000-lb thrust, 100-psia chamber pressure in modified RL10 tubular thrust chambers having nozzle expansion ratios of 40:1. The most severe cooling problems were determined and solutions to these problems investigated. Regenerative cooling applicability with bulk boiling methane was predicted with regard to thrust and chamber pressure limits. Performance data were obtained in 25 uncooled simulated altitude test firings with bell-shaped and conical nozzles.

CONTENTS

SECTION	PAGE
I INTRODUCTION	1
II SUMMARY	5
III TEST COMPONENT ANALYSIS AND DESIGN – TASK I.....	9
A. Design Requirements	9
B. Injectors	9
C. Uncooled Thrust Chambers and Exhaust Nozzle Extensions.....	13
D. Cooling Analysis and RL10 Chamber Modifications	14
IV TEST FACILITIES AND EQUIPMENT.....	41
A. Liquid Propellant Research Facility	41
B. Propellant Supply System	41
C. Control System	45
D. Instrumentation and Data Acquisition	46
V INJECTOR CHECKOUT TESTS – TASK II	49
A. Test Description	49
B. Test Performance	49
C. Heat Transfer	55
VI UNCOOLED ALTITUDE TESTING – TASK III.....	59
A. Test Description	59
B. Performance	59
VII REGENERATIVELY COOLED ALTITUDE TESTS	71
A. Test Description	71
B. Cooled Chamber Performance	75
C. Analysis of Cooling Results	80
VIII APPLICABILITY OF METHANE BULK BOILING COOLING – TASK I	87
A. Range of Conditions	87
B. Predicted Range of Applicability	88
IX REFERENCES	93
APPENDIX A	A-1

ILLUSTRATIONS

FIGURE		PAGE
1	Maximum Nucleate Boiling Heat Flux for Methane.....	2
2	Maximum Wall Temperature vs Heat Flux for Methane in Saturated Film Boiling	2
3	Sea Level Injector Performance	6
4	Flox/Methane Altitude Performance	7
5	Predicted Regenerative Cooling Limits	8
6	Tangential Entry Orifice Construction and Water Flows	10
7	Coaxial Injector	11
8	Triplet Injector	12
9	Uncooled Thrust Chamber Assemblies	13
10	Wall Temperature, Coolant Bulk Temperature, and Heat Flux for Mixture Ratio = 4.0	15
11	Wall Temperature, Coolant Bulk Temperature, and Heat Flux for Mixture Ratio = 4.75	16
12	Wall Temperature, Coolant Bulk Temperature, and Heat Flux for Mixture Ratio = 5.75	17
13	Tube Inserts in Throat Region	18
14	Location of Silver Filler Braze and Chamber Thermocouples	19
15	Coolant Density Change with Heat Addition	20
16	Effect of Heat Flux Variation on Coolant Distribution.....	21
17	Effect of Heat Flux and Coolant Flow Variations on Tube Wall Margin.....	22
18	Installation of Metering Orifice for Tube-to-Tube Flow Control.....	22
19	Effect of Metering Orifices on Jacket Flow Distribution.....	23
20	Influence of Carbon Deposition on Wall Temperature: RL10 Chamber with Tube Inserts.....	25
21	Influence of Supplementary-Cooling on Wall Temperature and Coolant Bulk Temperatures: RL10 Chamber with Tube Inserts.....	26
22	Distribution of Nodes for Analog Simulation.....	27
23	Enthalpy of Saturated Liquid Methane	33
24	Latent Heat of Vaporization for Methane.....	33
25	Density of Methane	34
26	Rate of Vapor Generation for Methane	35
27	Heat Exchanger Inlet and Outlet Mass Flux for Case 1.....	38
28	Heat Exchanger Inlet and Outlet Mass Flux for Case 2	38
29	Heat Exchanger Inlet and Outlet Mass Flux for Case 3.....	39
30	Heat Exchanger Inlet and Outlet Mass Flux for Case 5.....	39
31	Variation of Density with Time for Case 2.....	40
32	Variation of Wall Temperature and Quality with Time for Case 2.....	40
33	Schematic of Liquid Propellant Research Facility	42
34	Flox-Methane Test Stand Flow Schematic for Uncooled Tests.....	43
35	Flox-Methane Test Stand Flow Schematic for Supplementary-Cooled Tests	43
36	Flox/Methane Test Stand Flow Schematic for Regeneratively Cooled Tests	44
37	Engine Installation for Uncooled Sea Level Tests	49

ILLUSTRATIONS (Continued)

FIGURE		PAGE
38	Flox-Methane Characteristic Exhaust Velocity: 82.6% F_2 in Flox.....	53
39	Effect of Momentum Ratio for Coaxial Injectors	54
40	Predicted Coaxial Injector Performance	54
41	Comparison of Heat Transfer Coefficients, Test No. 2 USL, $r = 5.09$	55
42	Comparison of Heat Transfer Coefficients, Test No. 8 USL, $r = 5.63$	56
43	Triplet Injector – Facing Injector from Exit (Axial Plane 3 in. from Injector Face).....	56
44	Triplet Injector – Facing Injector from Exit (Axial Plane at Throat, $t = 3.5$)	57
45	Coaxial Injector – Facing Injector from Exit (Axial Plane 3 in. from Injector Face).....	57
46	Coaxial Injector – Facing Injector from Exit (Axial Plane at Throat)	58
47	Coaxial Injector – Characteristic Exhaust Velocity	64
48	Coaxial Injector – Vacuum Thrust Coefficient	65
49	Coaxial Injector – Vacuum Specific Impulse	66
50	Triplet Injector – Characteristic Exhaust Velocity	67
51	Triplet Injector – Vacuum Specific Impulse	68
52	Triplet Injector – Measured Vacuum Thrust Coefficient	69
53	Estimated Triplet Injector Vacuum Thrust Coefficient Based on Constant 95% η_c^* (Measured Coaxial Injector $\eta_c^* F_{vac}$ Included for Comparison).....	69
54	Post-Test View of RL10 Thrust Chamber.....	74
55	Characteristic Exhaust Velocity Data from Cooled Tests.....	75
56	Thrust Coefficient Data from Cooled Tests.....	78
57	Estimated Vacuum Specific Impulse Data from Cooled Tests.....	79
58	Predicted Regeneratively Cooled Chamber Condition Based on Measured Uncooled Test Heat Flux Profile, $r = 4.53$	81
59	Predicted Regeneratively Cooled Chamber Condition Based on Measured Uncooled Test Heat Flux Profile, $r = 5.65$	82
60	Effect of Carbon Flake-Off on Chamber Cooling, $r = 4.53$	83
61	Effect of Carbon Flake-Off on Chamber Cooling, $r = 5.65$	84
62	Predicted Start Transient Wall Temperature	85
63	Results of Parametric Heat Transfer Analysis: Chamber Pressure = 100 psia	89
64	Results of Parametric Heat Transfer Analysis: Chamber Pressure = 175 psia	90
65	Results of Parametric Heat Transfer Analysis: Chamber Pressure = 250 psia	91
66	Flox/Methane Regenerative Cooling Limits for Mixture Ratio of 5.75	92

TABLES

TABLE		PAGE
1	Summary of Cooled Tests	8
2	Injector Design Characteristics	12
3	Operating Conditions for the Heat Exchanger Nodes	28
4	Estimated Performance Data Accuracy	47
5	Measured Uncooled Sea Level Test Data	50
6	Calculated Performance Data for Uncooled Sea Level Tests	51
7	Injector Performance Comparison – Uncooled Sea Level Tests	52
8	Summary of Uncooled Altitude Tests	60
9	Calculated Performance Data for Uncooled Altitude Tests	61
10	Injector Performance Comparison for Uncooled Altitude Tests	62
11	Measured Cooled Altitude Test Data	76
12	Calculated Performance Data Cooled Altitude Tests	77
13	Range of Conditions for Parametric Study	87

NOMENCLATURE

A	Area	in ²
A _s	Heat transfer surface area	in ²
C	Capacitance	in ²
C _p	Specific heat at constant pressure	Btu/lb _m -°R
c*	Characteristic velocity	ft/sec
d	Diameter	in.
D _{eq}	Equivalent diameter	in.
f	Friction factor	
F	Thrust	lb _f
G	Coolant flowrate	lb _m /in ² -sec
g	Gravitational constant	lb _m -ft/lb _f -sec ²
h	Heat transfer coefficient	Btu/in ² -sec-°R
H	Enthalpy	Btu/lb _m
H _v	Latent heat of vaporization	Btu/lb _m
I	Fluid inertance	sec ² /in ²
I _s	Specific impulse	lb _f -sec/lb _m
I _{vac}	Vacuum specific impulse	lb _f -sec/lb _m
k	Thermal conductivity	Btu/hr-ft-°R
K	Fluid resistance w ΔP	lb _m -lb _f ^{1/2} /sec-in.
L	Length	in.
M	Tube-wall mass	lb _m
Nu	Nusselt number	
P	Pressure	lb/in ²
P _c	Chamber pressure	lb/in ²
Pr	Prandtl Number	
q	Heat flux to fluid	Btu/sec
Q	Heat flux to walls	Btu/sec
Q _m /Q _p	Heat flux reduction due to carbon deposition	
r	Mixture ratio (oxidizer-to-fuel) by weight	
Re	Reynolds number	
t	Time	sec
T	Temperature	°R
T _{abw}	Adiabatic wall temperature	°R
v	Specific volume	ft ³ /lb _m
V	Velocity	ft/sec
\dot{w}	Flowrate	lb/sec
x	Distance along coolant flow path	in.
X	Quality	
β	Rate of vapor generation	ft ³ /sec
η _c *	Characteristic velocity efficiency	
η _{cF}	Thrust coefficient efficiency	
η _{Ivac}	Vacuum specific impulse efficiency	
θ	Coolant bulk temperature	°R
μ	Viscosity	lb _m /ft-sec
ρ	Density	lb/ft ³

NOMENCLATURE (Continued)

Subscripts

amb	Ambient
b	Evaluated at coolant bulk temperature
bulk	Bulk fluid properties
c	Coolant side
cd	Discharge coefficient
cor	Corrected performance value
E	Coolant exit conditions
f	Fuel
F	Valves based on thrust
g	Combustion side
i	Evaluated at inlet to node
①	Average valve for node
in	Inlet conditions
j	Coolant jacket
m	Evaluated at mean film temperature, $T_f = \frac{1}{2}(T_{we} + \theta)$
o	Oxidizer
p	Total propellant flow
sat	Coolant saturation properties
sl	sea level
t	Tank conditions
v	Saturated vapor
vac	Vacuum conditions
w	Wall conditions

Superscript

/	Theoretical value
---	-------------------

SECTION I

INTRODUCTION

Analytical and experimental programs for "Investigation of Light Hydrocarbon Fuels with Fluorine-Oxygen Mixtures," have been conducted by Pratt & Whitney Aircraft under National Aeronautics and Space Administration Contracts NAS3-4195 and NAS3-6296 (References 1 and 2). The objective of these programs was to investigate the applicability of flox/light hydrocarbon propellant combinations to upper-stage pressure-fed engine applications. The major conclusions drawn from the work performed under these two contracts may be summarized as follows:

1. Flox/light hydrocarbon combinations provide high delivered vacuum specific impulse.
2. Flox/light hydrocarbon propellants have bulk densities comparable to other space-storable-propellant combinations.
3. Many of the flox/light hydrocarbon combinations have overlapping liquid ranges, thereby enhancing space storability.
4. For fluorine concentrations generally of interest to space storable applications, flox/hydrocarbon combinations will be hypergolic.
5. For low chamber pressure (nominally 100 psia), transpiration cooling has been shown to be feasible and attractive with methane, while regenerative cooling is applicable with a number of other light hydrocarbon fuels including propane, 1-butene, and a eutectic blend of pentane and isopentane.

With most fuels, the application of convective thrust chamber cooling at subcritical pressures is limited by the occurrence of film boiling and consequent high wall temperature. Film boiling is usually encountered in high heat flux areas, but also occurs at lower heat flux as the coolant approaches its saturation temperature. This trend is shown in figure 1 for methane (taken from Reference 1).

The narrow liquid range of methane limits its use as a liquid phase coolant, thus in most applications it must pass through the film-boiling regime. A sudden decrease in coolant-side film coefficient and associated increase in wall temperature occurs at the point where initiation of film boiling occurs. Beyond this point, coolant-side film coefficients increase as coolant velocity and Reynolds number increase. The wall temperature in this region is primarily a function of local heat flux and coolant velocity.

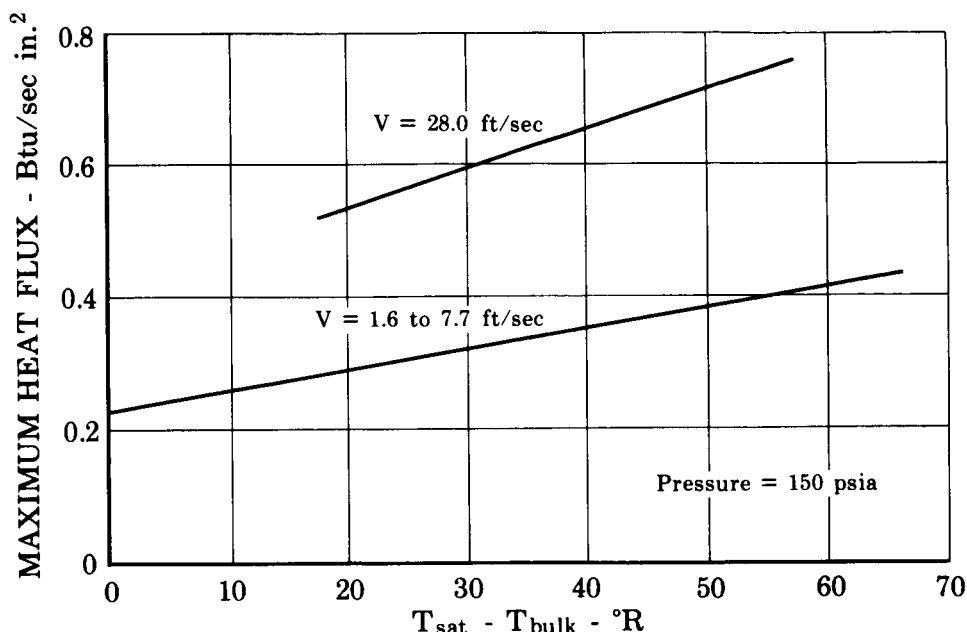


Figure 1. Maximum Nucleate Boiling Heat Flux
for Methane

FD 24929

Figure 2 shows the wall temperature at the point of initiation of film boiling as a function of local heat flux based on typical methane flow conditions. To maintain tolerable wall temperatures it is necessary to initiate film boiling at relatively low heat flux levels. Thus, the limited liquid heat capacity of methane becomes an asset by allowing vaporization to take place in the low heat flux regions of the nozzle. In this manner it is possible to maintain satisfactory wall temperatures throughout the entire thrust chamber by vaporizing the methane in the low heat flux region of the nozzle and by using high velocity gas to cool the high heat flux regions of the nozzle throat and combustion chamber.

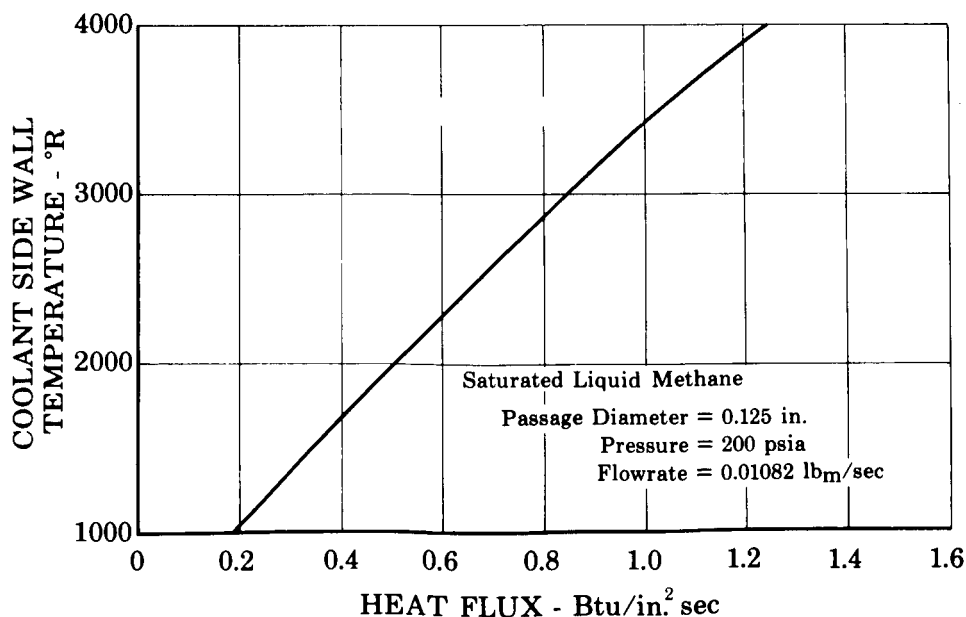


Figure 2. Maximum Wall Temperature vs Heat Flux
for Methane in Saturated Film Boiling

FD 24930

Another factor that increases the range of applicability of cooling with boiling methane is the heat flux reduction caused by carbon deposition on the chamber wall. Methane heat transfer data from previous test programs have produced chamber combustion-side film coefficients approximately 60 to 90% of theoretical predictions based on the Bartz boundary layer method (Reference 3). The lower values were determined under Contract NAS3-4195 from 100-psia thrust-chamber firings using modified RL10 (coaxial element) injectors with gaseous fuel (Reference 1), and the higher ratios were based on liquid-liquid testing with impinging type injectors (Reference 2).

When film or bulk boiling occur, fluid dynamic stability can be affected. The large changes in fluid density caused by heat addition in the boiling region, coupled with the dependence of coolant heat transfer on flowrate and velocity can result in divergent instability. In general, however, the pressure and volume perturbations at the point of boiling can be isolated from the system by employing various stabilizing devices. High differential pressure restrictions, such as orifices or cavitating venturis, upstream of the cooling jacket can be used to force a constant inlet flowrate. The compressibility of the gaseous coolant jacket outlet flow produces a stabilizing effect, which may be enhanced by increasing the line volume between the coolant jacket and the injector.

The primary objective of the work conducted under this program was to determine the feasibility of cooling a flox/methane engine with bulk-boiling methane. This was accomplished through an analytical and experimental investigation of steady-state heat transfer and dynamic stability. A secondary objective was to obtain additional altitude performance data with the flox/methane combination. The investigation was divided into three tasks. Task I, Methane Boiling Evaluation and Design, consisted of analysis and test hardware design, including detailed analysis of the range of applicability of regenerative cooling with boiling methane. Task II, Injector Checkout Tests, consisted of 5000-lb thrust, 100-psia chamber pressure, uncooled sea level firings with gaseous methane and liquid flox to determine baseline performance and circumferential heat flux. Task III, Methane Boiling Cooling Tests, consisted of simulated altitude testing to determine the exhaust nozzle heat flux and baseline performance, followed by 5000-lb thrust 100-psia chamber pressure simulated altitude firings in modified RL10 tubular thrust chambers to determine the requirements for satisfactory bulk-boiling cooling with fluid dynamic stability.

SECTION II

SUMMARY

Contract NAS3-10294 is the most recent of three "Investigations of Light Hydrocarbon Fuels with Fluorine-Oxygen Mixtures as Liquid Rocket Propellants" to be conducted by Pratt & Whitney Aircraft under the sponsorship of the NASA Lewis Research Center. Under the first two investigations, the feasibility of using light hydrocarbon fuels for transpiration cooling and conventional regenerative cooling at pressure-fed engine conditions was established. This report deals entirely with the third contract in the series.

The objective of Contract NAS3-10294 was to evaluate the feasibility of regenerative cooling with bulk-boiling methane. The term **bulk boiling** refers to vaporization of liquid methane in the low heat flux regions of the exhaust nozzle under predominantly film-boiling conditions. The high velocity gaseous methane produced in the nozzle is then used to cool the high heat flux regions of the combustion chamber. Secondary program objectives were to predict the range of applicability of bulk-boiling cooling and to obtain additional flox/methane performance data at simulated altitude conditions.

As with previous flox/light hydrocarbon programs, test conditions were nominally 5000-lb vacuum thrust and 100-psia chamber pressure. Liquid flox at the optimum theoretical concentration of 82.6% fluorine was used for all testing. Liquid methane at 180° to 200°R was used for thrust-chamber cooling and ambient gaseous methane was used as the fuel to simulate the coolant jacket outlet conditions in uncooled and supplementary-cooled tests.

Both coaxial and triplet injectors were tested. The coaxial injector had 145 elements, each with tangential entry swirlers to enhance atomization. The triplet injector had 133 elements, each having two oxidizer streams impinging on a central gaseous fuel stream. On both injectors the oxidizer orifices were nickel and a Rigimesh stainless steel faceplate contained the fuel orifices (or annuli) and provided transpiration cooling.

The characteristic velocity efficiency, η_c^* , of the two injectors was evaluated in uncooled sea level firings, the results of which are shown in figure 3. The triplet injector fulfilled one contract objective by achieving 95% η_c^* over most of the mixture ratio range of interest. Unfortunately, this injector yielded heat fluxes of approximately 100 to 120% of the theoretical heat flux as predicted by the Bartz boundary layer method. Values of 70 to 90% of the theoretical value had been predicted from the two previous programs, which indicated that carbon deposition would significantly reduce the heat flux, and heat fluxes of under 100% were deemed necessary for satisfactory cooling. The coaxial injector achieved

96% η_c^* at a mixture ratio of 4.3 and produced only 60 to 80% of the theoretical heat flux; however, the efficiency dropped off at higher mixture ratios. This low performance at high mixture ratio with the coaxial injector was partially expected because the fuel-to-oxidizer momentum ratios were below the design values, which were based on regenerative-cooling fuel injector inlet conditions. The addition of film-cooling holes in the triplet injector provided slightly lower heat flux, but in this configuration the injector exhibited unstable combustion. On this basis, the coaxial injector was selected for the initial cooled tests, while the triplet injector was selected for uncooled simulated altitude performance testing.

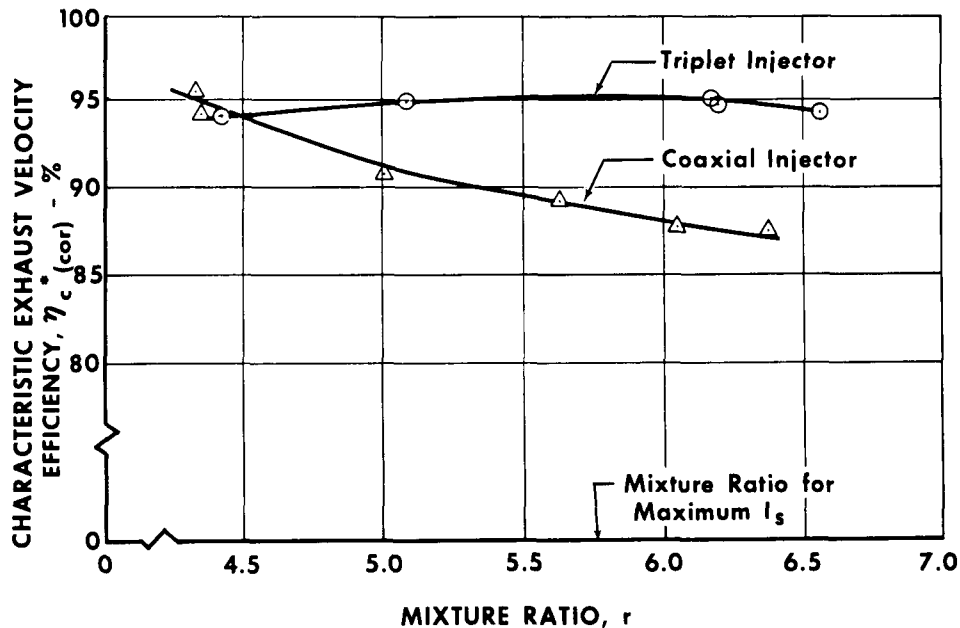


Figure 3. Sea Level Injector Performance

GS 7933A

Twenty-one uncooled simulated altitude firings were conducted with the triplet injector, twelve using a bell nozzle having the same geometry as the RL10 engine, and nine with a 15-deg conical nozzle. Both configurations provided nozzle expansion ratios of 40. Vacuum specific impulses of approximately 380 seconds were obtained at a mixture ratio of 4.1 as shown in figure 4. Acoustic instability in these tests prevented accurate determination of η_c^* ; however, an estimated η_c^* of 95% based on the sea level data provides thrust coefficients that are consistent with other stable data obtained on this contract and previously under Contract NAS3-6296 (Reference 2). Three significant conclusions may be drawn from these data. First, nozzle expansion losses due to nonequilibrium expansion are considerably less than theoretical predictions, i.e., less than 3% below $r = 4.5$ compared to nonequilibrium predictions of 5%, and less than 6% at $r = 5.75$ compared to predicted losses of 10%. (Predicted kinetic losses are taken from Reference 2). Second, the experimental vacuum specific impulse peaks below a mixture ratio of 5.0 even though η_c^* is constant with mixture ratio. Third, conical nozzles provide a 1 to 2% performance improvement at high mixture ratios, but little increase in the peak vacuum specific impulse.

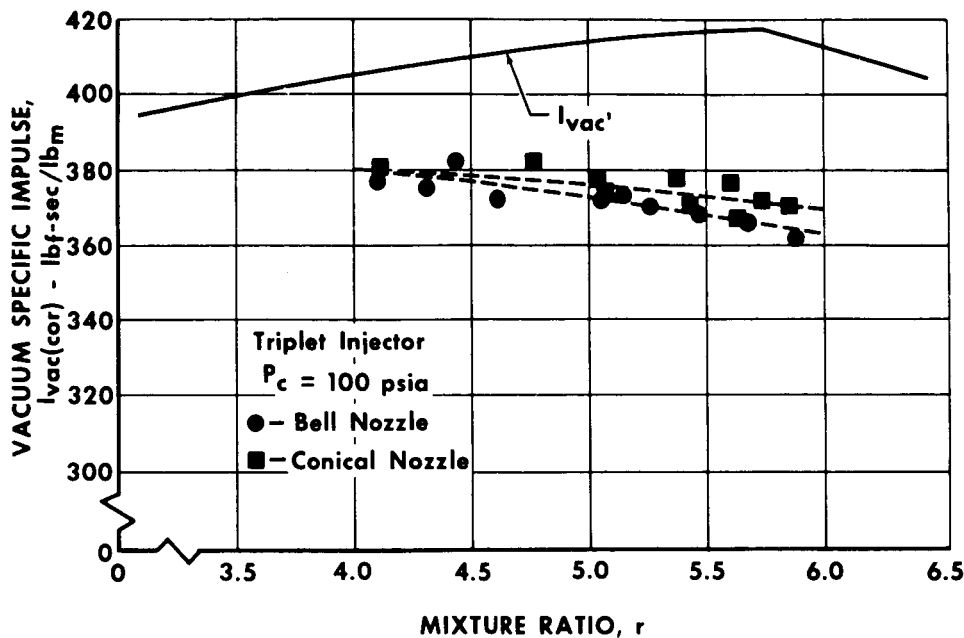


Figure 4. Flox/Methane Altitude Performance

GS 7934

Using modified RL10 tubular thrust chambers, four supplementary and three regeneratively cooled tests were conducted using liquid-methane cooling at bulk-boiling conditions. The test results are summarized in table 1. Coolant pressure surges occurred in tests No. 1 CA and 5 CA caused by a drastic change in the coolant density during the engine start. This problem was overcome by lengthening and carefully controlling the start transient. On tests No. 2 CA, 3 CA, 4 CA, and 6 CA successful bulk-boiling cooling was demonstrated; however, on tests No. 4 CA and 6 CA minor chamber damage was encountered at the higher mixture ratios run at the end of the test. It was concluded that this damage was probably caused by carbon flakeoff at high mixture ratios, which temporarily caused local hot spots. No instances of fluid dynamic instability were encountered in any of the cooled tests. Completely satisfactory bulk-boiling cooling was demonstrated below a mixture ratio of 5.0, which, as previously indicated, was found to be the region of interest based on maximum experimental performance.

The use of individual metering orifices in the coolant jacket tubes was found to be extremely useful, not only in controlling coolant distribution during steady-state operation, but also in limiting chamber damage when a tube failure occurs. Damage sustained during tests No. 2 CA, 4 CA, and 6 CA was minimized and readily repaired. The more severe damage incurred during the start transient on test No. 7 CA did not progress after steady-state conditions were obtained. Without the metering orifices, catastrophic failures would probably have occurred on all of these tests.

TABLE 1. SUMMARY OF COOLED TESTS

Test No.	Type Cooling	Test Duration, sec	Coolant Flow, lb/sec	Mixture Ratio	Results
1 CA	Supplementary	2	-	-	Shutdown at start; repairable tube damage
2 CA	Supplementary	20	3.0	4.3	Successful
3 CA	Supplementary	20	3.0	4.0-5.5	Successful
4 CA	Supplementary	30	2.2	4.0-5.5	Repairable tube damage
5 CA	Regenerative	9	-	-	Shutdown at start; no damage
6 CA	Regenerative	40	2.4-2.2	4.6-5.0	Repairable tube damage
7 CA	Regenerative	60	2.4-2.2	4.0-5.0	Burnout at start

In addition to the experimental program, a study was conducted to determine the limits of applicability of bulk-boiling methane with regard to chamber pressure and thrust. The results are summarized in figure 5. Based on rather conservative assumptions regarding tubular thrust chamber construction, a lower limit of approximately 2000-lb thrust at 100-psia chamber pressure was found.

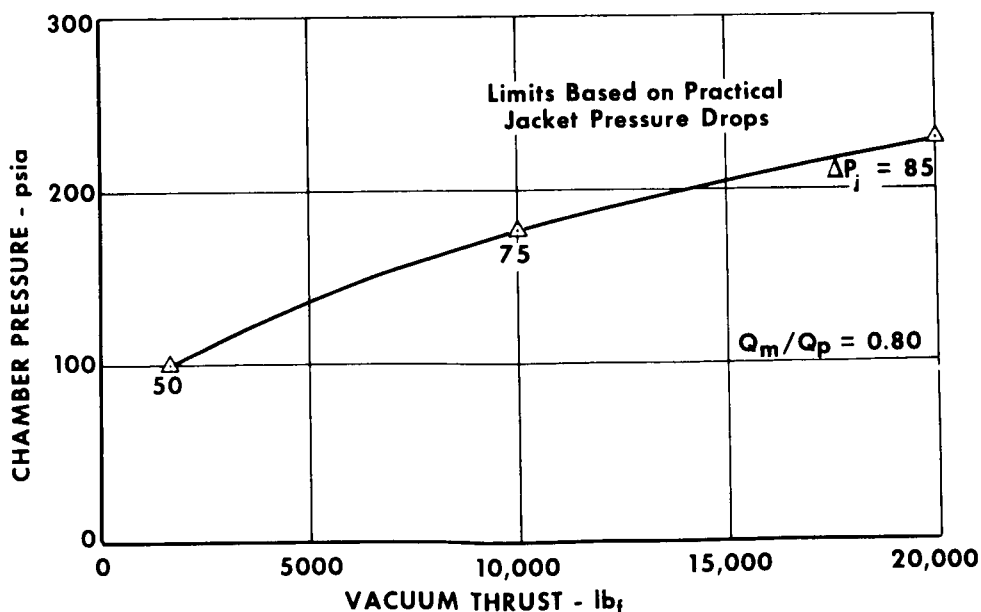


Figure 5. Predicted Regenerative Cooling Limits

GS 7942A

SECTION III

TEST COMPONENT ANALYSIS AND DESIGN — TASK I

A. DESIGN REQUIREMENTS

Nominal design conditions for all test hardware were 100-psia chamber pressure and 5000-lb vacuum thrust based on a nozzle expansion ratio of 40. A flox concentration of 82.6% fluorine was used throughout the study. Injector designs were based on an oxidizer inlet temperature of 160° to 180°R and a methane inlet temperature of 525°R for uncooled and supplementary-cooled tests and 550° to 700°R for regeneratively cooled tests. Thrust chamber cooling was based on a methane inlet temperature of 180° to 200°R.

Solid copper thrust chambers and stainless steel nozzle extensions, initially fabricated and tested under Contracts NAS3-4195 and NAS3-6296, were used for the uncooled firings. One chamber-bell-nozzle assembly provided the same internal geometry as the RL10 oxygen-hydrogen engine, while a second assembly had the same combustion chamber geometry and a 15-deg conical exhaust nozzle. The injectors and the cooled thrust chamber were modifications of RL10 engine components.

B. INJECTORS

The primary goals in selection of the injector configurations were achievement of 95% η_c^* at a mixture ratio of 5.75 with stable combustion and uniform circumferential heat flux. Two element configurations were selected: (1) a coaxial design with tangential entry oxidizer swirlers, and (2) a crossed-fan triplet having two oxidizer streams impinging on a central fuel stream. This selection was based on the results of three previous NASA contracted flox/light hydrocarbon programs (References 1, 2, and 4), and a Company-sponsored flox/butene-1 injector test program (Reference 5).

The coaxial injector was selected because all previous experimental data with flox/gaseous methane had been obtained with this type of element. These data indicated that straight coaxial jets would only marginally provide the 95% η_c^* required, but that use of oxidizer swirlers could provide significant increases in efficiency. It was therefore considered necessary to utilize oxidizer swirlers to ensure meeting the performance objectives. Higher performance was found with 216-element injectors than with the 108-element injectors tested under Contract NAS3-4195; however, the swaging techniques required to achieve high-injection momentum ratios with the higher elements density led to problems with hardware durability at high mixture ratio. On this basis, it was decided to use the maximum number of elements that would provide reasonable fuel annulus dimensions without swaging. It was considered necessary to maintain a fuel annulus gap of over 0.007 to 0.008 in. to prevent uneven fuel distribution caused by unavoidable manufacturing tolerance limitations. The final design had 145 elements with a resulting annulus 0.008 in. wide.

Because of durability problems encountered with previous flox/methane coaxial injectors using ribbon swirlers, a tangential entry oxidizer swirler design was selected. This unique design consisted of slots, electro-discharge-machined into the back of the injector divider plate. Figure 6 shows the construction details of a test element having the same internal dimensions as those in the injector. Three slots are drilled tangentially to each oxidizer orifice and the orifice is then closed with a spot weld. A shallow slot angle causes the slot exit area to be the controlling area, and requires only that the depth of penetration and not the weld size be uniform. The swirl elements produce a conical spray with a 30-degree included angle. The elements were designed for a pressure drop of 25 psi at a mixture ratio of 5.75. Experience with both ribbon and tangential entry swirlers indicated that a 30-degree spray angle provides a desirable compromise between adequate droplet breakup and prevention of wall impingement. In figure 6 the flow from the tangential entry swirler is compared with that produced by a straight orifice of the same diameter. The cone angle is primarily a function of the ratio of slot to orifice area and does not change appreciably with pressure drop as shown in figure 6. The calculated mean drop size for this element is 135 microns. Based on vaporization criteria (Reference 6), this corresponds to an effective length of 12.2 in. or approximately twice that required for essentially complete vaporization. The coaxial injector is shown in figure 7.

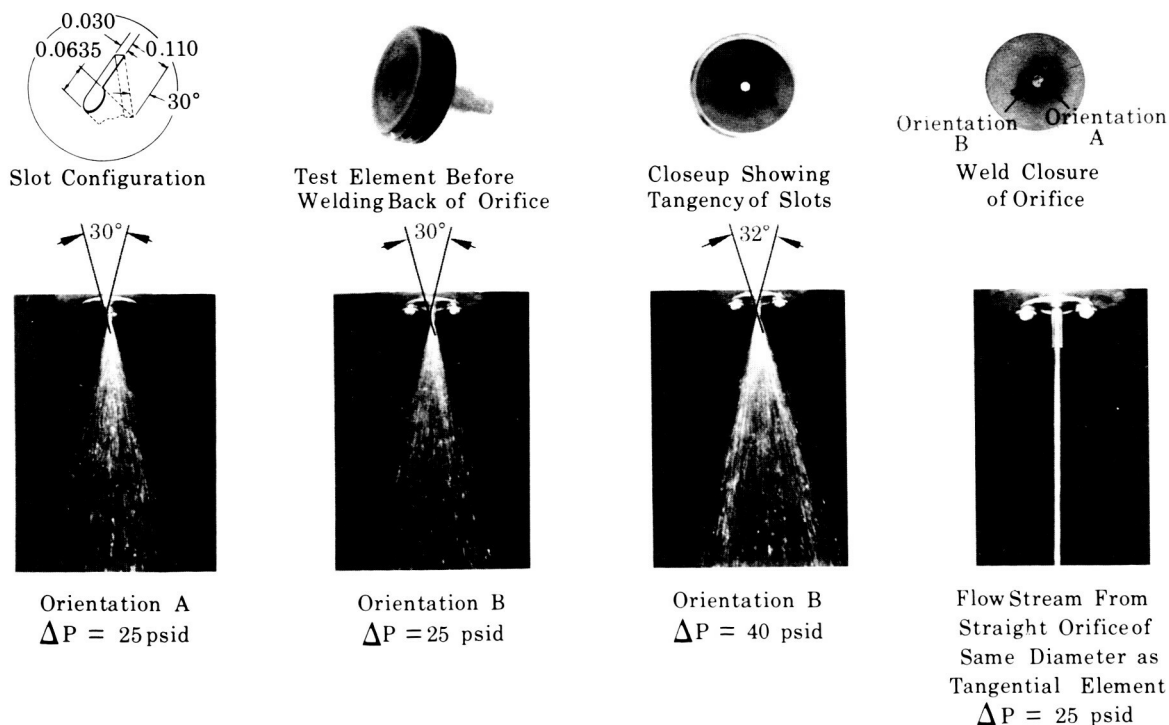


Figure 6. Tangential Entry Orifice Construction and Water Flows

FD 22502A

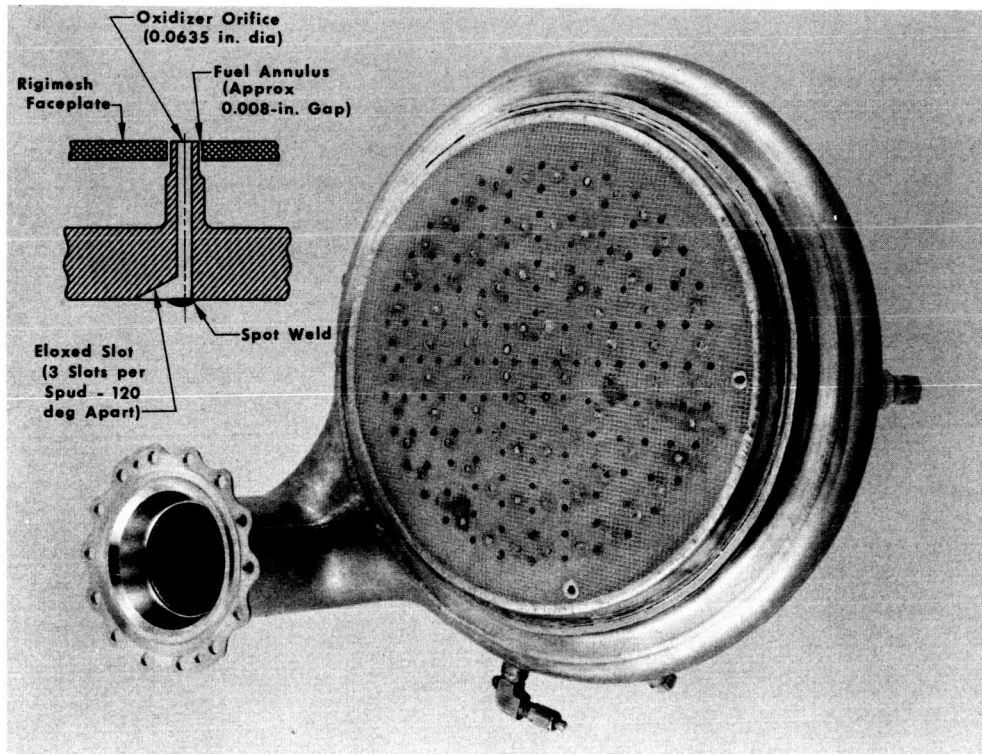


Figure 7. Coaxial Injector

GS 7930

The second injector design was based on the use of triplet elements, i.e., two liquid oxidizer streams impinging on a central gaseous fuel stream. Selection of the triplet was based on high performance with other propellant combinations at gas-liquid injection conditions. A Company-sponsored flox/butene-1 injector performance comparison of triplet injectors with parallel impingement fans and perpendicular fans showed that at approximately the same momentum ratios and mixture ratios the perpendicular fan injector produced higher performance with less than half as many elements because of the increased interelement mixing caused by the fan circulation.

The triplet injector, shown in figure 8, had 133 elements, the approximate maximum based on the geometry, fluid dynamic, and manufacturing restraints imposed by the design requirements. To minimize circumferential heat flux variations, the outer row of the injector consisted of 36 elements oriented to provide an outer ring canted 10 deg away from the wall. The included angle between the oxidizer streams was 90 deg and the impingement point was 0.225 in. from the injector face. Effective length estimates for the injector were 25 in. neglecting secondary atomization by the gaseous fuel, more than adequate to assure essentially complete vaporization.

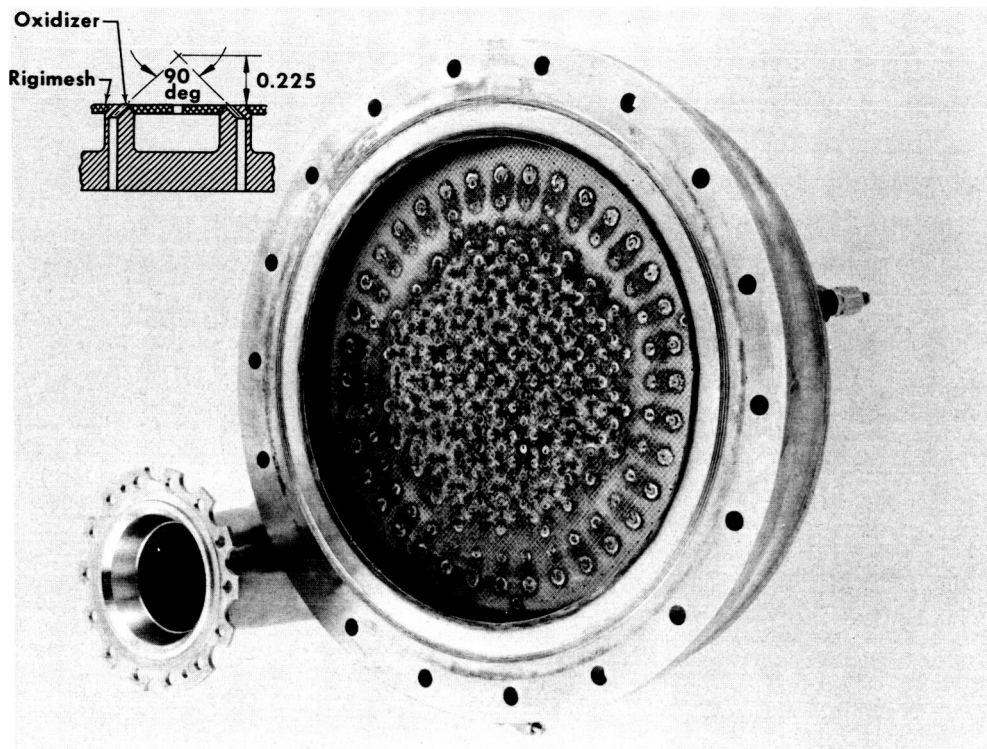


Figure 8. Triplet Injector

GS 7931

Both injectors utilized nickel oxidizer plates that were machined and drilled to form the oxidizer orifices and stainless steel Rigimesh faceplates that provided transpiration cooling and contained the fuel orifices (or annuli). The principal element dimensions and operational pressure drops for the two injectors are summarized in table 2.

TABLE 2. INJECTOR DESIGN CHARACTERISTICS

Element Pattern	Number of Elements	d_o , in.	d_f , in.	Mixture Ratio	ΔP_o , psi	ΔP_f ,* psi	Momentum Ratio
Concentric	145	0.0635	0.146**	5.75	25	60	4.1
				4.00	23	105	5.8
Triplet	133	0.0490	0.074	5.75	20	65	4.6
				4.00	18	118	6.4

*Based on ambient temperature methane
 **0.008-in. annulus width

C. UNCOOLED THRUST CHAMBERS AND EXHAUST NOZZLE EXTENSIONS

Two uncooled copper thrust chamber configurations were used for sea level injector checkout testing (Task II) and uncooled simulated altitude testing (Task III). The sea level injector checkout testing was conducted using a solid copper chamber having a 15-deg nozzle half-angle, with an area ratio of 1.98 to ensure under-expansion at 100-psia chamber pressure. The altitude testing used both (1) a bell-nozzle configuration, i.e., copper chamber and stainless steel RL10 contour exhaust nozzle extension, and (2) the copper chamber used for sea level testing with a 15-deg conical exhaust nozzle extension. The two altitude assemblies are shown in figure 9.



Figure 9. Uncooled Thrust Chamber Assemblies

GS 7932

The two uncooled thrust chamber assemblies were previously fabricated and tested under Contracts NAS3-4195 and NAS3-6296 and required only minor modification of the injector flange and addition of a flange to the exit plane of the bell-nozzle chamber to mount the nozzle extension for altitude testing. Modifications to the exhaust nozzle extensions were not required.

Instrumentation of the 15-deg thrust chamber consisted of 27 chromel-alumel (CA) thermocouples located axially along the chamber and 45 CA thermocouples located circumferentially around the chamber in three separate planes: 18 in a plane 3 in. from the injector face, 12 in a plane 5.85 in. from the injector face, and 15 at the throat plane. A high frequency pressure transducer was installed approximately 2 in. from the

injector face. The bell-nozzle chamber had 10 chromel-alumel thermocouples located axially and 26 more located circumferentially in two separate planes: 18 in a plane 3 in. from the injector face and 8 in the throat plane. The bell-nozzle-extension instrumentation consisted of 12 axial and 8 circumferential chromel-alumel thermocouples. The circumferential thermocouples were located in a plane 9 in. from the throat. No thermocouples were used on the conical nozzle extension.

Installation of the thermocouples was accomplished by cutting grooves in the outer surface of the chamber, placing the thermocouple wires in the grooves and peening in place, thus forming a junction. The junction was then flame-sprayed with copper to ensure good thermal conduction. The entire chamber was wrapped with an insulating blanket covered with fiberglass for protection.

D. COOLING ANALYSIS AND RL10 CHAMBER MODIFICATIONS

1. STEADY STATE

The following parameters were considered in the heat transfer analysis of the RL10A-3-1 chamber to be tested under Task III:

Chamber Pressure	100 psia
Mixture Ratio	4.0, 4.75, and 5.75
Fuel Flowrate	2.66, 2.31, and 1.95 lb/sec
Coolant Flowrate	1 and 2 times fuel-flowrate
Heat Transfer Reduction Due to Carbon Deposition (Q_m/Q_p)	0.6, 0.8, and 1.0

Analysis of the unmodified RL10A-3 chamber, at 80% of the Bartz heat flux, indicated that local wall temperatures would be very near the burnout wall temperature at some of the required operating conditions. Wall temperature, coolant bulk temperature, and heat flux are shown in figures 10, 11, and 12 for mixture ratios of 4.0, 4.75, and 5.75, respectively. To increase the heat transfer to the methane coolant, thereby reducing wall temperatures, wire inserts were placed in the tubes to reduce the flow cross-sectional area. These tube inserts were in the form of copper wires extending from the turnaround manifold to the exit manifold. Several wire sizes were investigated. The selected configuration was of varying blockage produced by 2, 3, and 4 strands of 0.032-in. diameter (No. 20) wire twisted together as shown in figure 13.

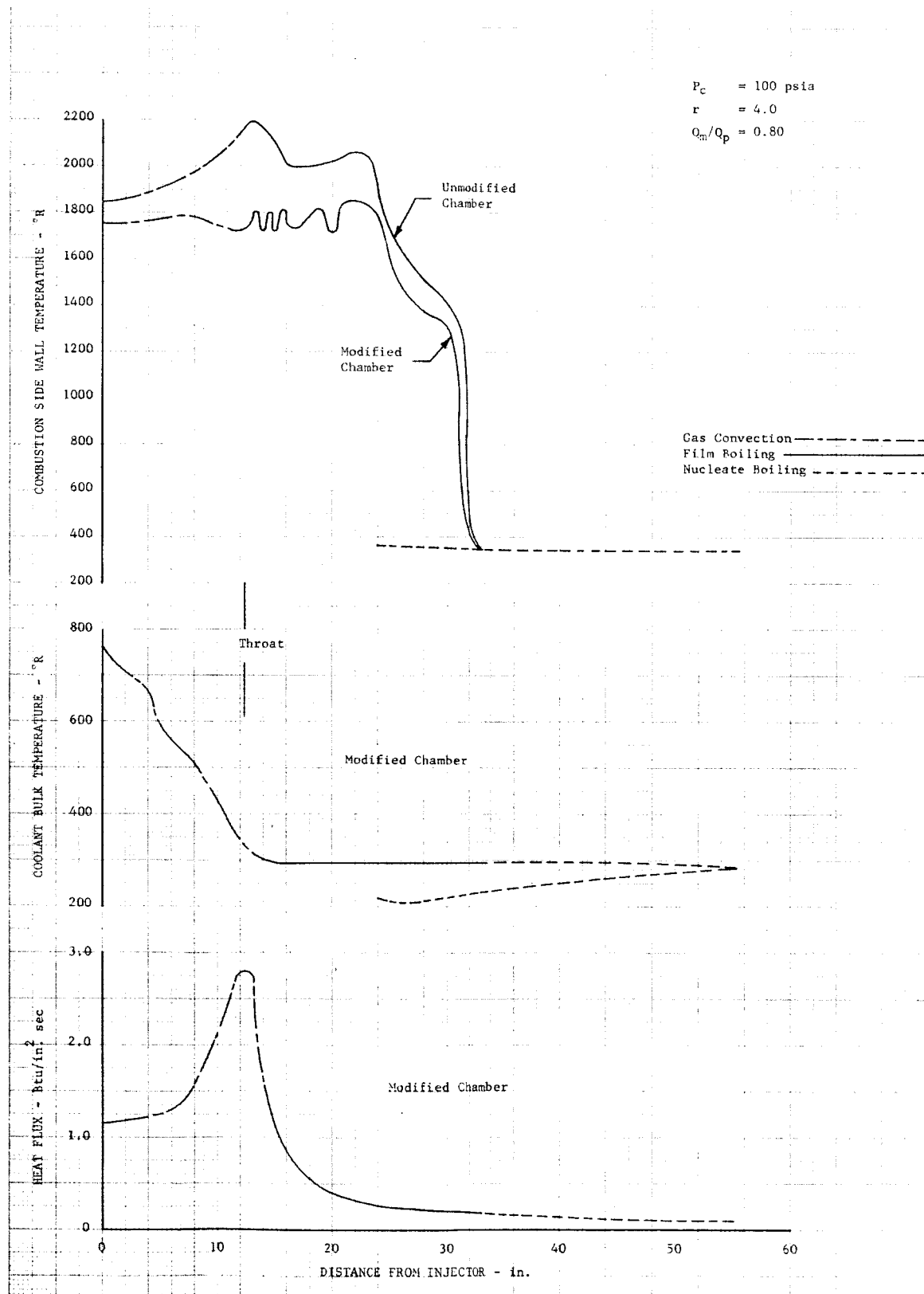


Figure 10. Wall Temperature, Coolant Bulk Temperature, and Heat Flux for Mixture Ratio = 4.0

DF 66867

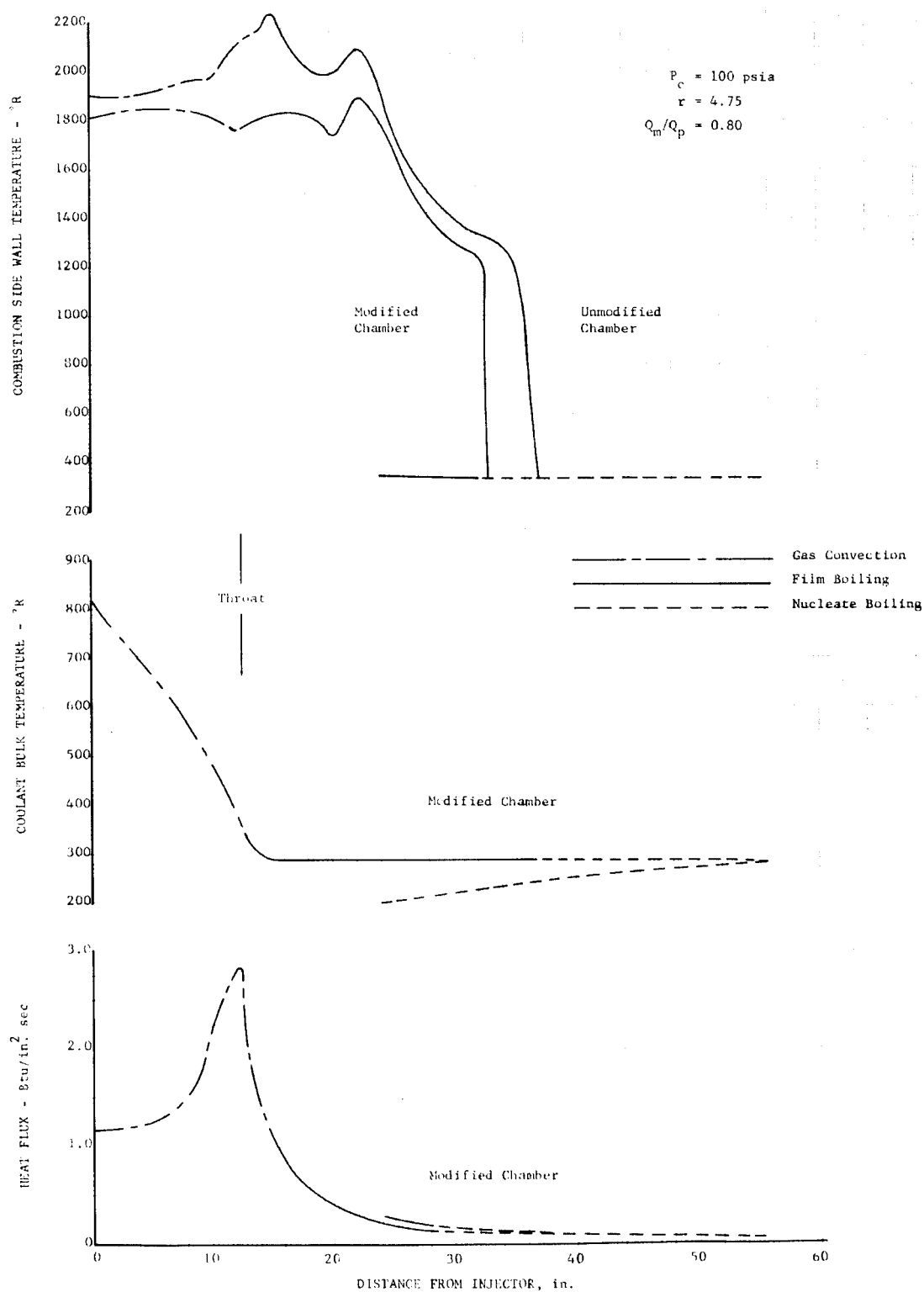


Figure 11. Wall Temperature, Coolant Bulk Temperature, and Heat Flux for Mixture Ratio = 4.75

DF 66868

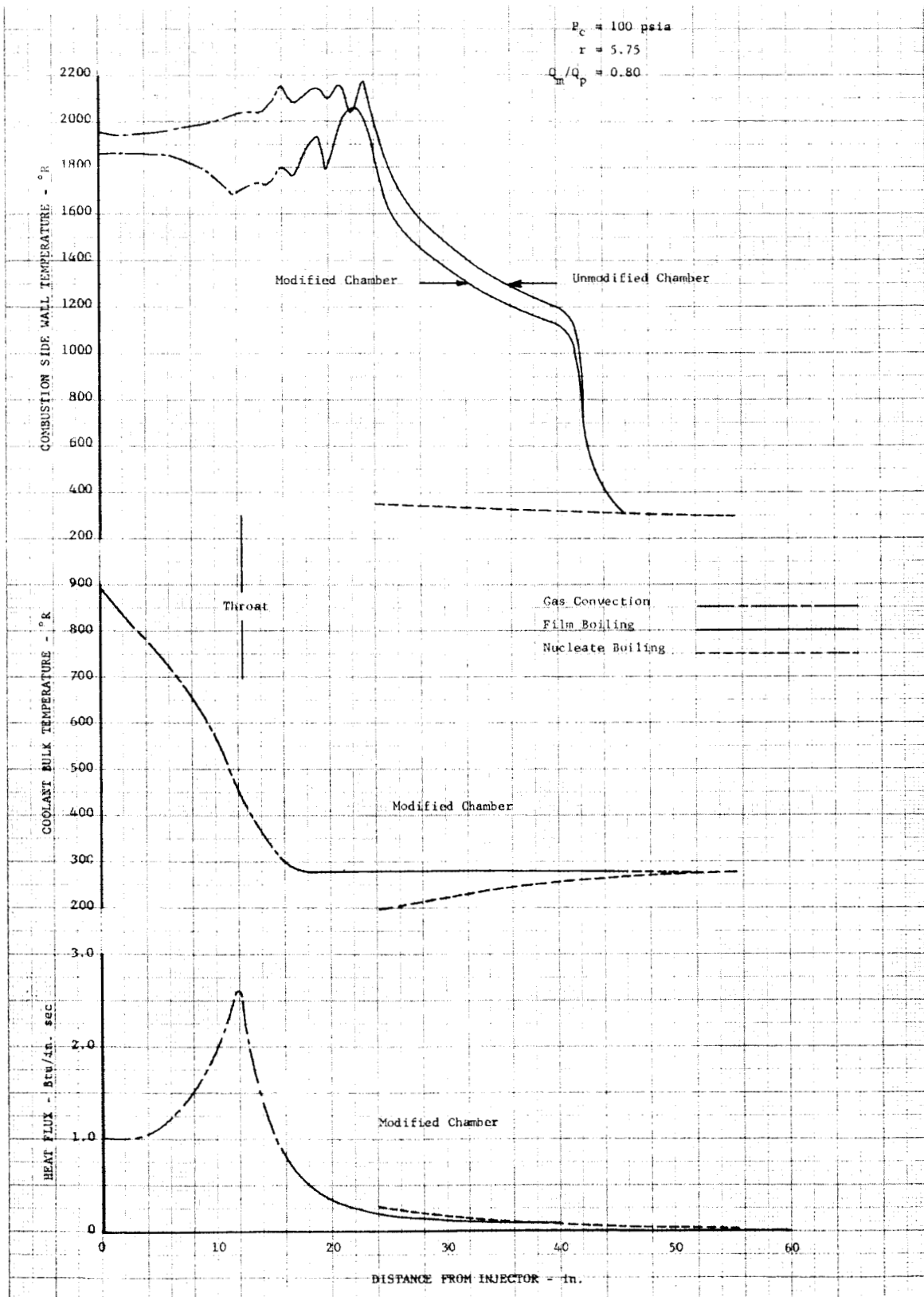


Figure 12. Wall Temperature, Coolant Bulk Temperature, and Heat Flux for Mixture Ratio = 5.75

DF 66869

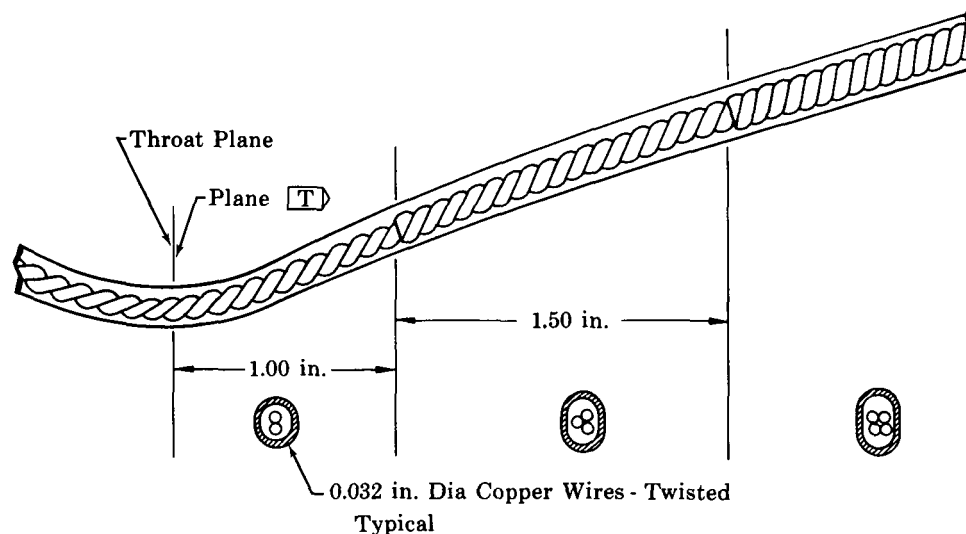


Figure 13. Tube Inserts in Throat Region

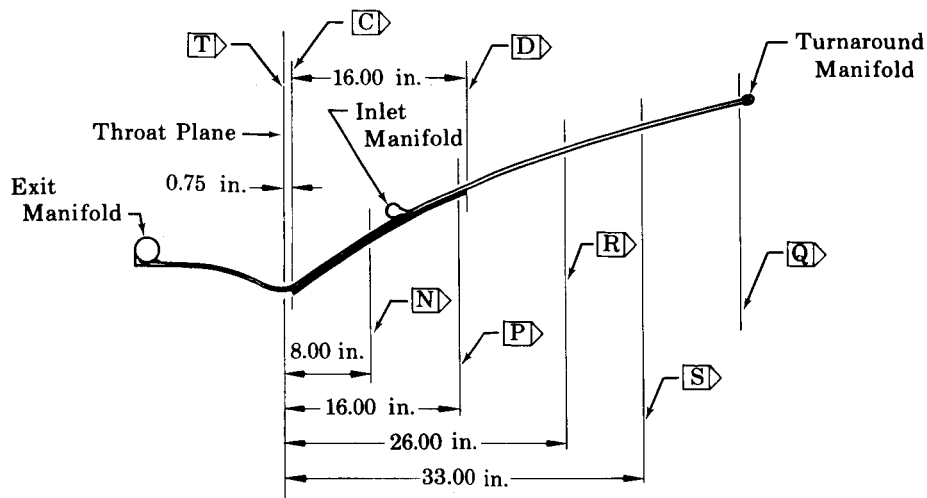
FD 24931

Reductions in wall temperature of as much as 400°R were realized in the regions of maximum wall temperature. The various modes of heat transfer occurring in the coolant passages are indicated by the different types of lines on figures 10 through 12. As shown in these figures, the point of complete vaporization shifts downstream from the injector with increasing mixture ratio. This may be explained by noting that as the mixture ratio is increased from 4.0 to 5.75 the total heat load to the chamber remains essentially constant, while the coolant flowrate decreases. Thus, the heat absorption per pound of coolant is greater for the higher mixture ratio cases and causes the point of complete vaporization to occur earlier. The location of the point of complete vaporization relative to the injector face as a function of mixture ratio is shown below (the throat is at 12 in.).

Mixture Ratio	Location of Point of Complete Vaporization From Injector Face, in.
4.0	14
4.75	15
5.75	17

Because the coolant flow in the long tubes is away from the turnaround manifold, friction and momentum forces held the insert in tension by attaching the inserts at the turnaround manifold. The opposite end of the inserts (at the exit manifold) "float" free, thus eliminating possible kinking or stressing due to unequal thermal expansion.

In addition to the wire swirls, a silver filler braze was added to the troughs between tubes in the predicted region of high temperature film boiling to provide additional cooling margin. The braze provided increased wall temperature margin by increasing conduction away from the tube crowns and into the trough areas. As shown in figure 14, the braze covered the area from about 0.75 to 17 in. downstream of the throat.



- Notes: ① Plane [Q] Contains Bulk T/C (Short Tubes).
 ② Planes [N], [P], [R], and [S] Contain Hot Wall T/C's (Long Tubes).
 ③ Lithium Silver Braze Between Planes [C] and [D].

Figure 14. Location of Silver Filler Braze and Chamber Thermocouples

FD 24932

Also shown in figure 14 are the locations of twelve hot wall temperature and two coolant bulk temperature thermocouples in two planes approximately 120 deg apart. The coolant bulk temperature measurements taken in the short tubes allowed estimation of the heat flux level at that plane.

In addition to the modifications to reduce the tube wall temperature, metering orifices, inserted in the chamber to provide uniform coolant flow to each tube, were added to the chamber inlet manifold. The requirement for this modification arises from the potentially large tube-to-tube coolant flow variation caused by nonuniform circumferential heat flux. The problem is particularly severe with bulk-boiling methane because of the large density decrease that occurs at the vaporization point. Figure 15 compares the density change of methane and supercritical pressure hydrogen for varying amounts of heat addition. Due to the density decrease of methane, most of the coolant pressure drop is taken after the point of vaporization. Any change in heat flux thereby displaces the vaporization region and results in a change in the coolant pressure drop. For the modified test chamber operating at a nominal mixture ratio of 5.75 and 80% of the Bartz heat flux, figure 16 shows that a $\pm 10\%$ circumferential heat flux variation results in a $\pm 50\%$ variation in tube-to-tube coolant flow for a given jacket differential pressure. (Note that the jacket differential pressure must be essentially the same because the tubes are connected to common manifolds.)

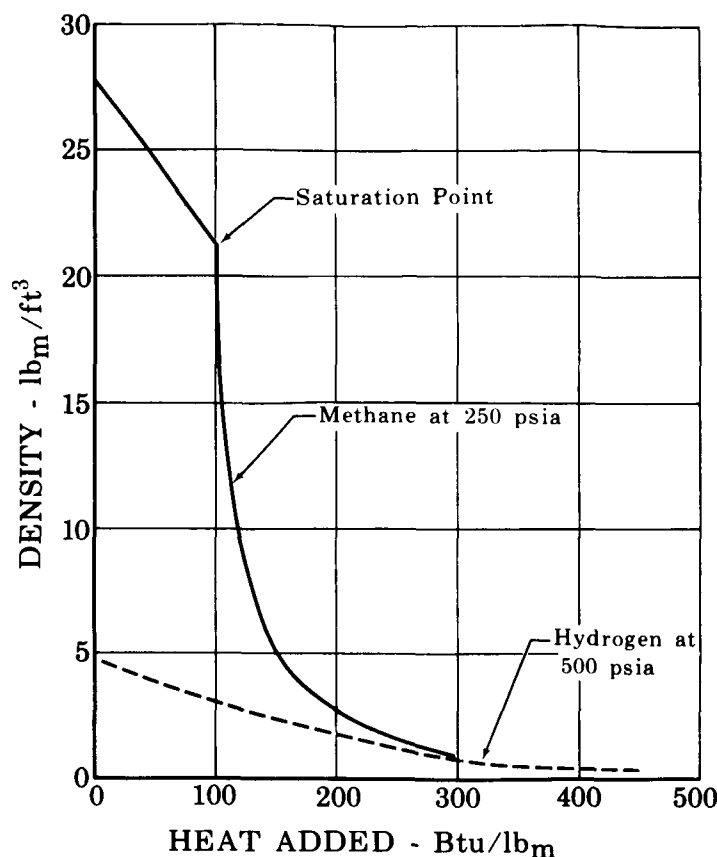


Figure 15. Coolant Density Change With Heat Addition

FD 23591

For comparison, the bottom curve in figure 16 shows the same heat flux-flow relationship for a fluorine/hydrogen RL10 operating with supercritical pressure (no boiling) hydrogen coolant. In this case a $\pm 10\%$ change in heat flux results in only a $\pm 2\%$ variation in coolant flow. The relative stability of the supercritical pressure hydrogen system occurs because there are no large changes in hydrogen density.

Unfortunately, higher heat fluxes reduce the coolant flow; this is opposite to the desired result of higher flows in the higher heat flux regions. Because of this effect, small circumferential heat flux variations have a relatively large effect on tube wall temperature. The term "tube wall margin" is defined as the difference between the temperature at which the tube would burst and the calculated tube hot wall temperature. Figure 17 shows the variation in tube wall margin that results from the $\pm 10\%$ heat flux variation indicated by the X's in figure 16. At the 90% heat flux point, the flowrate is reduced to 75% of nominal and the tube wall margin is reduced to 150°R. Based on uniform coolant distribution, for 100% of the Bartz heat flux the minimum tube wall margin would be approximately 200°R. Thus, the secondary effect of reduced coolant flow has a greater effect on wall cooling margin than the primary effect of nonuniform circumferential heat flux.

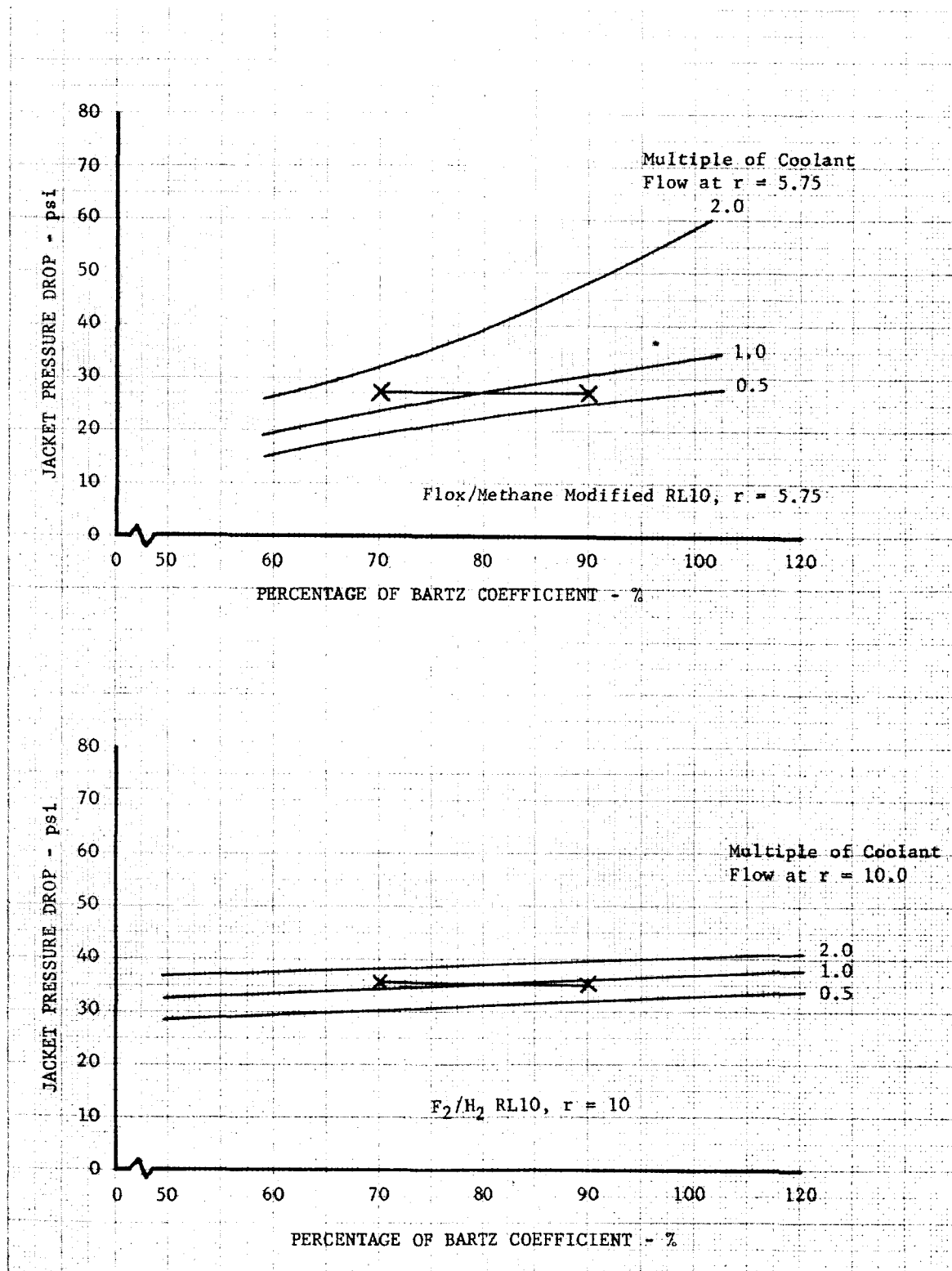


Figure 16. Effect of Heat Flux Variation on Coolant Distribution

DF 66870

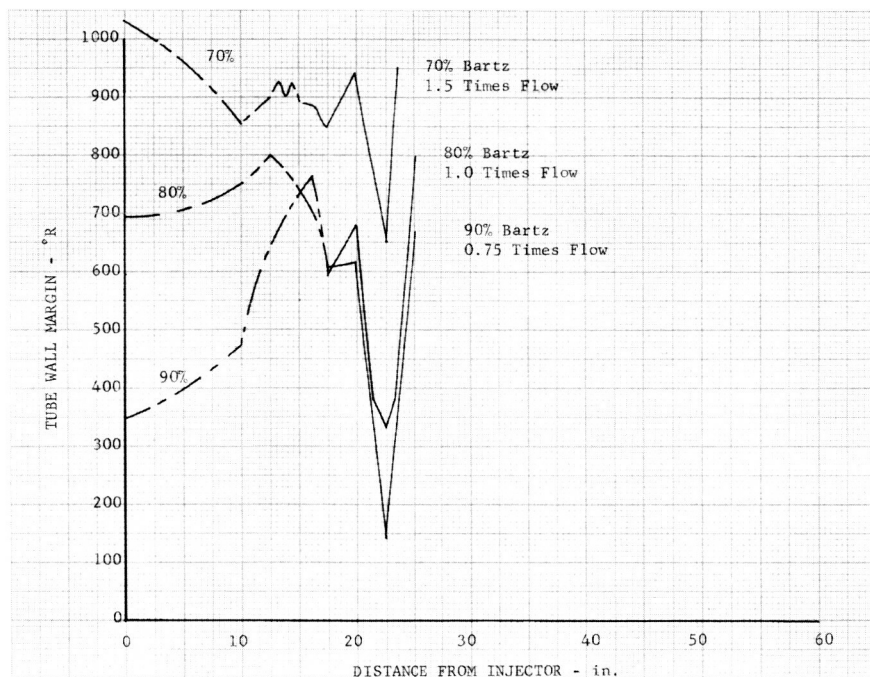


Figure 17. Effect of Heat Flux and Coolant Flow Variations on Tube Wall Margin

DF 66871

To overcome this problem, metering orifices were used to reduce the dependency of flow on pressure perturbations in the tubes produced by non-uniform circumferential heat flux. Figure 18 shows the installation of the metering orifices. The orifices are placed in each of the 180 short tubes and flow separators are inserted into the turnaround manifold so that the flow from each short tube is routed to its adjacent long tube. The photo-insert in figure 18 shows the completed turnaround manifold. Orifices of 0.031-in. diameter were used to limit the coolant flow to $\pm 10\%$ as shown in figure 19.

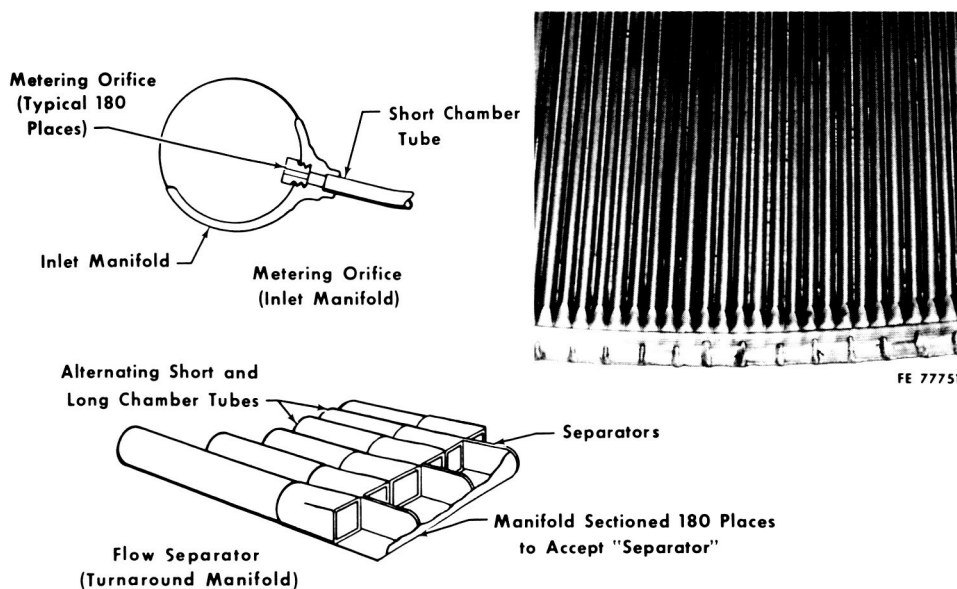


Figure 18. Installation of Metering Orifice for Tube-to-Tube Flow Control

GS 7939

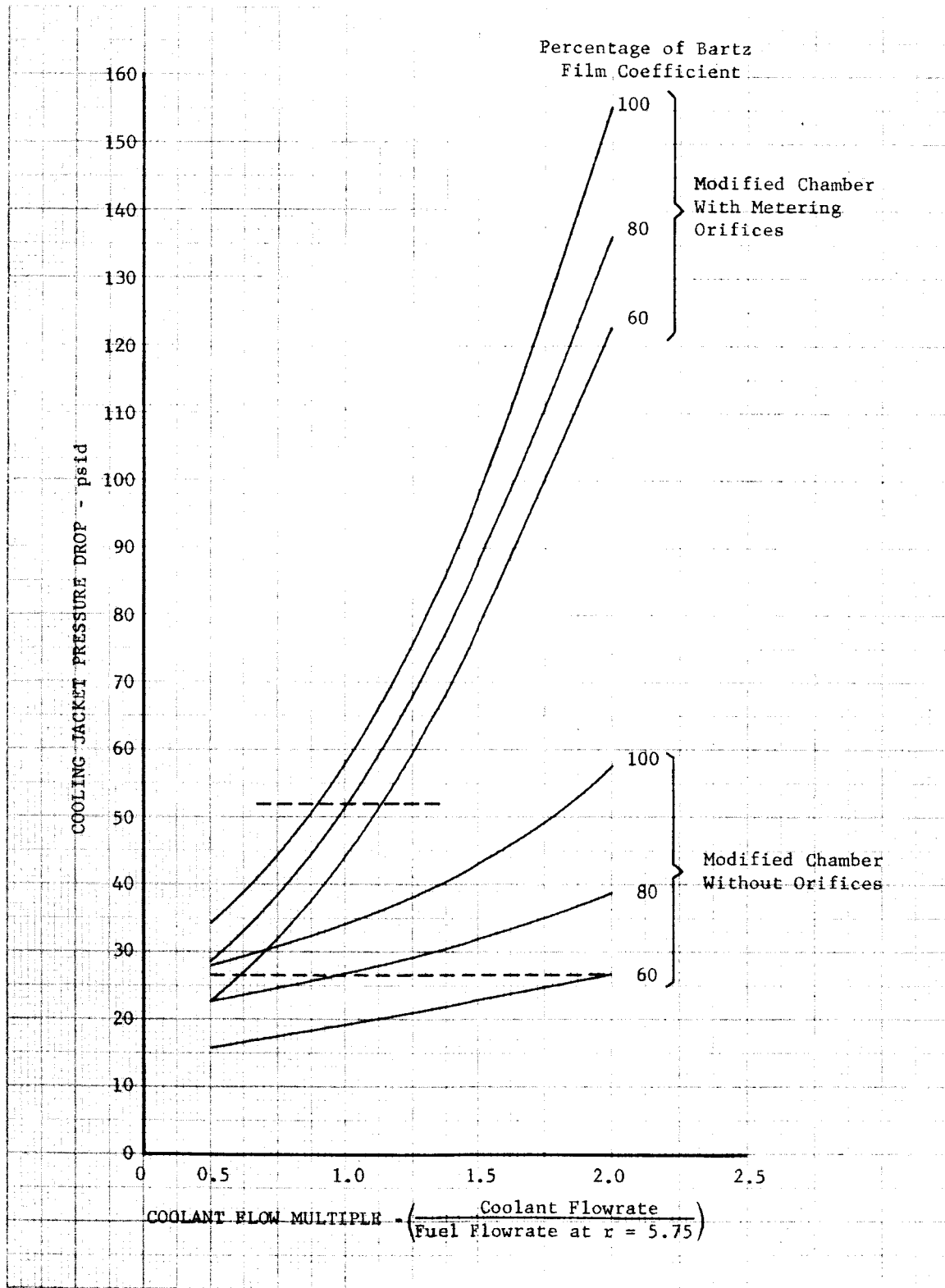


Figure 19. Effect of Metering Orifices on Jacket Flow Distribution

DF 66872

Variation in heat transfer rates due to carbon deposition on the combustion chamber walls was investigated for values of the parameter Q_m/Q_p of 0.6, 0.8, and 1.0 for mixture ratios of 4.0 and 5.75. As indicated in figure 20, the maximum wall temperature increases approximately 250°R in going from 80 to 100% of the theoretical heat flux. The location of the point of complete vaporization is influenced by carbon deposition through a change in total heat transferred to the coolant. This point shifts from 13.8 to 20.9 in. from the injector for a change in Q_m/Q_p from 60 to 100% for the 5.75 mixture ratio case, and from 11.4 to 17.4 in. for the 4.0 mixture ratio case.

The desirability of using high coolant flowrates during the supplementary-cooled tests was investigated for coolant flows up to twice the injector fuel flow. Increasing the jacket coolant flow above the chamber fuel flow decreases the wall temperature in the throat region. Doubling the coolant flowrate reduced the wall temperature by as much as 250°R in the highest wall temperature regions for the regenerative case at a mixture ratio of 5.75, as shown in figure 21. With the increased coolant flowrate the heat absorption per pound of coolant is decreased and the location of complete vaporization of the coolant occurs much later, e.g., the location of complete vaporization moves from a point 17 in. from the injector to a point 8 in. from the injector when the coolant flowrate is doubled. Because the point of transition to film boiling now occurs in a high heat flux region, the wall temperature increase at the transition point is approximately twice that for the regenerative cooling flowrate. In addition, a high temperature region occurs in the chamber area because the point at which gas convection cooling begins has also been moved to a higher heat flux area. Thus, overcooling may not always provide the increased cooling margin that is desired, but for this case a slight benefit was found for overcooling up to twice the injector fuel flow.

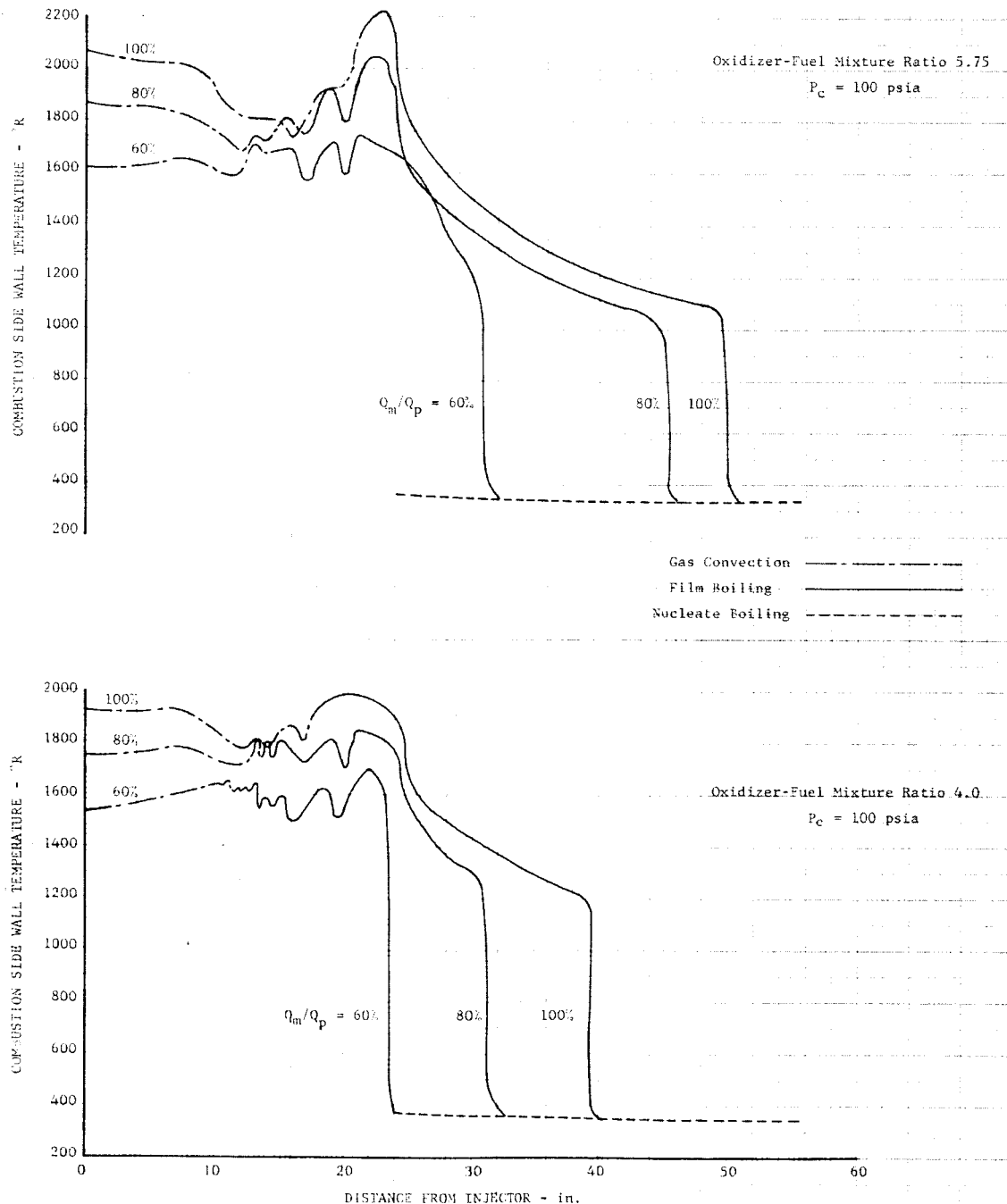


Figure 20. Influence of Carbon Deposition on Wall Temperature: RL10 Chamber With Tube Inserts

DF 66873

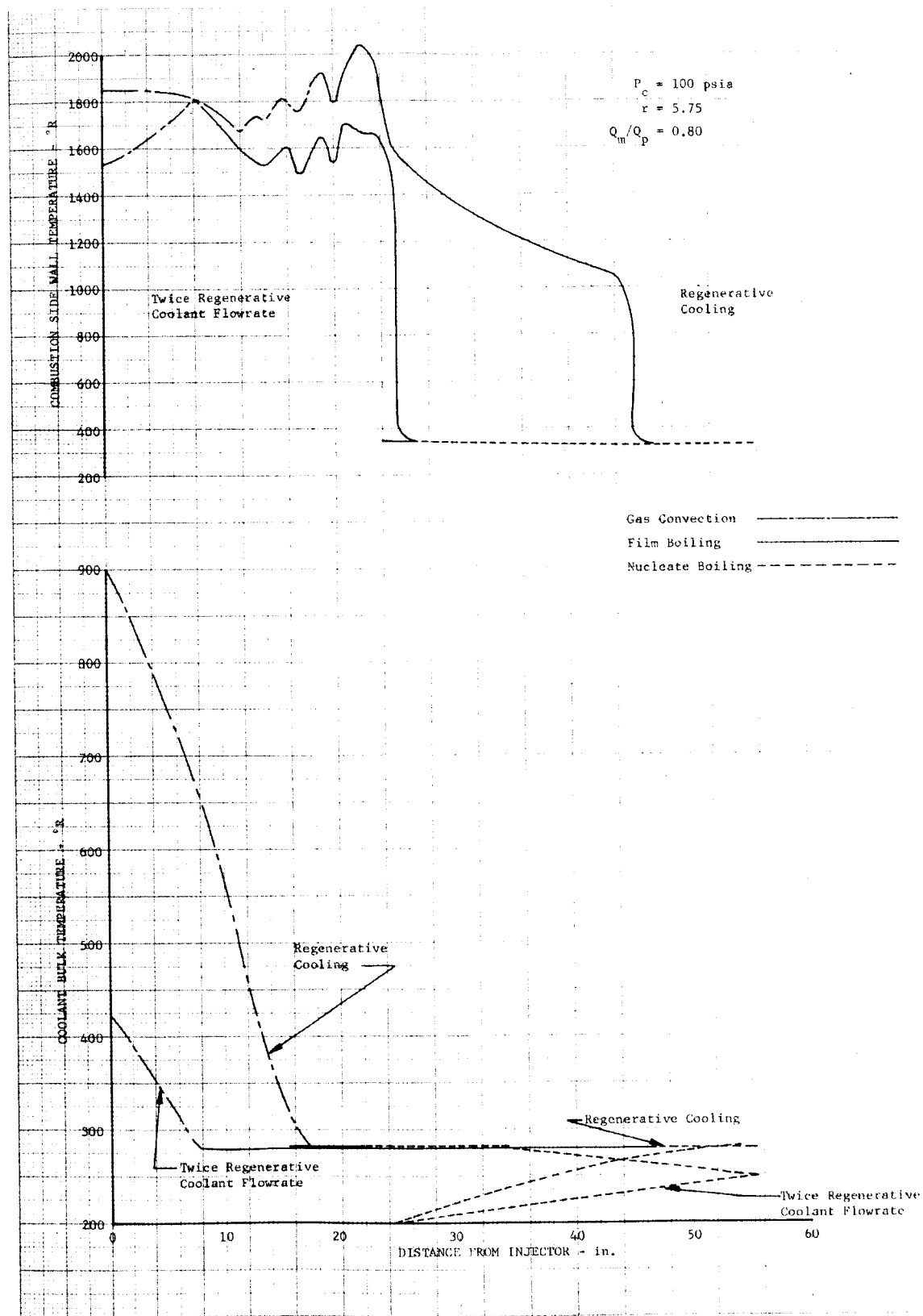


Figure 21. Influence of Supplementary-Cooling on Wall Temperature and Coolant Bulk Temperatures: RL10 Chamber With Tube Inserts

DF 66874

2. FLUID DYNAMIC STABILITY – ANALOG SIMULATION

A dynamic simulation of bulk-boiling methane in an RL10 heat exchanger was made using a Beckman 2133 analog computer. The purpose of the analog study was to (1) determine if the basic heat exchanger is stable, (2) isolate the problem area if it is not stable and (3) determine those methods that will stabilize the heat exchanger. The analysis employed in the analog program was similar to that reported in Reference 7 with the exception that the methane properties and boiling heat transfer correlations of Reference 1 were incorporated. The heat exchanger was represented by an 8-node system as shown in figure 22. The inlet and outlet stand plumbing were represented by lumping equivalent capacitances (volume effects), inertances (fluid accelerations), and resistances in series. Although the tube inserts discussed in paragraph D-1 affect the level of steady-state values (wall temperature, etc.) they were not expected to influence the dynamics of the system appreciably and were not included.

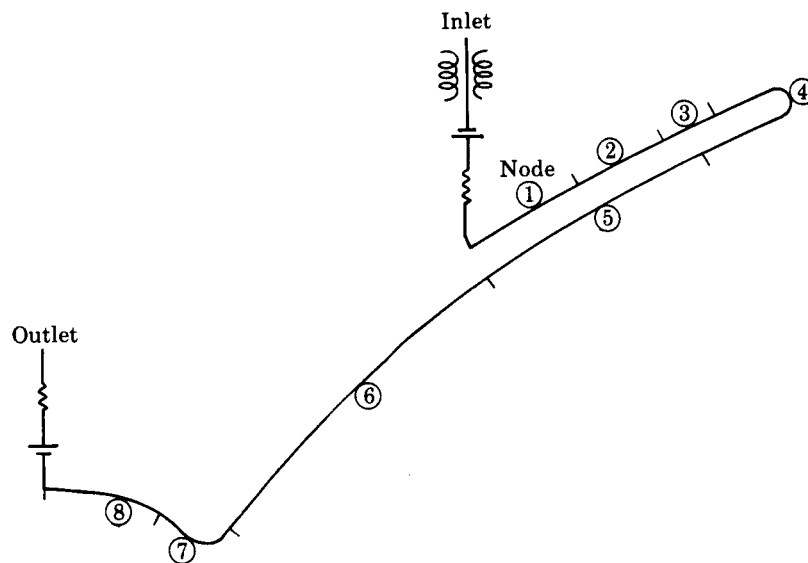


Figure 22. Distribution of Nodes for Analog Simulation

FD 24933

The steady-state density ratio across each node was restricted to a maximum value of two. This restriction, combined with the necessity of using the available analog equipment most efficiently, resulted in the decision to use 8 nodes. Based on the steady-state analysis, several heat transfer correlations were required to cover the possible flow regimes in each node. The possible operating conditions programed for each node are shown in table 3.

TABLE 3. OPERATING CONDITIONS FOR THE
HEAT EXCHANGER NODES

Node	Conditions Covered in Analog Program
1	Nucleate boiling, no net vapor generation
2	Nucleate boiling, no net vapor generation
3	Nucleate, subcooled, or saturated film boiling
4	Nucleate, subcooled, or saturated film boiling
5	Nucleate, subcooled, or saturated film boiling
6	Nucleate, subcooled, or saturated film boiling and superheated gas convection
7	Superheated gas convection
8	Superheated gas convection

Inlet and outlet line dynamics are represented by the following equations:

1. Inlet

$$\frac{dG_{in}}{dt} = \frac{144}{A_{in} I_{in}} (P_T - P_{in})$$

$$\frac{dP_{in}}{dt} = \frac{1}{144} \left(\frac{A_{in}}{G_{in}} \right) G_{in} - \left(\frac{A_1}{C_{in}} \right) \left(\frac{180}{144} \right) G_1$$

$$P_1 = P_{in} - \left[\frac{A_1}{K_{in}} \right]^2 G_1^2$$

2. Outlet

$$\frac{dP_9}{dt} = \left(\frac{180}{144} \right) \left(\frac{A_9}{C_E} \right) G_9 - \left(\frac{1}{C_E} \right) W_E$$

$$W_E = K_E \sqrt{P_9 - P_{amb}}$$

Values of capacitance, inertance, and resistance for the lines are effective values that represent the accumulative effect of the various sections of the plumbing.

The equations governing the heat input to the fluid are the same as those used in the steady-state analysis,

$$q = A s_c h_c (T_{wc} - \theta) \quad \text{Superheated Gas Convection}$$

$$q = A s_c h_c (T_{wc} - T_{sat}) \quad \text{Film Boiling (Subcooled and Saturated)}$$

$$T_{wc} = T_{sat} + 50^\circ \quad \text{Nucleate Boiling}$$

$$h_c = \left[\frac{0.023}{D_{eq}^{0.2}} \left(\frac{C_p}{\mu} \right)_f^{0.4} (K_f)^{0.6} \left(\frac{\rho_f}{\rho_b} \right)^{0.8} \right] G^{0.8} \quad \text{For Superheated Gas Convection}$$

$$h_c = 15.03 \left[\frac{0.023}{D_{eq}^{0.2}} \left(\frac{C_p}{\mu} \right)_f^{0.4} (K_f)^{0.6} \left(\frac{\rho_f}{\rho_b} \right)^{0.8} \right] G^{0.8} \left(\frac{\rho_b}{\rho_f} - 1 \right)^{0.72} \left(\frac{q}{H \ell_v A s_c} \right)^{0.72} \quad \text{For Subcooled Film Boiling}$$

$$h_c = \left[\frac{0.023}{D_{eq}^{0.2}} \left(\frac{C_p}{\mu} \right)_f^{0.4} (K_f)^{0.6} \left(\frac{\rho_f}{\rho_b} \right)^{0.8} \right] G^{0.8} \left(\frac{\rho_b}{\rho_v} \right)^{0.5}$$

For Saturated Film Boiling

Previous experience based on the work done in Reference 3 indicates that heat storage in the walls is not a significant factor for the first 5 nodes. This analysis treats heat storage in the walls for nodes 6 through 8 only.

Heat storage in the walls is calculated as the difference between the heat flux to the wall, Q , and the heat flux to the fluid, q , which are defined as follows:

$$Q_i = \left[(h_g A s_g T_{adw})_{(i)} - (h_g A s_g T_{wg})_{(i)} \right]$$

$$q_i = A s_{ci} h_{ci} (T_{wc} - T_{sat})_i \quad 0 \leq x \leq 1$$

$$q_i = A s_{ci} h_{ci} (T_{wc} - \theta)_i \quad x > 1$$

This results in a wall energy balance equation as follows:

$$\frac{dT_w}{dt} = \frac{1}{MC_p} (Q - q)$$

It was assumed that density varied linearly with distance in each node. The rate of change of density was then:

$$\frac{d\rho_i}{dt} = \frac{1}{L_i} (G_i - G_{(i+1)})$$

and further,

$$\rho_{(i+1)} = 2\rho_i - \rho_{i-1}$$

The variations from the assumption of a linear distribution of density were small, and resulted in a negligible effect on the solution.

The primary effect of heat addition to the fluid is an increase in fluid volume. A simplified form of the energy equation that accounts for the volume effect is obtained by combining the first law of thermodynamics, property relations, and continuity. It was necessary to assume a quasi-steady flow process. Properties that are independent of pressure changes are evaluated at the heat exchanger inlet pressure. The latter assumption is reasonable because steady-state analysis indicates small pressure losses.

First Law of Thermodynamics,

$$dq = \dot{W} dH$$

Property Relation,

$$\rho = \rho(H, p)$$

$$d\rho = \left. \frac{\partial \rho}{\partial H} \right|_P dH + \left. \frac{\partial \rho}{\partial P} \right|_H dP$$

Continuity,

$$\dot{W} = \rho AV$$

$$d\dot{W} = 0 = AV d\rho + \rho d(VA)$$

Substitution of the first two equations into the continuity equation yields the desired differential equation.

$$d\left(\frac{GA}{\rho}\right) = -\frac{1}{\rho^2} \frac{\partial \rho}{\partial H} \bigg|_P dq = \frac{\partial v}{\partial H} \bigg|_P dq$$

The nature of the analog simulation requires that the energy equation provides a means for calculating the flow rate per unit area from node to node. In finite difference form this gives:

$$G_{i+1} = \frac{\rho_{i+1}}{A_{i+1}} \left(\frac{\beta_i + \beta_{i+1}}{2} \right) + \frac{\rho_{i+1}}{\rho_i} \left(\frac{A_i}{A_{i+1}} \right) G_i .$$

An exact form of the momentum equation requires accounting for all factors such as friction and turning losses, as well as heat addition, throughout each node.

The basic momentum equation:

$$\frac{dP}{dx} = - \underbrace{\frac{4\bar{f}}{D_{eq}} \frac{1}{2g} \rho V^2}_{\text{friction}} - \underbrace{\frac{\rho V}{g} \frac{dv}{dx}}_{\text{heat addition}} - \underbrace{\frac{1}{A} \frac{dw}{dt}}_{\text{acceleration}}$$

is rearranged and then modified with the assumptions:

1. Friction and momentum pressure losses for each node are proportional to the inlet velocity head for each node.
2. Flow accelerations are proportional to the unbalanced pressure forces, dp/dx .
3. The pressure drop in nodes 1 through 5 is so small in the steady-state analysis that it is assumed negligible.

The form of the momentum equation used is:

$$\frac{dG_i}{dt} = C_{uo}(P_1 - P_9) - C_{u1}\left(\frac{G_1^2}{\rho_1}\right) - C_{u6}\left(\frac{G_6^2}{\rho_6}\right) - C_{u7}\left(\frac{G_7^2}{\rho_7}\right) - C_{u8}\left(\frac{G_8^2}{\rho_8}\right) - C_{u9}\left(\frac{G_9^2}{\rho_9}\right)$$

where the effective inertance may be expressed as:

$$C_{uo} = g / \left[A_1 \sum_i (L/A) + 180 A_1 (L_{in}/A_{in}) \right]$$

$$C_{ui} = C_{uo} (\Delta P_i / (G_i^2 / \rho_i)) 144 \text{ for } 1 \leq i \leq 9$$

and C_{ui} is non-zero because the inlet manifold pressure drop is included for the pressure drop in node 1.

Methane thermodynamic properties were normalized to simplify the curves as necessary to fit the analog capability. Figures 23 and 24 show the saturated liquid enthalpy and the latent heat of vaporization. These are used to determine the vapor quality and the vapor density. The pressure, temperature, density relationship is shown in figure 25. Figure 26 shows the rate of vapor generation, $(\partial V / \partial H)_p$, as a function of pressure and density, a parameter required for solution of the energy equation.

Because the steady-state analysis indicated small pressure drops through the heat exchanger, the coolant properties for all nodes are evaluated at the jacket inlet pressure. Bivariate curve fits are required because the inlet pressure is a time-dependent function.

The steady-state chamber conditions assumed during this study were for a supplementary-cooled test at a mixture ratio of 5.75 and 80% of the Bartz heat flux. The walls of the heat exchanger were initially depressed to temperatures ranging from 330° to 376°R along the heat exchanger to simulate a cold start condition. Most of the analog runs were for a step input in heat transfer to the heat exchanger walls from the cold start condition. The step input was selected because it introduces the most severe disturbance into the heat exchanger system.

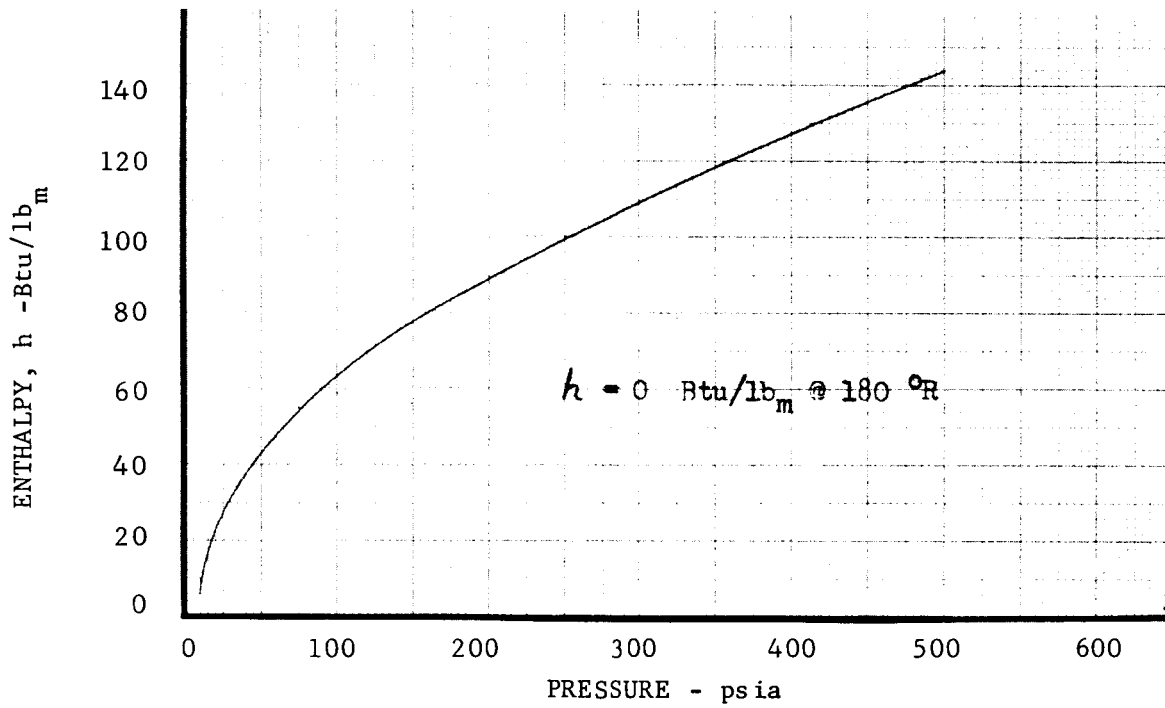


Figure 23. Enthalpy of Saturated Liquid Methane

DF 58480

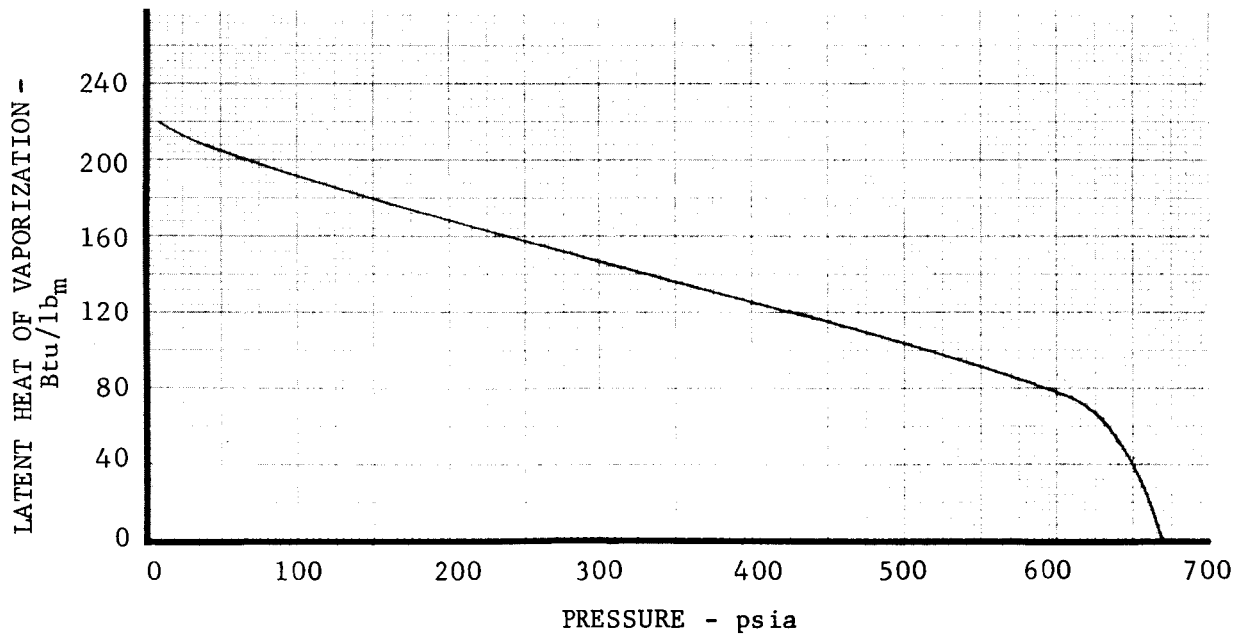


Figure 24. Latent Heat of Vaporization for Methane

DF 58481

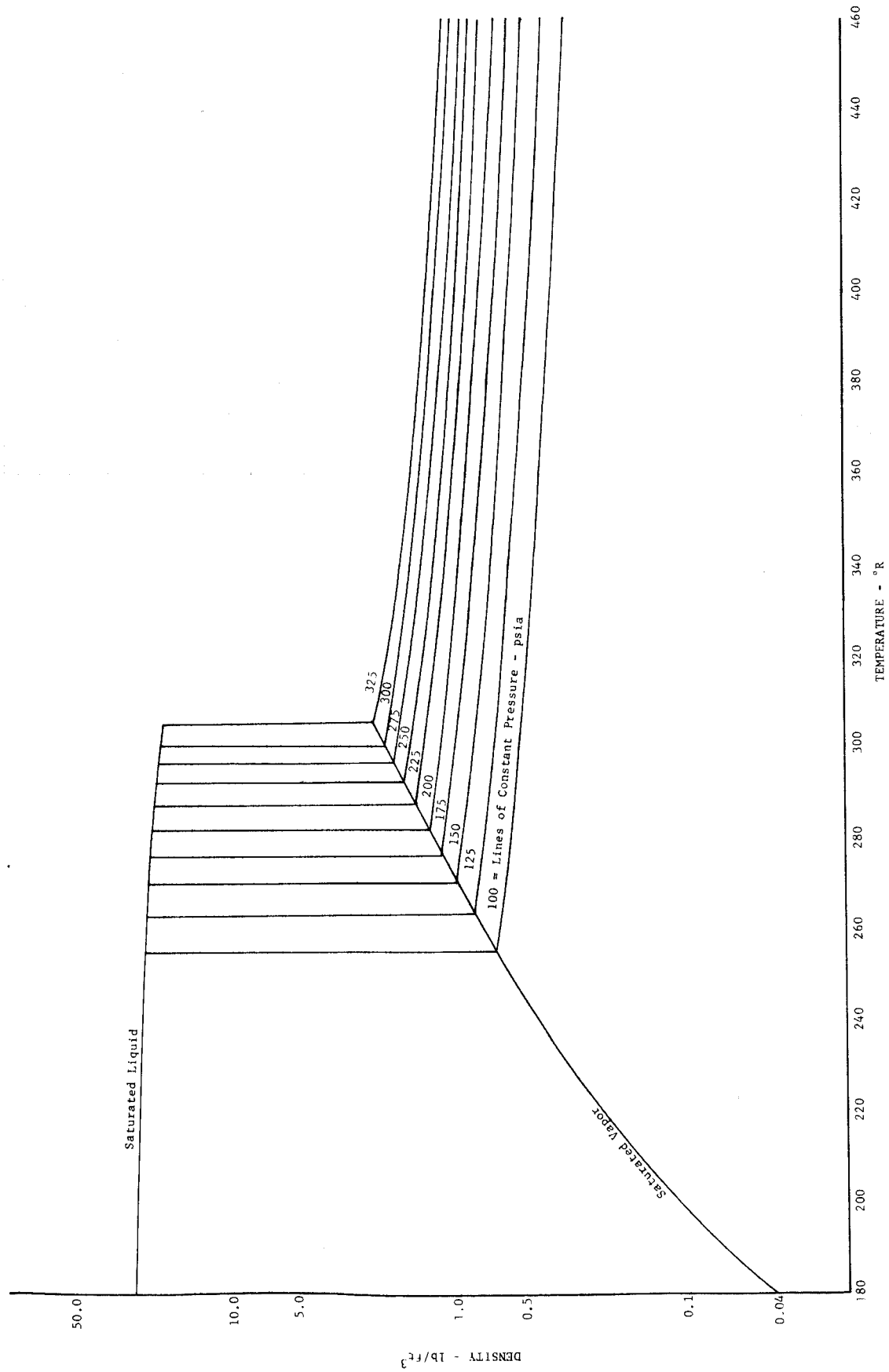


Figure 25. Density of Methane

DF 66877

DF 68317

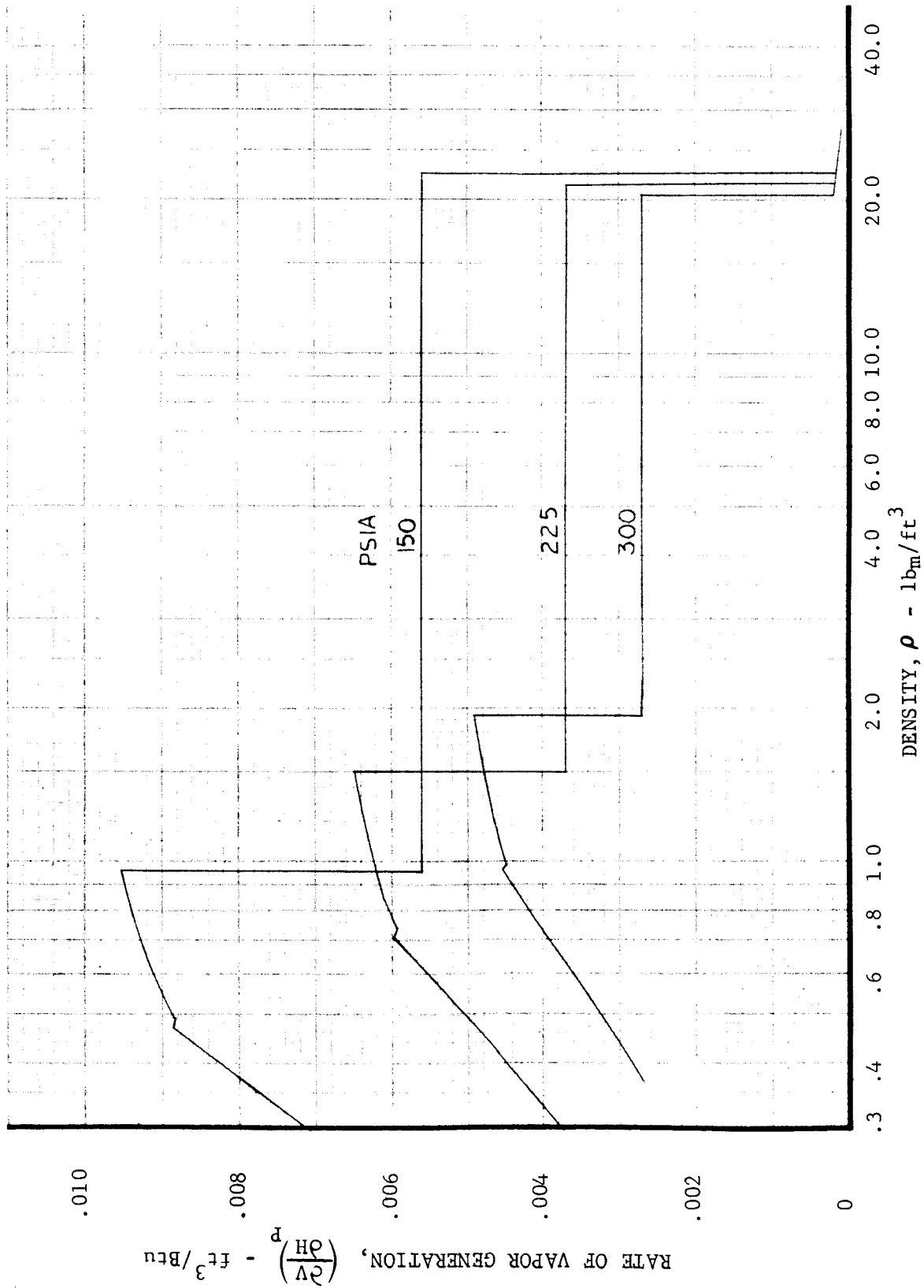


Figure 26. Rate of Vapor Generation for Methane

Analog solutions for the following cases were obtained:

1. Heat exchanger less inlet and outlet line dynamics and resistance. The inlet flow rate to the heat exchanger and discharge pressure were held constant. This constant flow condition approximates a cavitating venturi immediately upstream of the heat exchanger, while the constant discharge pressure approximates an instantaneously regulating dump control valve.
2. Heat exchanger less inlet and outlet line dynamics. The inlet flow measuring orifice and control valve were represented as a combined constant area restriction while the discharge pressure was held constant.
3. Heat exchanger with inlet line dynamics incorporated and the discharge control operating as a fixed restriction. This simulates zero gain inlet and outlet control valves and a zero volume outlet line.
4. Same as case 3 with the exception that the outlet plumbing volume effects were taken into account. Three values of volume were used: existing line volume, and ten times and one-hundred times the existing line volume.
5. Same as case 4 except that the heat transfer to the heat exchanger walls was ramped in $1/10$ and $1/2$ sec.

The heat exchanger was stable for both cases 1 and 2. Steady-state was achieved within 1 sec after initiation of the step input with the heat exchanger behaving basically as a damped first order system. It is interesting to note that the heat exchanger wall temperatures lag the heat input by a time factor of approximately three, i.e., large oscillations in coolant flowrate do not produce correspondingly large oscillations in wall temperature. Case 3, in which the discharge valve was represented by an orifice, was unstable with a frequency of 80 cycles per second. Case 4 was an attempt to stabilize the heat exchanger by using an accumulator to provide a time delay between the jacket discharge flow and pressure. The existing outlet plumbing volume did not stabilize the heat exchanger whereas, accumulators providing ten and one-hundred times the existing outlet volumes appeared to be marginally stable with a step input in heat transfer. Ramped inputs of $1/10$ and $1/2$ sec (case 5), with the ten times outlet plumbing volumes again displayed marginal stability but the one-hundred times volume was very stable. It is expected that if the transient characteristics of the outlet valve and the outlet plumbing dynamics were included, a stable situation would exist.

Figures 27 through 30 show a comparison of the heat exchanger inlet and outlet mass flux traces for cases 1, 2, 3, and 5. The arrow on each trace signifies the start of the heat input transient. As previously discussed, figures 27 and 28 display stable operation, whereas figure 29 indicates unstable behavior. Figure 30 indicates stable conditions for a 1/10 sec input ramp with one-hundred times the outlet line volume for the same conditions that caused the instability shown in figure 29. Typical time traces for coolant density, quality, and wall temperature for case 2 are presented in figures 31 and 32. Figure 31 shows the variation of density with time at the inlet to node 6 and at the outlet of the heat exchanger. Nodes 5 and 6 hot wall temperatures (figure 32) indicate slow response to the input disturbance with steady-state being achieved at approximately 3 sec (not shown) with values of 1620° and 2100°R, respectively. The average quality of node 6 indicates that almost complete vaporization of the coolant occurred during the transient. The final value at 3 sec is approximately 0.72.

It is concluded that the isolated heat exchanger is unstable for the conditions investigated, and that stabilized effects result from utilizing a control valve and accumulator downstream of the thrust chamber to maintain a constant discharge pressure and by limiting the rate of change of the heat input. While not investigated in this study, the use of flow restrictions upstream of the thrust chamber should also provide a stabilizing effect.

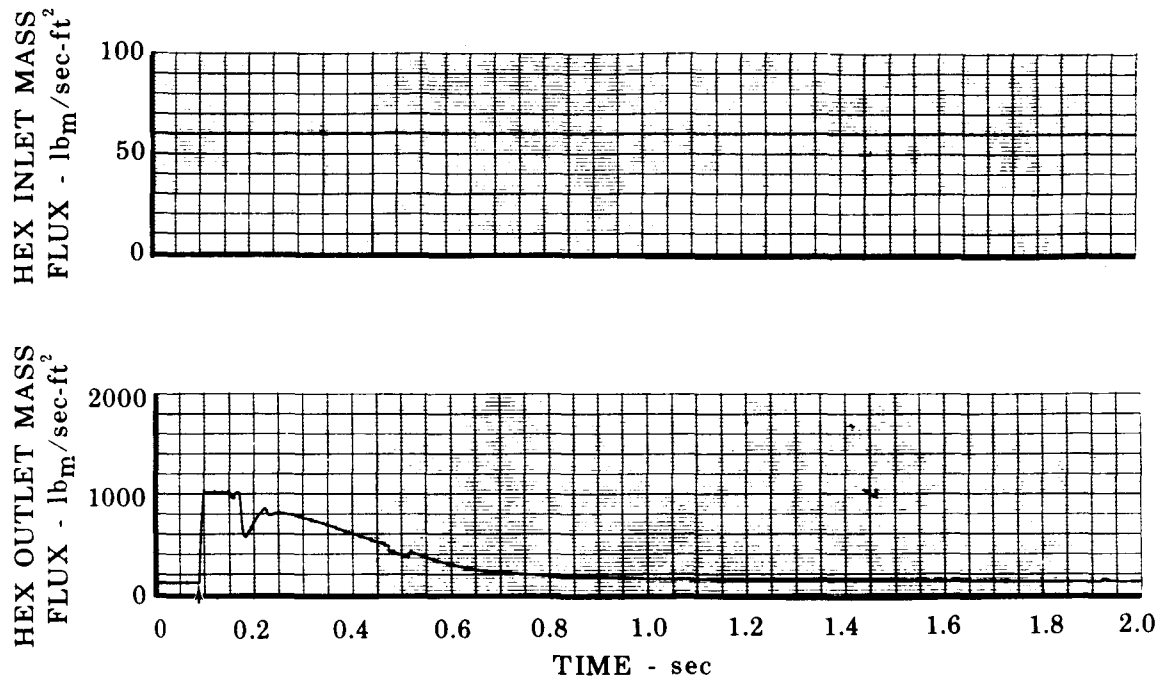


Figure 27. Heat Exchanger Inlet and Outlet
Mass Flux for Case 1

FD 23044

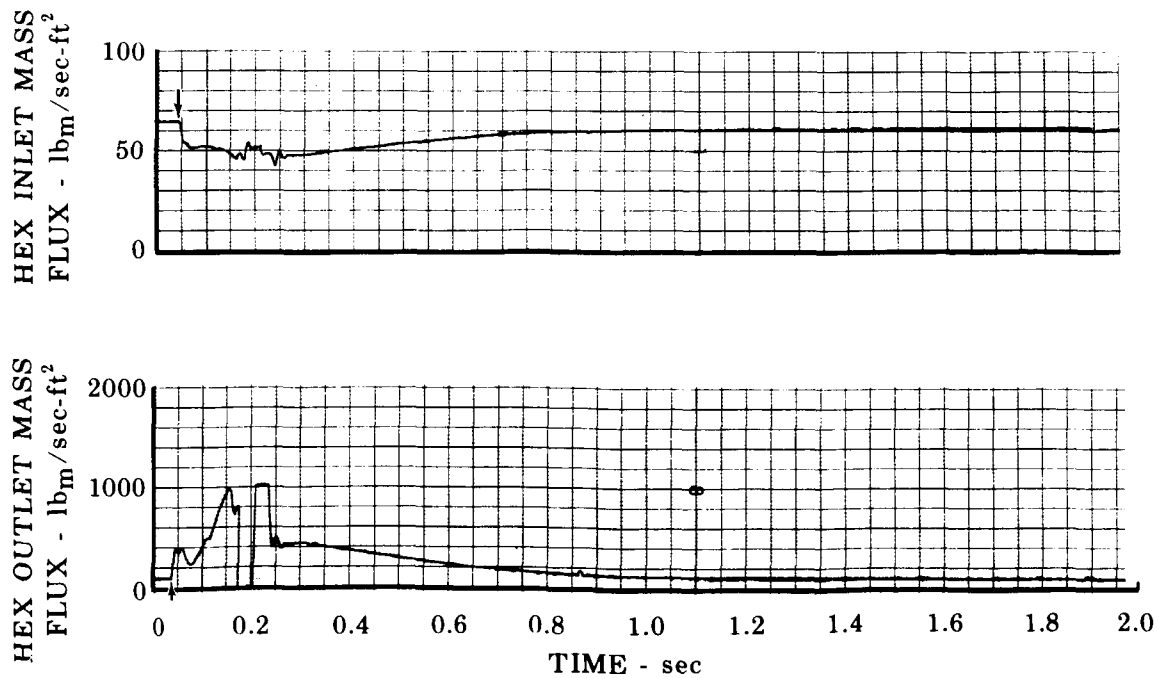


Figure 28. Heat Exchanger Inlet and Outlet
Mass Flux for Case 2

FD 23047

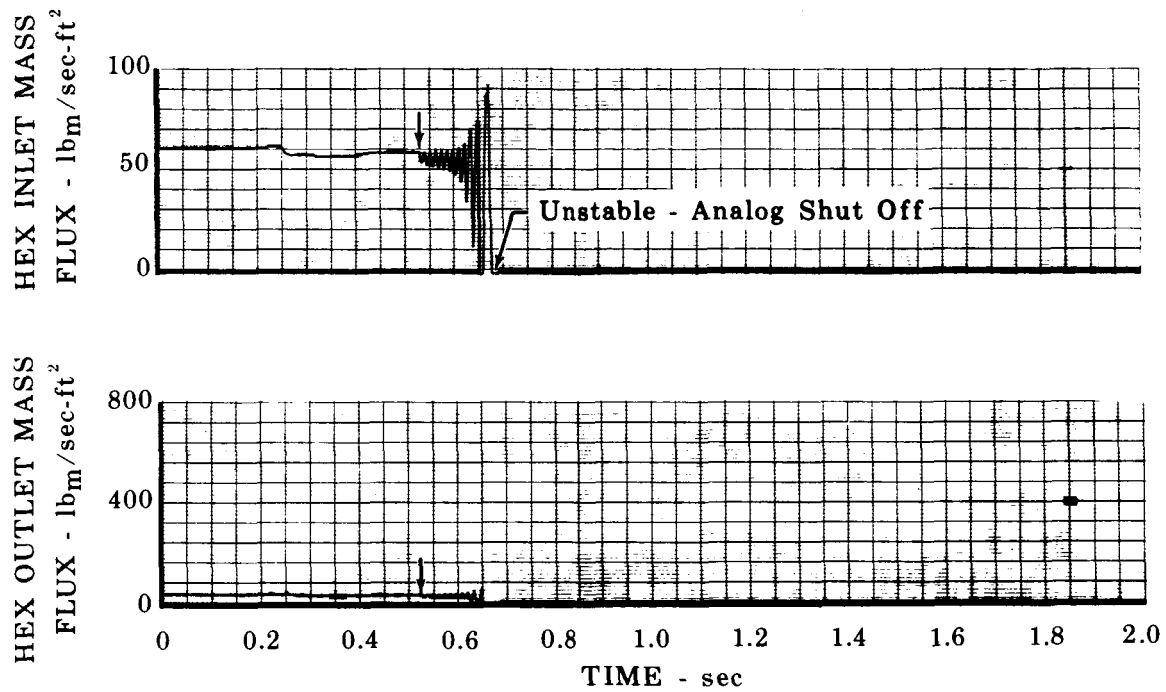


Figure 29. Heat Exchanger Inlet and Outlet
Mass Flux for Case 3

FD 23045

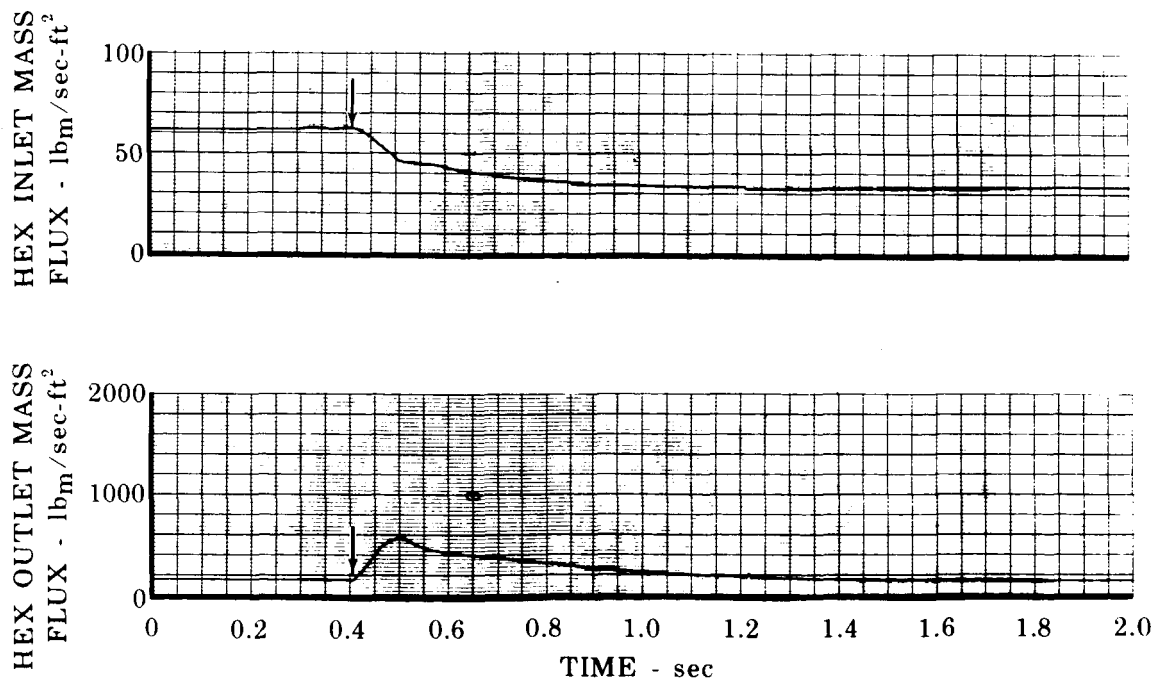


Figure 30. Heat Exchanger Inlet and Outlet
Mass Flux for Case 5

FD 23048

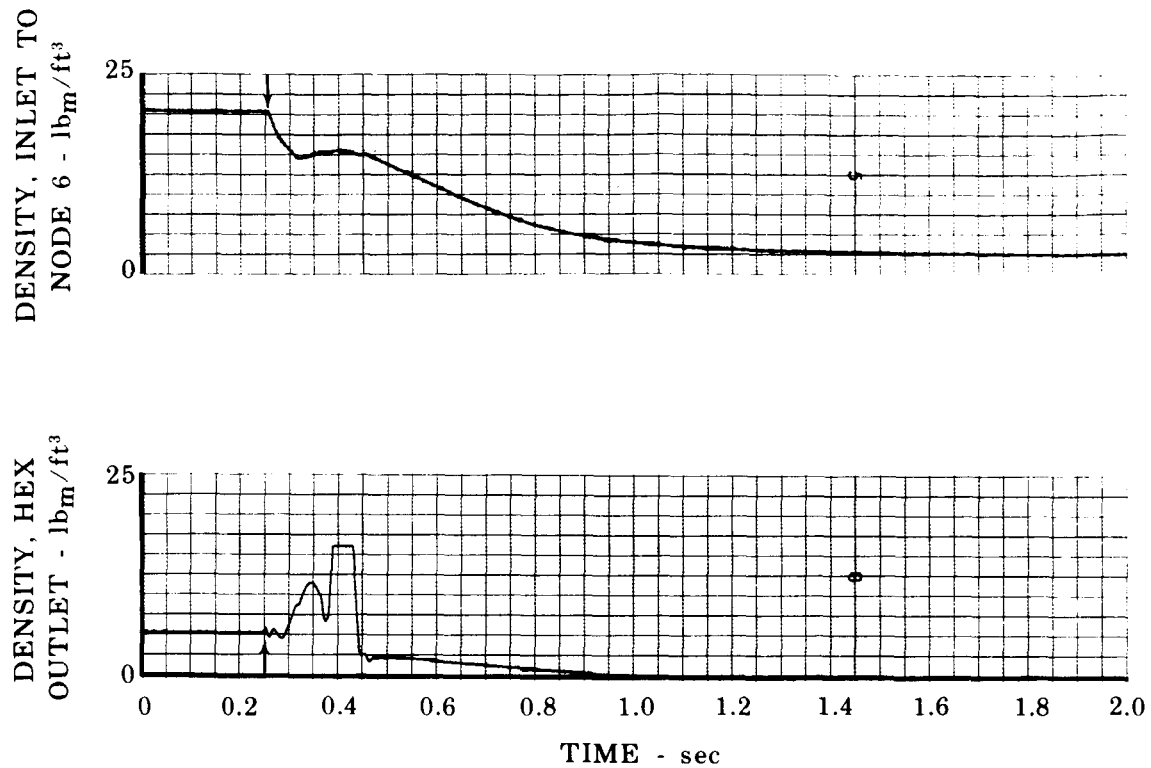


Figure 31. Variation of Density With Time for Case 2

FD 23046

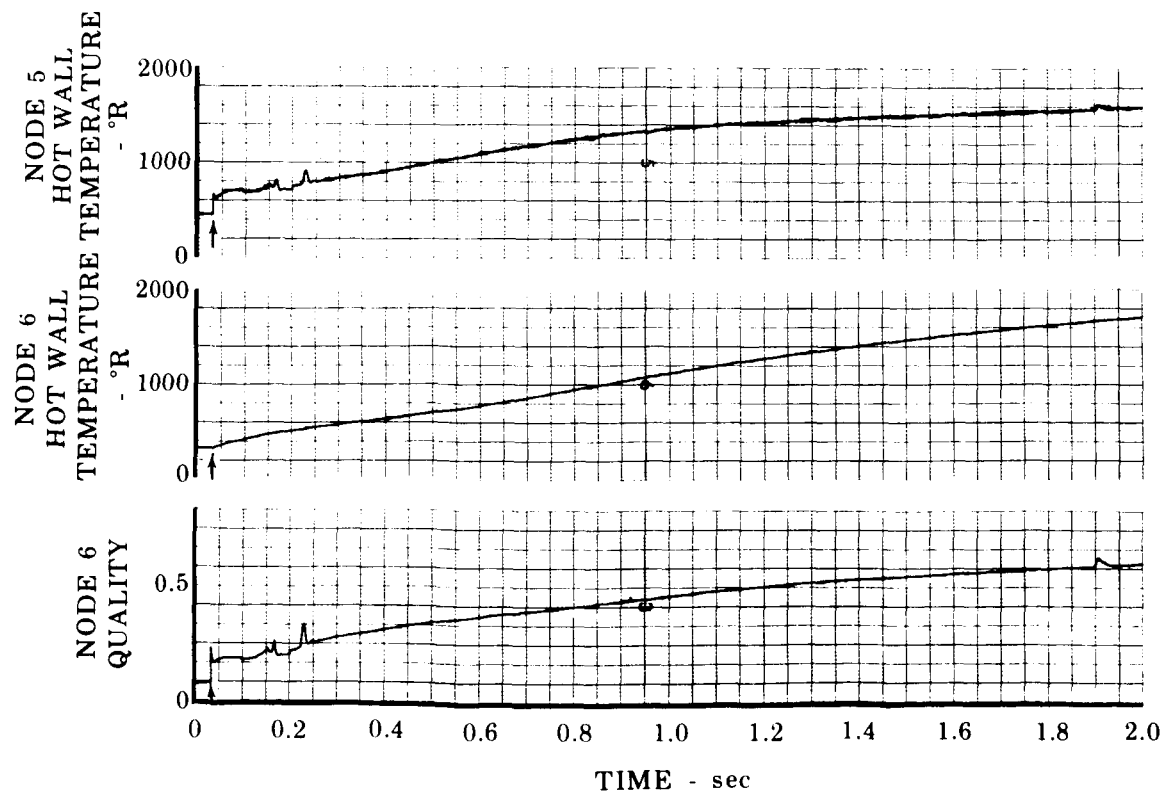


Figure 32. Variation of Wall Temperature and Quality With Time for Case 2

FD 23049

SECTION IV

TEST FACILITIES AND EQUIPMENT

A. LIQUID PROPELLANT RESEARCH FACILITY

All testing was conducted at Pratt & Whitney Aircraft's Liquid Propellant Research Facility (figure 33). This complex has the capability of flowing storable and cryogenic propellants at feed pressures up to 5500 psi. The facility is divided into four firing bays for 1000, 5000, 15,000 and 50,000-lb thrust levels. The 5000 and 15,000-lb thrust bays are connected to a continuous-acting steam-driven ejector system for altitude simulation. These two bays have exhaust diffusers that discharge into a common cross-over duct that connects them to the two-stage steam ejector. For the 5000-lb thrust chambers used in this program, the ejection system was able to maintain pressures of approximately 0.2 psia (simulated altitude of approximately 100,000 ft).

Rigorous standards of materials selection, fabrication, cleaning, passivation, and leak detection are followed for fluorine test facility design and operations. Liquid-fluorine handling is accomplished remotely from the facility control room, which is located about 300 ft from the test stands. All operations are carried out using remote-operated valves except for transfer from the delivery vehicles, which are equipped with manual valves. Liquid fluorine is stored in roadable Dewars similar to the delivery vessels, but equipped with remote-operated valves. A detailed description of the fluorine procedures used by Pratt & Whitney Aircraft is presented in Reference 8.

B. PROPELLANT SUPPLY SYSTEM

All rocket chamber test firings were conducted in the 5000-lb thrust B-27 stand firing bay. Three different propellant flow path configurations were used for the uncooled, supplementary cooled, and regeneratively cooled tests; the propellant flow paths are shown in figures 34, 35, and 36.

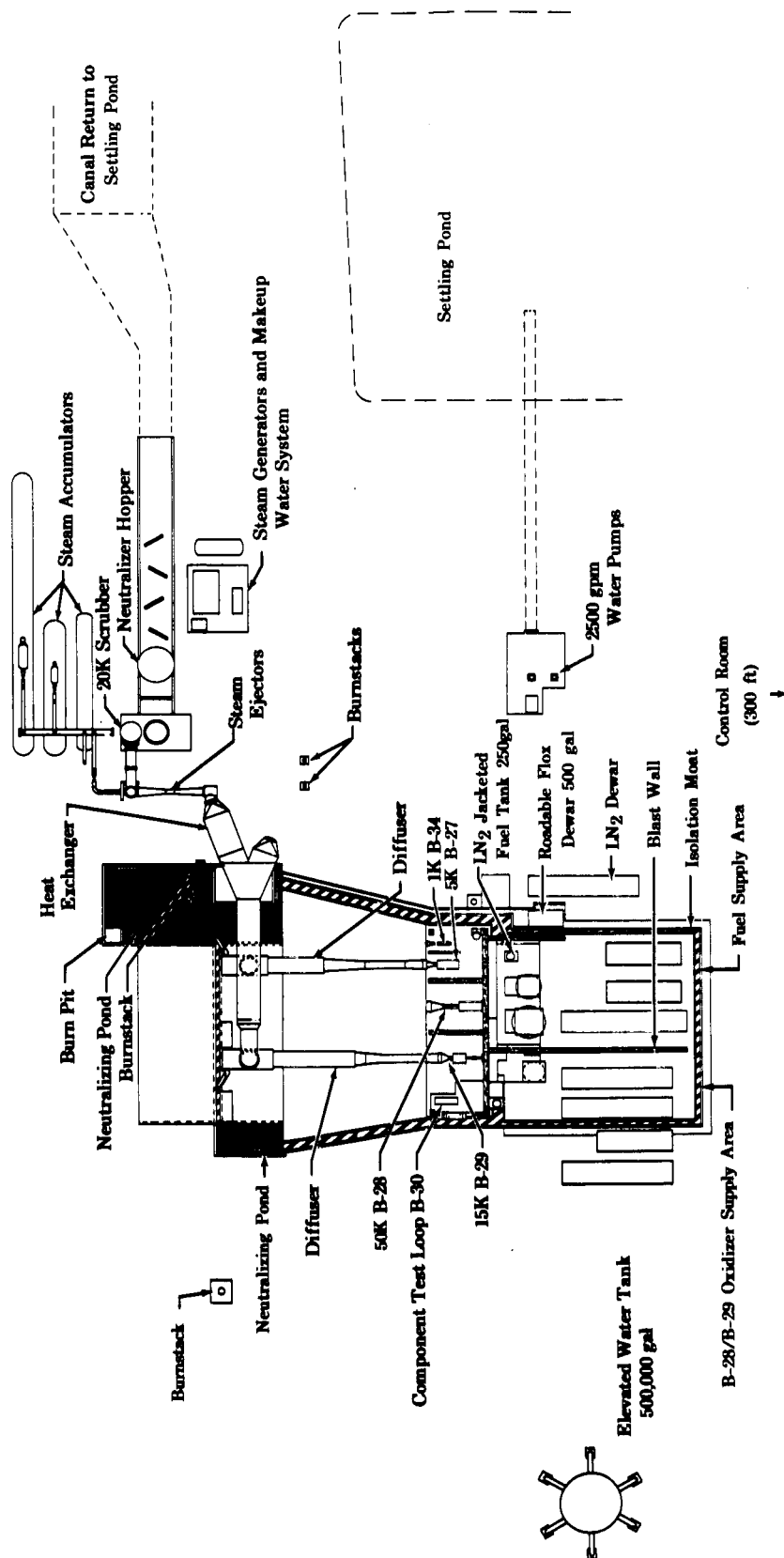


Figure 33. Schematic of Liquid Propellant Research Facility

FD 12808B

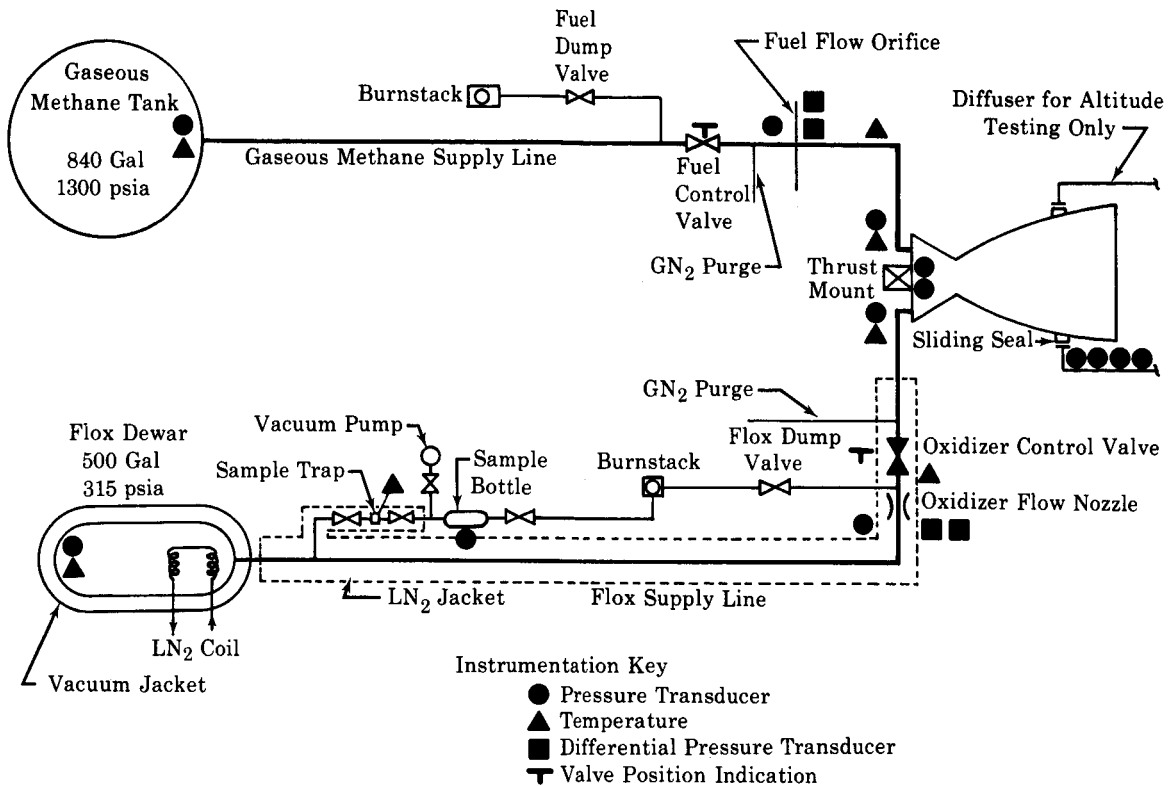


Figure 34. Flox/Methane Test Stand Flow Schematic for Uncooled Tests

FD 25250

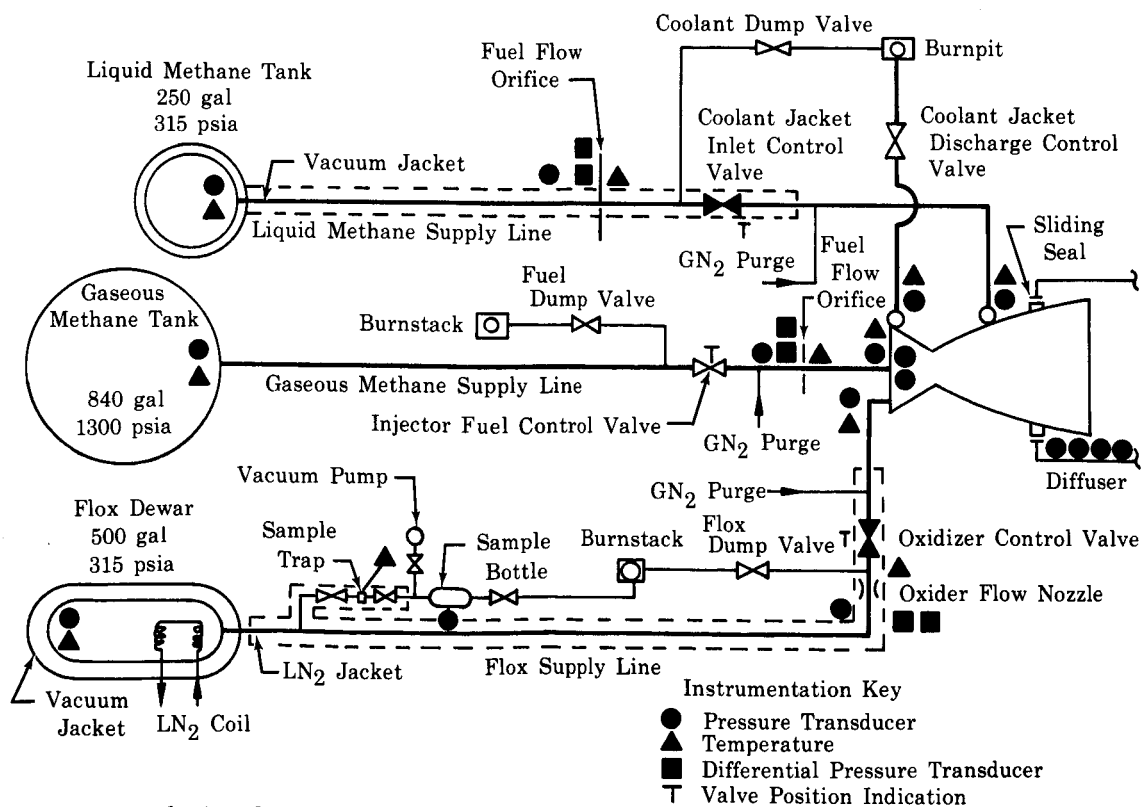


Figure 35. Flox/Methane Test Stand Flow Schematic for Supplementary-Cooled Tests

FD 25249

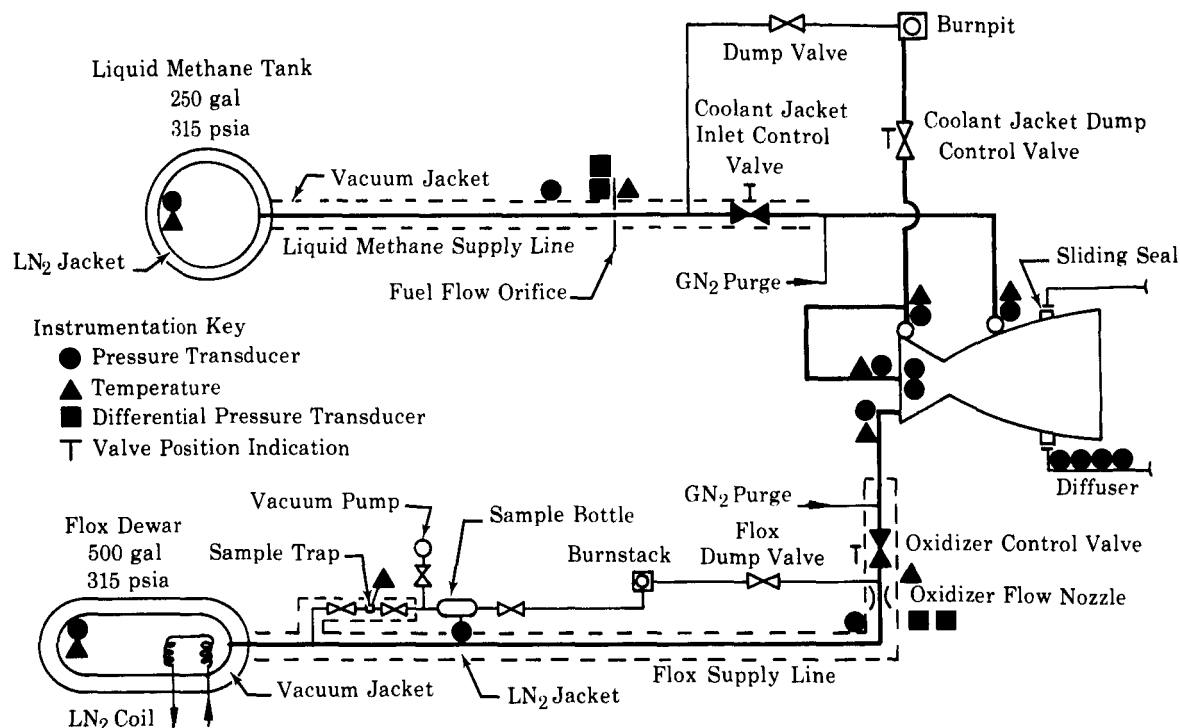


Figure 36. Flox/Methane Test Stand Flow Schematic for Regeneratively Cooled Tests

FD 25248

Gaseous methane, used in the uncooled tests, was supplied from an 840-gal tank. The gaseous methane was pressurized by flowing the fuel into the tank from a high-pressure tube-trailer in which the methane was stored. Liquid methane, for the cooled tests, was supplied from a 250-gal liquid nitrogen jacketed tank. Fuel temperature settings in this tank were obtained by controlling the nitrogen jacket pressure. The liquid methane was liquefied from the gaseous state by allowing it to enter the cooled tank where it was condensed. The fuel supply lines were vacuum jacketed up to the test chamber inlets. Fuel flow was controlled by up to three electrohydraulic servo-operated control valves.

The liquid flox was supplied from a 500-gal vacuum jacketed roadable Dewar. Liquid nitrogen cooling coils within the Dewar minimized boiloff losses to a negligible amount. Liquid flox was supplied to the injector through a liquid nitrogen jacketed line and controlled by a single servo-operated control valve. Flox was mixed within the Dewar by adding liquid oxygen and liquid fluorine while the Dewar weight was monitored from within the control room. Flox concentration, calculated from oxidizer weights, was verified by laboratory analysis of samples taken at some time during each test series. Accurate samples were obtained by trapping liquid flox in an evacuated space between two remotely operated valves. The two valves and the sample chamber were liquid nitrogen jacketed to prevent flox concentration changes due to fractional distillation. After the liquid flox was trapped, the sample system was isolated and the nitrogen flow secured to allow complete evaporation of the liquid flox into an evacuated

sample bottle. The system was allowed to remain intact for a period sufficient to ensure that a homogenous gas was contained throughout. The sample bottle was then removed to the chemistry laboratory for mercury absorption analysis. Duplicate analyses of samples ranging from 63 to 93% fluorine have shown a repeatability of 0.23% using this system.

C. CONTROL SYSTEM

Test firing events were controlled by a digital sequencer, analog-computer, electrohydraulic valve combination. Basically, the system consisted of oxidizer and fuel flowrate control, along with interrogation of certain parameters at specific time intervals to provide a go/no-go indication for the test to proceed or advance automatically to a controlled shutdown. The analog-computer was used for automatic closed loop control of the servo-operated control valves. The valves controlled upstream pressure and differential pressure at the oxidizer flow nozzle and fuel flow orifice to obtain predetermined flowrates. In addition to flowrate control, position control and pressure control of the valves were used during starting transients.

For all uncooled tests the fuel control valve opened in injector inlet pressure control then switched to flow control at approximately +0.75 sec into the test. The oxidizer control valve opened in position control then switched to flow control at approximately +1.2 sec into the test. The object of starting in this manner was to eliminate valve upsets during the starting transient when two-phase flow might be present. The fuel control valve was always opened slightly earlier and closed slightly later than the oxidizer control valve. Two sequenced go/no-go checks were made to ensure that ignition was obtained before a large quantity of propellants had been injected. A burn-wire was used to verify that ignition had occurred before +1.5 sec had elapsed. A continuous sample of chamber pressure was made to determine that it did not drop below 25 psia after +1.5 sec. For altitude tests, a continuous check of diffuser pressure was made to determine that it did not rise above 3 psia before start or between start +1.0 sec and shutdown.

In the cooled altitude tests the oxidizer control valve was opened slowly over a 10-sec ramp in position control then switched to flow control for the remainder of the test. Three fuel-control valves were used in the supplementary-cooled tests. The injector fuel inlet control valve was opened in injector inlet pressure control then switched to flow control at +1.5 sec. The cooling jacket inlet control valve and the cooling jacket discharge control valve both opened in position control at -8.0 sec. At +2.0 sec, the coolant jacket inlet valve switched to flow control; 0.5 sec later the coolant jacket discharge valve switched to coolant discharge pressure control. The coolant control valves both remained open for 5.0 sec at shutdown.

For the regeneratively cooled runs the oxidizer control valve was programed the same as for the supplementary tests. Only two fuel-control valves were used, one at the cooling jacket inlet, the other as a dump valve between the cooling jacket discharge and the injector fuel inlet to allow a complete jacket cooldown before starting the test firing. The cooling jacket inlet control valve was sequenced approximately the same as for the supplementary-cooled tests, while the cooling jacket dump valve was closed after the start transient was negotiated. An additional go/no-go check was made on the cooled tests to assure that cooling jacket flow did not drop below the amount necessary to avoid damaging the chamber during the start transient.

D. INSTRUMENTATION AND DATA ACQUISITION

The Liquid Propellant Research Facility data system provided recording of temperatures, pressures, thrust, and valve positions through a 96-channel low-level input analog-to-digital converter that fed a magnetic tape system. Also used were a 36-channel oscillograph system and 12 direct inking strip charts. A separate system consisting of a high-speed tape recorder, amplifiers, and transducers provided high-frequency data capability to 20,000 cps. Six closed circuit television channels provided continuous test observation. The instrumentation locations used in this test program are shown in the schematic flow diagrams (figures 34, 35, and 36). As shown on these diagrams, redundant measurements were made for all critical performance parameters (e.g., flowrates, chamber pressure, diffuser pressure, and thrust). All instrumentation was recorded by the digital system. Redundant oscillograph recordings of the critical performance parameters were made to guarantee that data would be available in the event of a digital system failure. Additional readout of the critical starting temperatures and pressures were available on the control room strip charts.

Pressures were sensed using standard 4-arm bridge strain gage pressure transducers. Temperature measurements were made with standard resistance thermometers and chromel-alumel or copper-constantan thermocouples. In use, the thermocouples formed the active arm of a bridge completion network. Thrust was measured with 4-arm bridge strain gage load cells. The valve positions were determined by use of position measuring potentiometers. Fuel flowrate was measured using upstream and differential pressure measurements in conjunction with a calibrated flow orifice. The oxidizer flowrate was similarly measured using a calibrated flow nozzle.

To assure validity of test data, redundant instrumentation and accurate calibration procedures traceable to the National Bureau of Standards (NBS) were used. It is normal to achieve total data measurement accuracies (three standard deviations) of $\pm 0.5\%$ for pressure, $\pm 0.5\%$ for thrust, $\pm 1\%$ for valve positions, and from $\pm 1^\circ$ to $\pm 5^\circ$ for temperatures,

depending on the temperature range of interest. The Instrumentation Engineering Section maintains a complete computerized record of evaluations, calibrations, and maintenance history relating to all sensing and recording equipment. Table 4 presents the maximum estimated performance data errors for a typical uncooled simulated altitude test.

TABLE 4. ESTIMATED PERFORMANCE DATA ACCURACY*

Parameter	Estimated Error, %	
	(68% Confidence)	(95% Confidence)
Characteristic Velocity	± 0.443	± 0.887
Vacuum Specific Impulse	± 0.643	± 1.287
Vacuum Thrust Coefficient	± 0.523	± 1.047

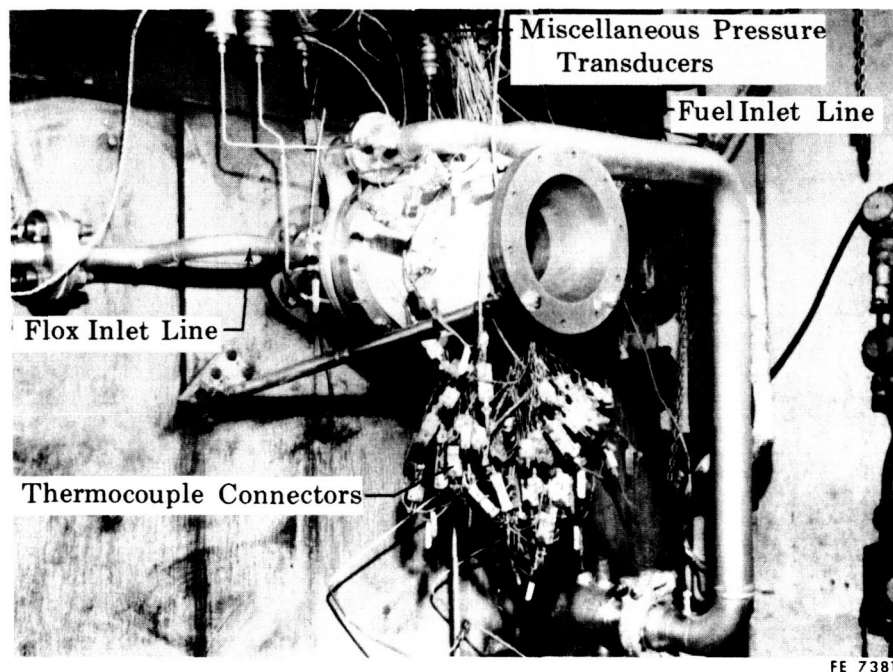
*Maximum statistical error estimates for a simulated altitude test using an uncooled chamber with flox-methane at a mixture ratio of 5.7. This estimate performed under Contract NAS3-6296.

SECTION V

INJECTOR CHECKOUT TESTS — TASK II

A. TEST DESCRIPTION

Injector checkout testing consisted of 11 uncooled sea level tests, five with the triplet injector and six with the coaxial injector. These injectors, described in Section III, were mounted on an uncooled copper thrust chamber with a nozzle expansion ratio of 1.98 and a divergence half-angle of 15 deg. The assembly is shown mounted on the test stand in figure 37. The primary goal of these tests was to demonstrate 95% combustion efficiency over a mixture ratio range of 4.0 to 5.75. A second objective was to minimize variations in circumferential heat flux profile caused by injection pattern nonuniformities. Liquid flox and gaseous methane were used at flowrates corresponding to 5000-lb vacuum thrust at 100-psia nominal chamber pressure, with an area ratio of 40 exhaust nozzle. All tests with the triplet injector were 4.0 sec duration. Test durations ranged from 2.0 to 6.0 sec for the coaxial injector.



FE 73816

Figure 37. Engine Installation for Uncooled
Sea Level Tests

FD 24934

B. TEST PERFORMANCE

Table 5 presents measured data from the 11 uncooled sea level test firings. Table 6 shows calculated performance data, and table 7 presents calculated data for correlation of injector performance results. Data reduction procedures are described in detail in Reference 2.

TABLE 5. MEASURED UNCOOLED SEA LEVEL TEST DATA

Test	Injector	Test Duration, sec	P _c , psia	F, lb	\dot{w}_o , lb/sec	\dot{w}_f , lb/sec	T _o , °R	T _f , °R	ΔP_o , psi	ΔP_f , psi
1 USL	Triplet	4.0	98.2	3257	11.5	2.60	181	514	72	123
2 USL		4.0	96.1	3081	11.2	2.20	191	517	50	79
3 USL		4.0	98.8	3171	12.0	1.95	168	517	34	65
4 USL		4.0	93.1	2958	11.8	1.79	181	512	47	58
5 USL		4.0	95.1	3040	11.7	1.88	177	514	41	62
6 USL	Coaxial	2.0	103.2	3231	11.5	2.67	174	511	31	95
7 USL		4.0	95.7	2952	11.4	2.28	181	512	31	79
8 USL		6.0	91.6	2801	11.4	2.03	177	511	29	65
9 USL		6.0	90.1	2739	11.8	1.87	170	512	31	57
10 USL		6.0	100.3	3153	11.6	2.66	170	514	33	94
11 USL		6.0	91.1	2757	11.8	1.95	167	514	35	61

TABLE 6. CALCULATED PERFORMANCE DATA FOR UNCOOLED SEA LEVEL TESTS

Test	Injector	r	\dot{w}_p , lb/sec	Q, Btu/sec	I _{gl} , sec	c*, ft/sec	I _{gl} , sec	c* _{P_c} , ft/sec	c* _F , ft/sec	$\eta_{c^*P_c}^{(1)}$	η_{c^*F}	$\eta_{c^*P_c}^{(2)}$	$\eta_{c^*F}^{(3)}$	η_{I_s}	Δt Used, sec
1 USL	Triplet	4.43	14.1	1200	231	6896	252	6559	6527	0.951	0.946	0.939	0.959	0.913	2.3
2 USL		5.09	13.4	1200	231	6973	253	6674	6583	0.957	0.944	0.947	0.957	0.911	2.8
3 USL		6.18	14.0	1200	227	6926	253	6673	6423	0.963	0.927	0.952	0.939	0.895	2.5
4 USL		6.60	13.6	1200	218	6841	246	6466	6260	0.945	0.915	0.938	0.928	0.883	2.1
5 USL		6.21	13.6	1200	224	6918	251	6615	6405	0.956	0.926	0.948	0.938	0.894	2.4
6 USL	Coaxial	4.32	14.2	850	227	6879	255	6729	6346	0.978	0.922	0.959	0.932	0.891	0.7
7 USL		5.01	13.7	850	215	6967	253	6475	6145	0.929	0.882	0.912	0.892	0.851	1.5
8 USL		5.63	13.4	850	208	6995	251	6308	6013	0.902	0.860	0.891	0.870	0.829	1.3
9 USL		6.33	13.7	850	200	6891	246	6088	5800	0.884	0.842	0.876	0.852	0.812	1.6
10 USL		4.35	14.3	850	222	6883	253	6536	6238	0.950	0.906	0.941	0.916	0.975	4.1
11 USL		6.03	13.8	850	201	6945	249	6156	5812	0.886	0.837	0.877	0.847	0.807	4.3

(1) Based on injector face pressure measurements.

(2) Corrected for momentum loss, throat growth, and chamber heat loss.

(3) Corrected for heat loss only.

TABLE 7. INJECTOR PERFORMANCE COMPARISON - UNCOOLED SEA LEVEL TESTS

Test	Injector	\dot{w}_o , lb/sec	\dot{w}_f , lb/sec	A_{cdo} , in. ²	A_{cdf} , in. ²	V_o , ft/sec	V_f , ft/sec	$\dot{w}_f V_f / \dot{w}_o V_o$	$\eta_c^* P_c (cor)$	r
1 USL	Triplet	11.5	2.60	0.38	0.6809	52.8	1346.6	5.75	0.939	4.43
2 USL		11.2	2.20	0.38	0.7268	55.6	1309.5	4.82	0.947	5.09
3 USL		12.0	1.95	0.38	0.6945	53.0	1220.9	3.73	0.952	6.18
4 USL		11.8	1.79	0.38	0.6881	54.1	1194.7	3.35	0.938	6.60
5 USL		11.7	1.88	0.38	0.6971	52.8	1214.3	3.70	0.948	6.21
6 USL	Coaxial	11.5	2.67	0.36	0.7777	54.6	1342.5	5.70	0.959	4.32
7 USL		11.4	2.28	0.36	0.7502	55.2	1318.6	4.78	0.912	5.01
8 USL		11.4	2.03	0.36	0.7484	54.4	1250.9	4.09	0.891	5.63
9 USL		11.8	1.87	0.36	0.7397	55.3	1200.1	3.43	0.876	6.33
10 USL		11.6	2.66	0.36	0.7912	54.1	1345.7	5.73	0.941	4.35
11 USL		11.8	1.95	0.36	0.7453	54.5	1226.5	3.74	0.877	6.03

Figure 38 shows characteristic velocity (c^*) and characteristic velocity efficiency (η_c^*) test data as a function of mixture ratio (r). The triplet injector provided approximately 95% η_c^* over the mixture ratio range of interest, thereby achieving the contract objective. The coaxial injector provided approximately 96% η_c^* at a mixture ratio of 4.3; however, efficiency dropped off rapidly with increasing mixture ratio.

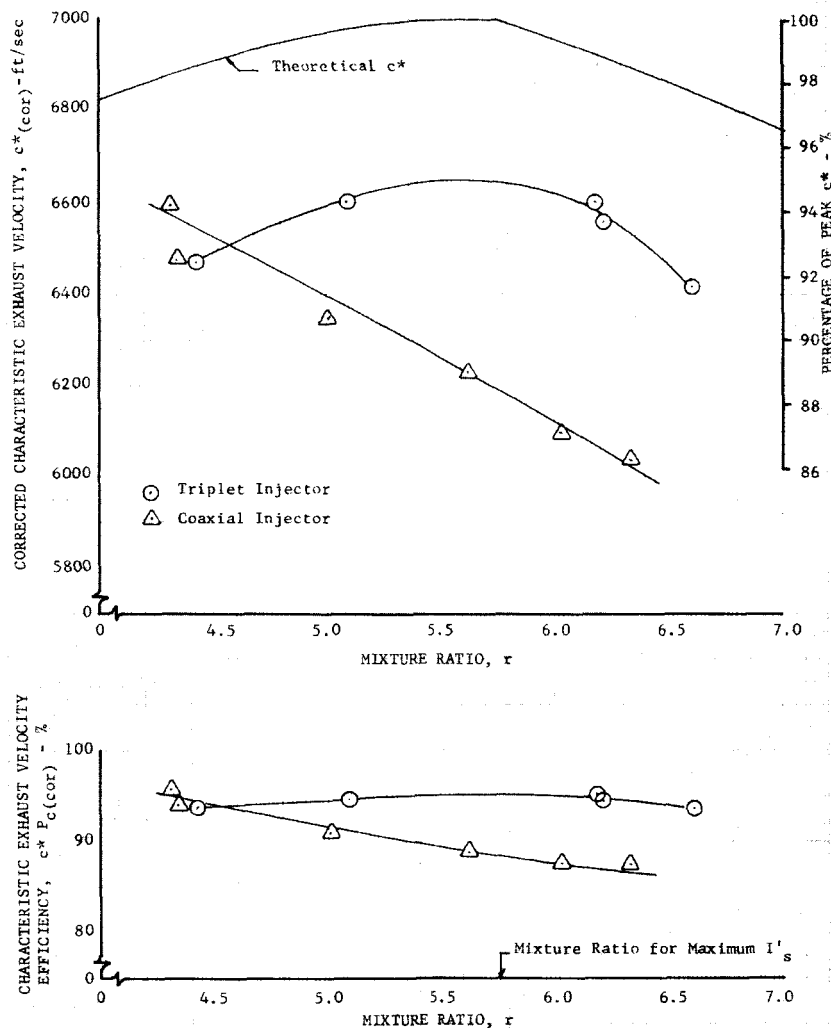


Figure 38. Flox-Methane Characteristic Exhaust Velocity: 82.6% F_2 in Flox

DF 61658

Figure 39 correlates η_c^* with fuel-to-oxidizer momentum ratio for the coaxial injector and five coaxial injectors tested under Contract NAS3-4195. Injector 1 was a modified RL10A-3 type injector with ribbon swirlers. Injectors 2, 3, 5, and 6 did not have swirlers, and the present Contract NAS3-10294 injector has tangential entry swirlers. A good correlation between momentum ratio and number of elements is achieved for all of the data except the single point obtained with the modified RL10A-3 injector. It may be concluded that (1) the tangential entry swirlers had no significant effect on η_c^* and (2) increased momentum ratio

should provide the same increased performance with the coaxial 145-element injector as with previous injectors. For the cooled tests the momentum ratio was predicted to be significantly higher for a given mixture ratio due to the higher temperature of the gaseous methane entering the injector from the cooling jacket. As shown in figure 40, this increased momentum ratio was predicted to provide a substantial increase in efficiency. As discussed in Section VII, an improvement in η_c^* was obtained.

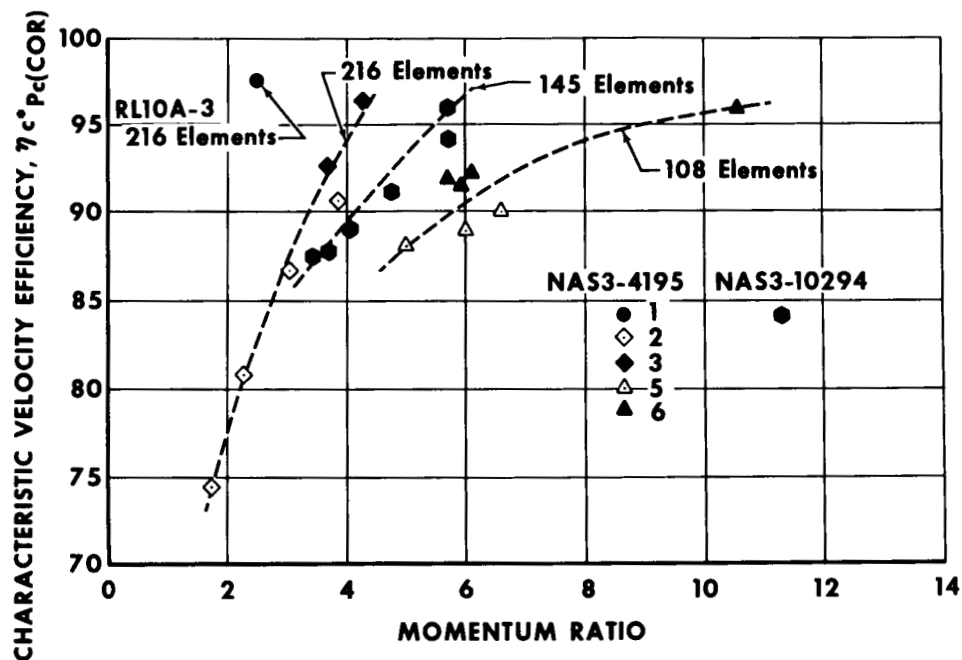


Figure 39. Effect of Momentum Ratio for Coaxial Injectors

GS 6761A

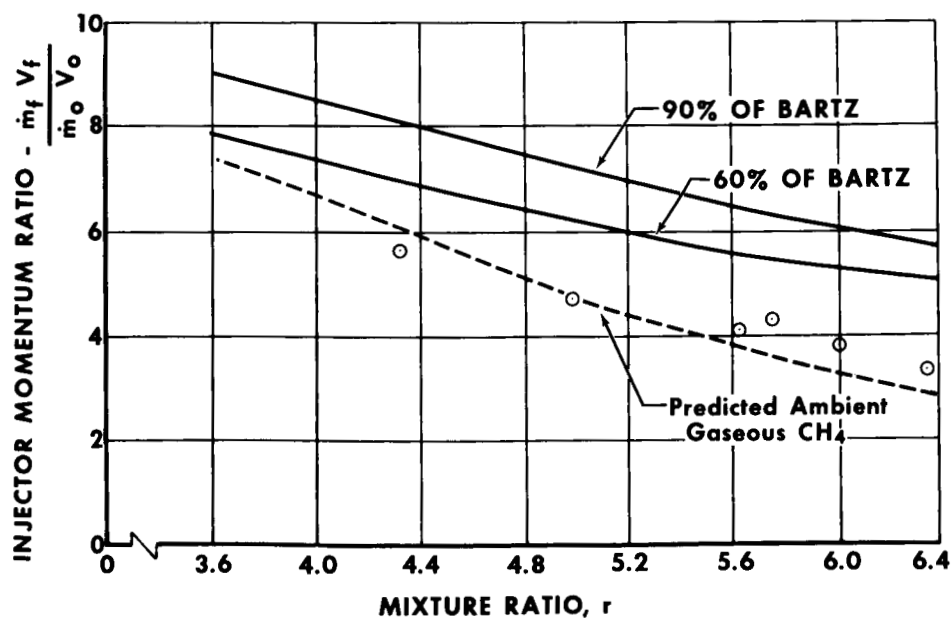


Figure 40. Predicted Coaxial Injector Performance

GS 6762

C. HEAT TRANSFER

Analysis of the wall temperature data from the solid copper chamber indicated that the chamber heat fluxes were 110 to 120% of the theoretical estimates for the triplet injector and 60 to 75% for the coaxial injector. Figures 41 and 42 show theoretical and experimental gas film coefficients for test No. 2 USL with the triplet injector and test No. 8 USL with the concentric element injector as a function of axial distance along the copper chamber from the injector face. While the total heat fluxes obtained with the triplet injector were more than the predicted values, the peak heat fluxes (as indicated by the peak in film coefficient in figure 41) were less than the predicted values. Figures 43, 44, 45, and 46 show circumferential temperature rise data for the two injectors at two axial locations. Circumferential temperature variations generally ran from ± 10 to $\pm 20\%$. One-dimensional analysis of the temperature data indicates that the percentage of circumferential heat flux variation is approximately equal to the temperature variation. Therefore, the variations in circumferential heat flux profile should be of the order of ± 10 to $\pm 20\%$.

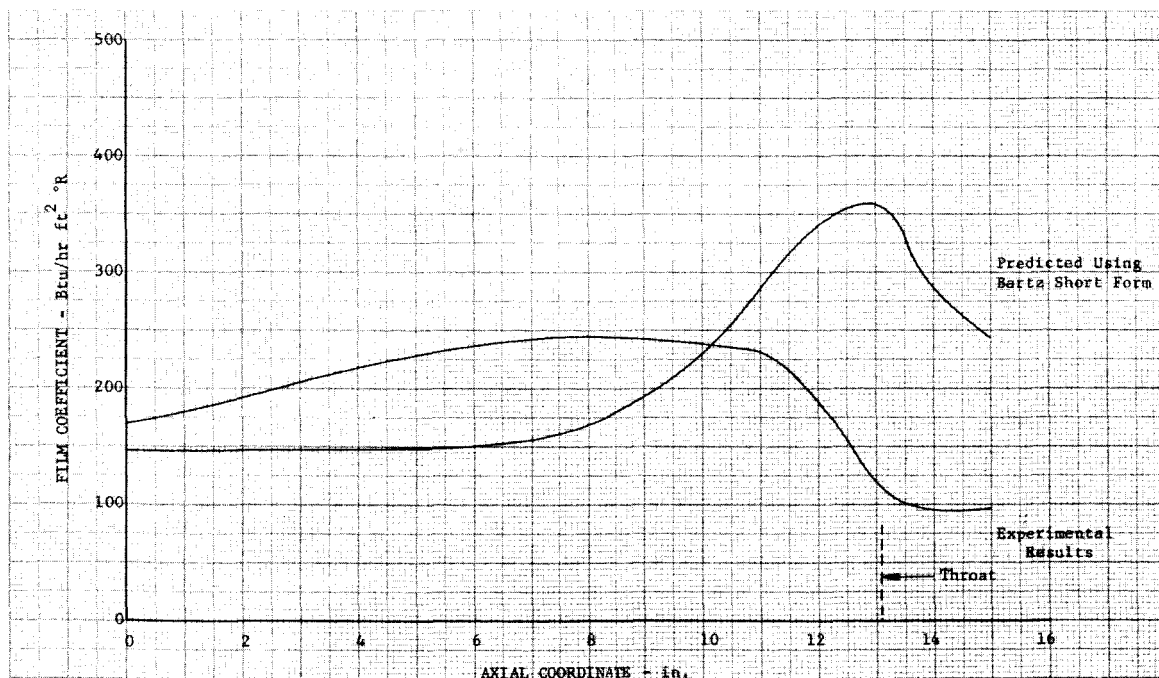


Figure 41. Comparison of Heat Transfer Coefficients, Test No. 2 USL, $r = 5.09$

DF 61126

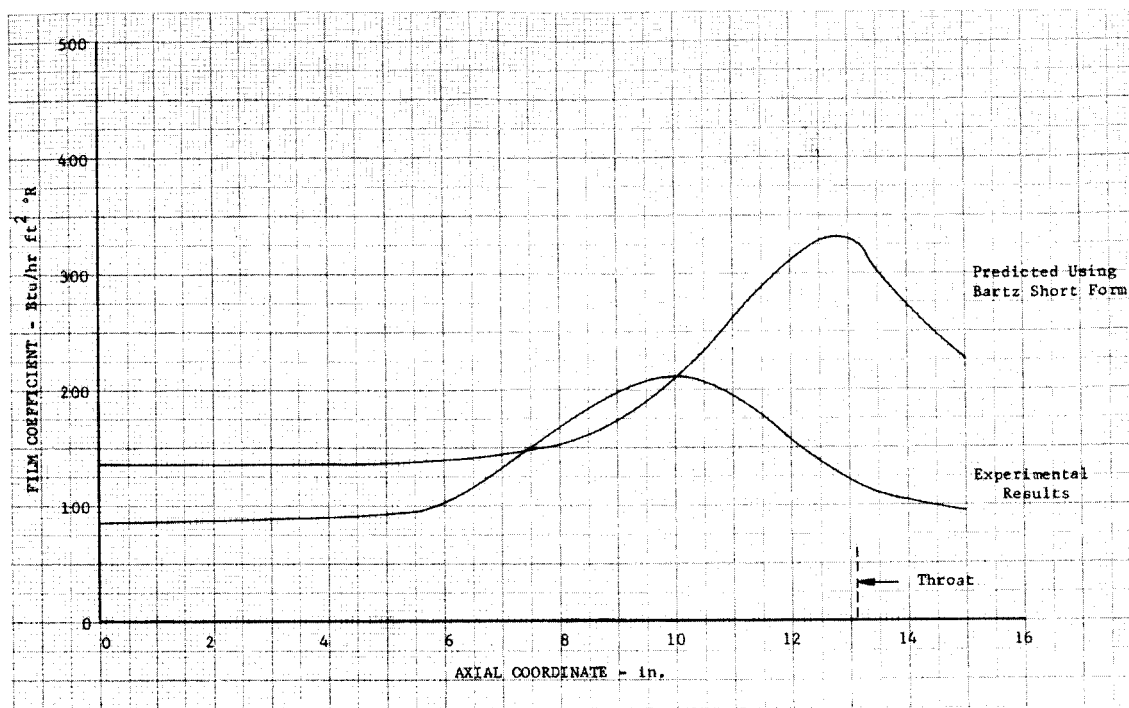


Figure 42. Comparison of Heat Transfer Coefficients, Test No. 8 USL, $r = 5.63$

DF 61131

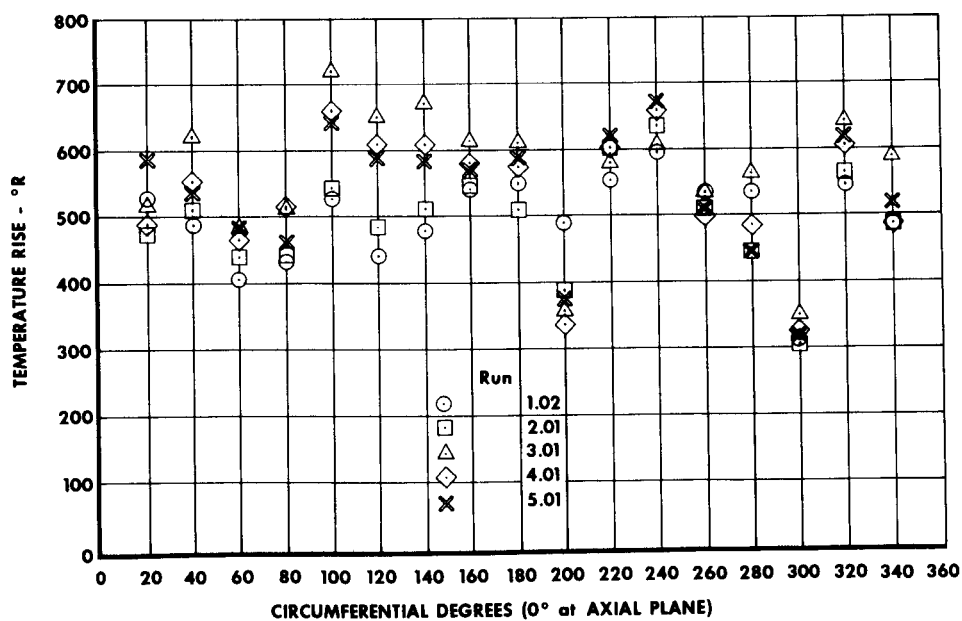


Figure 43. Triplet Injector — Facing Injector From Exit (Axial Plane 3 in. From Injector Face)

GS 6766

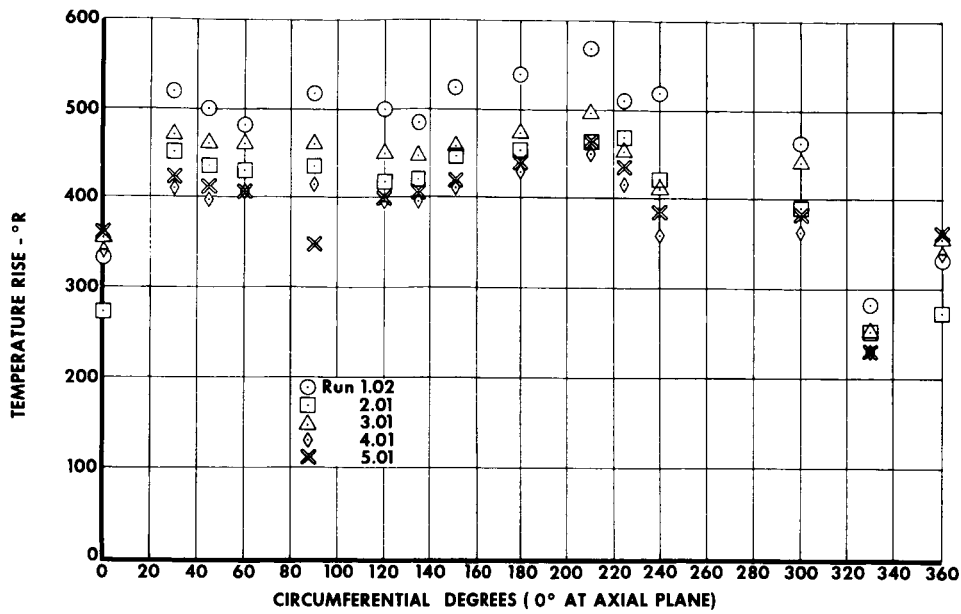


Figure 44. Triplet Injector — Facing Injector
From Exit (Axial Plane at Throat,
 $t = 3.5$)

GS 6763

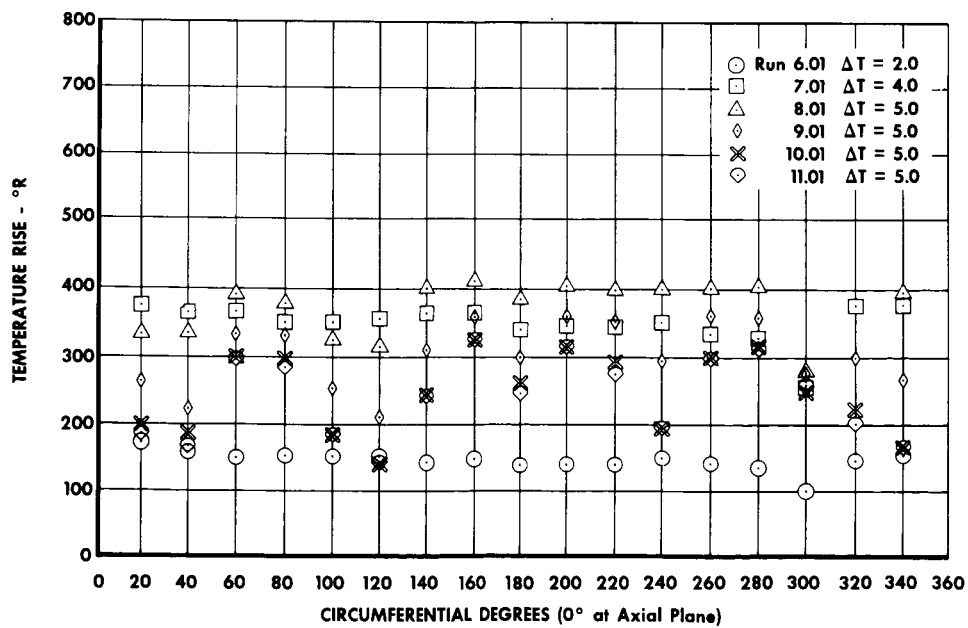


Figure 45. Coaxial Injector — Facing Injector
From Exit (Axial Plane 3 in. From
Injector Face)

GS 6764

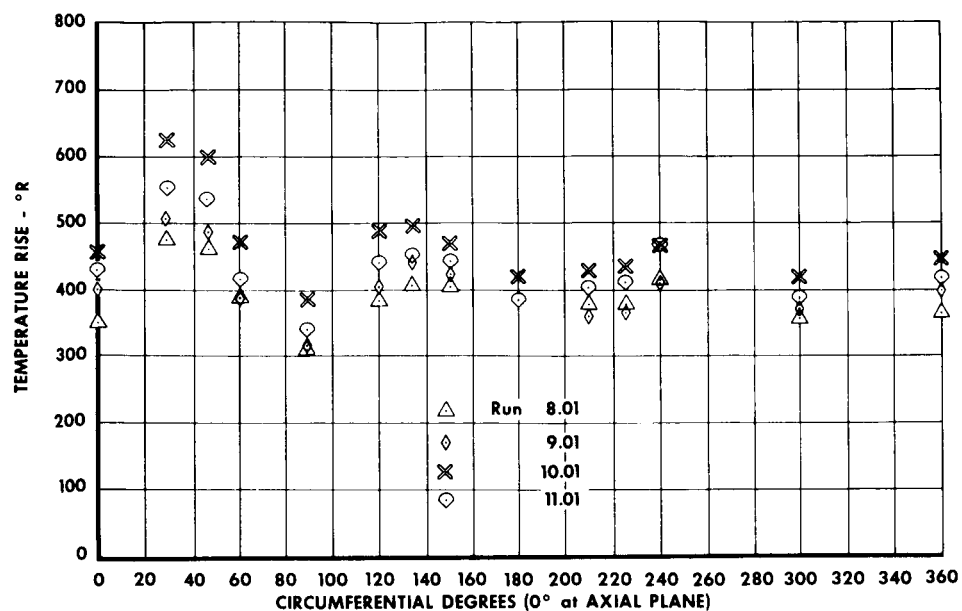


Figure 46. Coaxial Injector — Facing Injector
From Exit (Axial Plane at Throat)

GS 6765

SECTION VI

UNCOOLED ALTITUDE TESTING — TASK III

A. TEST DESCRIPTION

Twenty-five flox/methane firings were completed providing data over a mixture ratio range of 4.1 to 5.9. The oxidizer was liquid flox (82.6% fluorine), and the fuel was ambient gaseous methane. These tests produced chamber and nozzle heat transfer data subsequently used in the steady-state analysis for the cooled RL10 chamber design, and provided the most extensive flox/methane altitude performance data obtained to date. The contour of the uncooled chamber and the bell-nozzle extension were identical to the cooled RL10 chamber used for Task III cooled testing. A second chamber, with a 15-deg half-angle nozzle, was also tested providing a comparison of the kinetic performance losses due to nozzle design. Both nozzle extensions had expansion area ratios of 40. The copper chambers tested were instrumented with thermocouples to provide axial and circumferential heat flux data. The bell-nozzle extension also had thermocouple instrumentation to provide exhaust-nozzle heat flux data. A Kistler pressure transducer in the second chamber (with the 15-deg nozzle) provided combustion stability data. A detailed description of the hardware is presented in Section III. A steam-driven diffuser system was used to provide an ambient exhaust pressure below the nozzle separation level, at 0.1 to 0.5 psia during the firings.

B. PERFORMANCE

The uncooled simulated altitude testing consisted of 25 firings, 23 of which lasted the programmed duration, and 2 of which were aborted after ignition due to insufficient altitude system steam supply. Both the coaxial and triplet injector configurations were tested with the uncooled copper chamber using the bell-nozzle extension. The triplet was also tested with the 15-deg conical nozzle extension. Table 8 presents the measured data from the uncooled altitude testing. Table 9 shows the calculated performance data and table 10 presents calculated data for correlation of the injector performance.

TABLE 8. SUMMARY OF UNCOOLED ALTITUDE TESTS

Test No.	Injector	Chamber	Test Duration, sec	P _c , psia	F, lb	\dot{w}_o , lb/sec	\dot{w}_f , lb/sec	T _o , °R	T _f , °R	ΔP_o , psi	ΔP_f , psi	Remarks
1 UA	Concentric	30-deg Bell	5.0	102.0	5214	11.5	2.54	165	495	30	99	
2 UA			5.0	96.6	4913	11.6	2.28	163	495	28	84	
3 UA			5.0	94.7	4792	11.8	2.08	160	496	27	73	
4 UA			5.0	95.3	4823	11.8	2.16	160	493	25	76	
5 UA	Triplet	30-deg Bell	4.0	97.2	5211	11.4	2.52	174	497	55	102	Unstable Altitude System Abort
6 UA			1.5									
7 UA			5.0	98.2	5159	11.6	2.28	165	495	28	63	Unstable
8 UA			5.0	96.8	5102	12.0	2.08	160	492	31	53	Unstable
9 UA			5.0	98.2	5210	11.7	2.33	163	493	32	63	Unstable
10 UA			5.0	97.6	5161	11.9	2.17	162	488	34	55	Unstable
11 UA			1.6									Altitude System Abort
12 UA			4.0	95.0	5128	11.4	2.43	164	513	48	104	Unstable
13 UA			4.0	97.2	5156	11.2	2.61	162	512	29	85	Unstable
14 UA			4.0	98.7	5237	11.2	2.71	166	519	27	91	Unstable
15 UA			4.0	93.9	4925	11.7	1.99	166	517	31	60	Unstable
16 UA			4.0	95.5	5045	11.5	2.18	162	513	32	66	Unstable
17 UA	Triplet	15-deg Conical	4.0	96.9	5331	11.3	2.74	166	512	44	114	Unstable
18 UA			4.0	98.1	5324	11.5	2.42	164	510	33	73	Unstable
19 UA			4.0	88.5	4642	10.4	2.06	167	511	28	53	Unstable
20 UA			4.0	97.3	5252	11.7	2.18	165	513	32	63	Unstable
21 UA			4.0	96.9	5239	11.6	2.31	164	514	37	76	Unstable
22 UA			4.0	95.8	5203	11.7	2.09	163	514	35	60	Unstable
23 UA			4.0	97.6	5174	11.8	2.17	164	511	31	63	Unstable
24 UA			4.0	96.3	5152	11.8	2.07	163	511	32	58	Unstable
25 UA			4.0	95.6	5099	11.8	2.01	163	511	33	56	Unstable

TABLE 9. CALCULATED PERFORMANCE DATA FOR UNCOOLED ALTITUDE TESTS

Test No.	r	\dot{w}_p , lb/sec	c^*_{11} , ft/sec	I_{vac} , sec	I_{vac} , sec	I_{vac} , sec	$c^*_{P_c}$, ft/sec	$c^*_{F_c}$, ft/sec	$\eta_{c^*P_c}$ (2)	η_{c^*F}	$\eta_{c^*P_c}(cor)$ (3)	$\eta_{c^*F}(cor)$ (4)	$\eta_{I_{vac}}$	$\eta_{I_{vac}}(cor)$	$C_{F_{vac}}$	$\eta_{CF_{vac}}$	$\eta_{CF_{vac}}(cor)$ (5)	ΔT , sec
1 UA	4.53	14.04	6912	412	371	371	6734	6403	0.974	0.926	0.959	0.930	0.902	0.910	1.774	0.925	0.944	3.5
2 UA	5.10	13.88	6974	417	353	354	6439	6076	0.923	0.871	0.909	0.875	0.848	0.855	1.765	0.918	0.916	3.3
3 UA	5.65	13.88	6996	421	346	347	6341	5920	0.906	0.847	0.893	0.850	0.822	0.829	1.756	0.908	0.913	3.1
4 UA	5.47	13.96	6993	419	346	347	6336	5932	0.906	0.848	0.891	0.852	0.825	0.832	1.757	0.911	0.935	3.2
5 UA	4.52	13.92	6906	412	376	379	6495	6474	0.941	0.938	0.929	0.944	0.912	0.926	1.860	0.970	0.989	2.3
6 UA	5.11	13.88	6975	417	371	374	6554	6388	0.940	0.916	0.931	0.922	0.891	0.903	1.823	0.948	0.964	3.3
7 UA	5.77	14.08	6991	421	363	365	6377	6204	0.912	0.887	0.901	0.892	0.862	0.873	1.830	0.947	0.963	4.4
8 UA	5.04	14.03	6969	416	370	373	6471	6373	0.929	0.914	0.919	0.919	0.890	0.901	1.841	0.958	0.973	3.3
9 UA	5.48	14.07	6995	419	366	369	6427	6283	0.919	0.898	0.910	0.903	0.874	0.884	1.835	0.951	0.966	3.5
10 UA	4.69	13.83	6929	413	370	372	6362	6385	0.918	0.921	0.905	0.926	0.896	0.904	1.873	0.976	0.995	2.0
11 UA	4.28	13.81	6867	409	374	375	6539	6450	0.952	0.939	0.939	0.943	0.914	0.924	1.840	0.960	0.977	2.0
12 UA	4.11	13.91	6840	408	378	378	6598	6516	0.965	0.953	0.949	0.956	0.927	0.935	1.862	0.961	0.980	2.0
13 UA	5.88	13.69	6972	418	360	361	6355	6168	0.912	0.885	0.899	0.888	0.860	0.868	1.821	0.944	0.961	2.0
14 UA	5.25	13.68	6985	418	370	371	6491	6358	0.929	0.910	0.917	0.914	0.886	0.893	1.834	0.953	0.970	2.0
15 UA	4.12	14.04	6839	408	380	381	6393	6557	0.935	0.959	0.920	0.962	0.933	0.941	1.913	0.998	1.018	2.0
16 UA	4.77	13.92	6940	414	382	382	6519	6384	0.939	0.949	0.927	0.953	0.923	0.931	1.886	0.983	1.000	2.0
17 UA	5.05	12.46	6961	416	373	375	6415	6415	0.945	0.922	0.930	0.925	0.896	0.905	1.824	0.949	0.968	2.0
18 UA	5.37	13.88	6993	419	379	380	6498	6502	0.929	0.930	0.915	0.934	0.905	0.912	1.876	0.974	0.993	2.0
19 UA	5.02	13.91	6968	416	377	378	6455	6487	0.926	0.931	0.915	0.935	0.906	0.913	1.879	0.978	0.994	2.0
20 UA	5.61	13.79	6999	421	377	377	6425	6450	0.918	0.922	0.906	0.925	0.895	0.903	1.888	0.977	0.993	2.0
21 UA	5.43	13.97	6995	419	370	371	6461	6346	0.924	0.907	0.909	0.911	0.883	0.890	1.842	0.956	0.975	2.0
22 UA	5.72	13.87	6996	421	371	371	6418	6433	0.917	0.907	0.905	0.910	0.881	0.888	1.860	0.962	0.979	2.0
23 UA	5.86	13.81	6977	419	370	372	6412	6336	0.919	0.908	0.907	0.912	0.883	0.891	1.855	0.962	0.978	2.0

- (1) Corrected for chamber heat loss, and adjusted to correspond to liquid methane performance.
(2) Based on injector face pressure measurements.
(3) Corrected for momentum loss, throat growth, and chamber heat loss.
(4) Corrected for heat loss only.
(5) Corrected for heat loss and throat growth.

TABLE 10. INJECTOR PERFORMANCE COMPARISON FOR UNCOOLED ALTITUDE TESTS

Test No.	Injector	\dot{w}_o , lb/sec	\dot{w}_f , lb/sec	ACd _o	ACd _f	V _o	V _f	$\dot{w}_o V_o$	$\dot{w}_f V_f$	V _f /V _o	$\dot{w}FF_f/\dot{w}_o V_o$	$\eta_c^* P_c$ (cor)	r
1 UA	Concentric	11.5	2.54	0.36	0.7187	53.4	1322.4	614	3361	24.8	5.47	0.959	4.53
2 UA		11.6	2.28		0.7137	53.5	1318.9	623	3008	24.6	4.83	0.909	5.10
3 UA		11.8	2.08		0.7037	54.4	1274.2	640	2653	23.4	4.15	0.893	5.65
4 UA		11.8	2.16		0.7063	54.2	1289.7	639	2781	23.8	4.35	0.891	5.47
5 UA	Triplet	11.4	2.52	0.38	0.7212	51.1	1322.8	585	3333	25.9	5.77	0.929	4.52
7 UA		11.6	2.28		0.8049	50.5	1176.7	587	2677	23.3	4.57	0.931	5.11
8 UA		12.0	2.08		0.8038	51.9	1113.6	622	2315	21.5	3.72	0.901	5.77
9 UA		11.7	2.33		0.8313	51.2	1172.1	601	2733	22.9	4.54	0.919	5.04
10 UA		11.9	2.17		0.8203	51.6	1125.8	615	2446	21.8	3.98	0.910	5.48
12 UA		11.4	2.43		0.7039	50.1	1345.4	571	3274	26.9	5.73	0.905	4.69
13 UA		11.2	2.61		0.8217	48.8	1343.6	545	3507	27.6	6.44	0.939	4.28
14 UA		11.2	2.71		0.8315	49.4	1352.7	551	3669	27.4	6.66	0.949	4.11
15 UA		11.7	1.99		0.7595	51.8	1201.4	606	2389	23.2	3.94	0.899	5.88
16 UA		11.5	2.18		0.7814	50.1	1240.7	573	2705	24.8	4.72	0.917	5.25
17 UA	Triplet	11.3	2.74	0.38	0.7508	49.8	1344.1	562	3685	27.0	6.55	0.920	4.12
18 UA		11.5	2.42		0.8165	49.5	1266.0	570	3059	25.6	5.36	0.927	4.77
19 UA		10.4	2.06		0.8562	44.7	1173.2	465	2416	26.2	5.20	0.930	5.05
20 UA		11.7	2.18		0.7892	51.5	1216.0	602	2648	23.6	4.40	0.915	5.37
21 UA		11.6	2.31		0.7610	50.7	1262.9	588	2916	24.9	4.96	0.915	5.02
22 UA		11.7	2.09		0.7814	51.3	1197.0	601	2502	23.4	4.17	0.906	5.61
23 UA		11.8	2.17		0.7843	52.0	1205.1	614	2619	23.2	4.27	0.909	5.43
24 UA		11.8	2.07		0.7780	51.7	1176.2	612	2430	22.7	3.97	0.905	5.72
25 UA		11.8	2.01		0.7758	51.6	1162.9	608	2337	22.6	3.85	0.907	5.86

Figures 47, 48, and 49 show the characteristic velocity (c^*), vacuum specific impulse (I_{vac}), and thrust coefficient (C_F) data obtained as a function of mixture ratio for the coaxial injector. The c^* values obtained agree with the Task II sea level results, and the measured thrust coefficient data agree to within 0.5% with previous flox/methane simulated altitude data reported in Reference 2. The maximum corrected vacuum specific impulse was 371 at a mixture ratio of 4.5. The trend of the data indicates that even higher impulses could have been achieved at lower mixture ratios. Note that the corrected data shown are referenced to liquid methane. This is done for the sake of consistency with the regenerative cooled data presented in Section VII. Based on the actual inlet conditions (ambient temperature methane) and corrected for heat loss, the vacuum specific impulse would be approximately 3 sec higher. As discussed in the previous section, the low c^* at high mixture ratio with the coaxial injector was due partially to use of ambient temperature gaseous methane, which provided a momentum ratio well below the design value.

Results of the nineteen tests for which performance data were obtained with the triplet injector are presented in figures 50, 51, and 52. The characteristic velocity data, shown in figure 50, are indicated to be from 1 to 5% lower than the sea level data presented in Section V; however, all of these tests encountered high frequency instability. Between the sea level and altitude tests, seventy-two 0.035-in. film-cooling holes were added to the circumference of the injector to reduce chamber heat flux. The effect on performance of this small amount of film cooling should have been minimal; however, the reduction in injector fuel pressure drop and change in injector mass distribution were apparently enough to produce instability. In previous testing with similar injectors, it was found that acoustic instability reduced the indicated c^* based on measured chamber pressure, but had no effect on the sea level thrust (Reference 2), and this was apparently the case with these tests.

Figure 51 shows the vacuum specific impulse test data and figure 52 shows the indicated thrust coefficient efficiency. The thrust coefficient efficiencies are seen to be as much as 4.5% above the maximum values predicted to be attainable based on estimated friction and divergence losses, thereby providing a strong indication that the indicated c^* data are in error. If a constant value of 95% η_c^* (as determined from the sea level testing) is applied to the vacuum impulse data, the thrust coefficient efficiencies shown in figure 53 are obtained. These values are much more realistic and are in better agreement with the coaxial data which are shown for comparison.

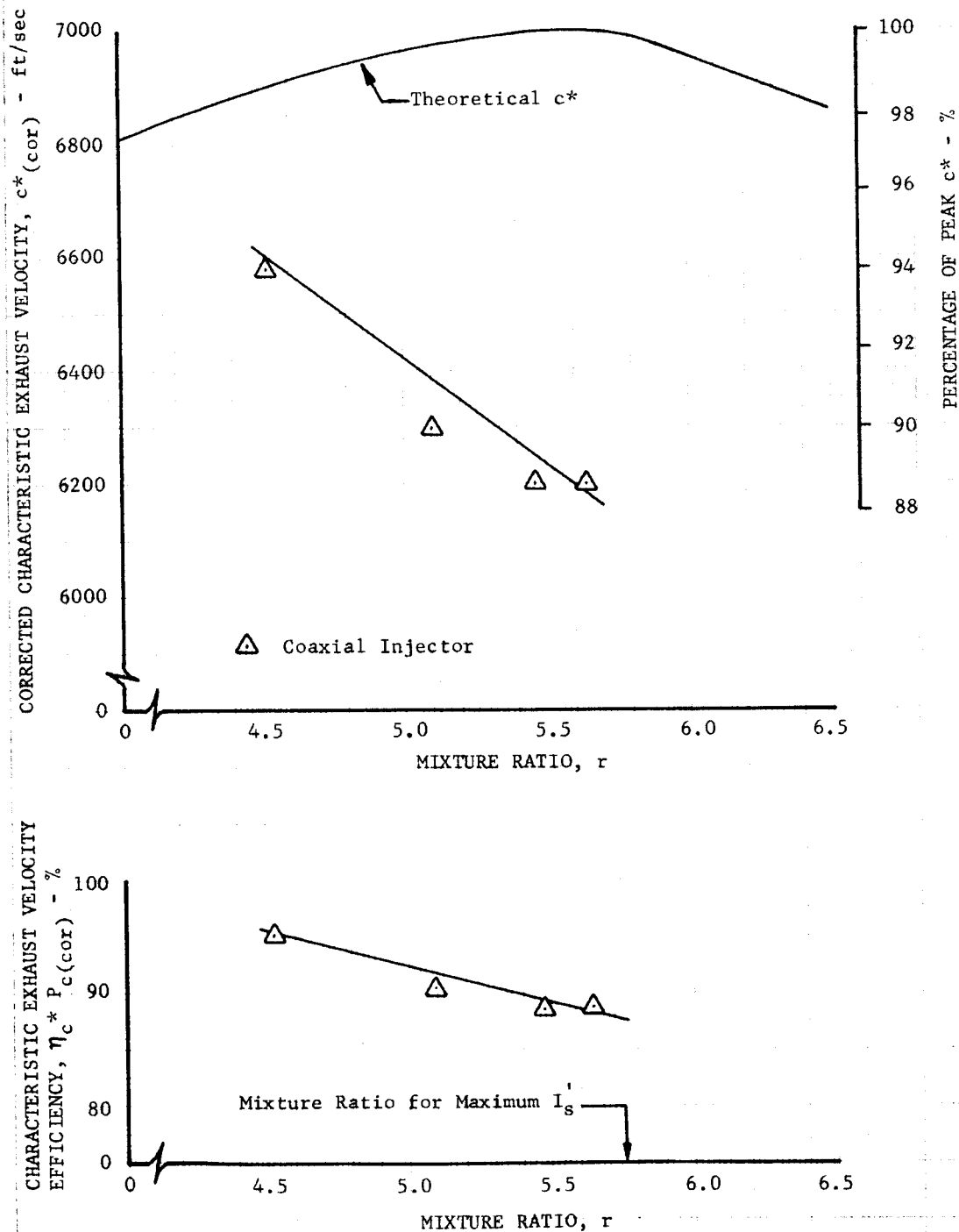


Figure 47. Coaxial Injector - Characteristic Exhaust Velocity

DF 65067

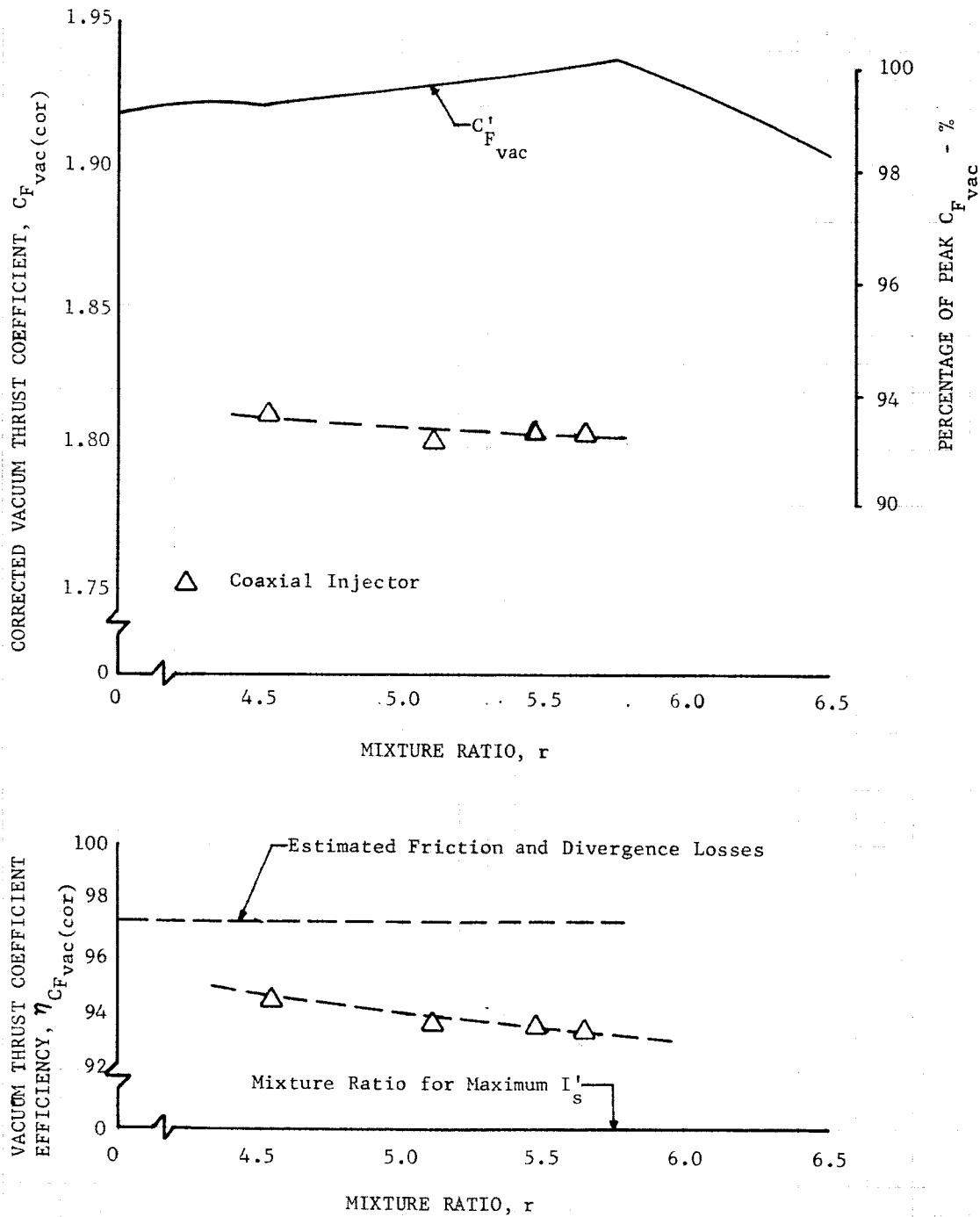


Figure 48. Coaxial Injector - Vacuum Thrust Coefficient

DF 65068

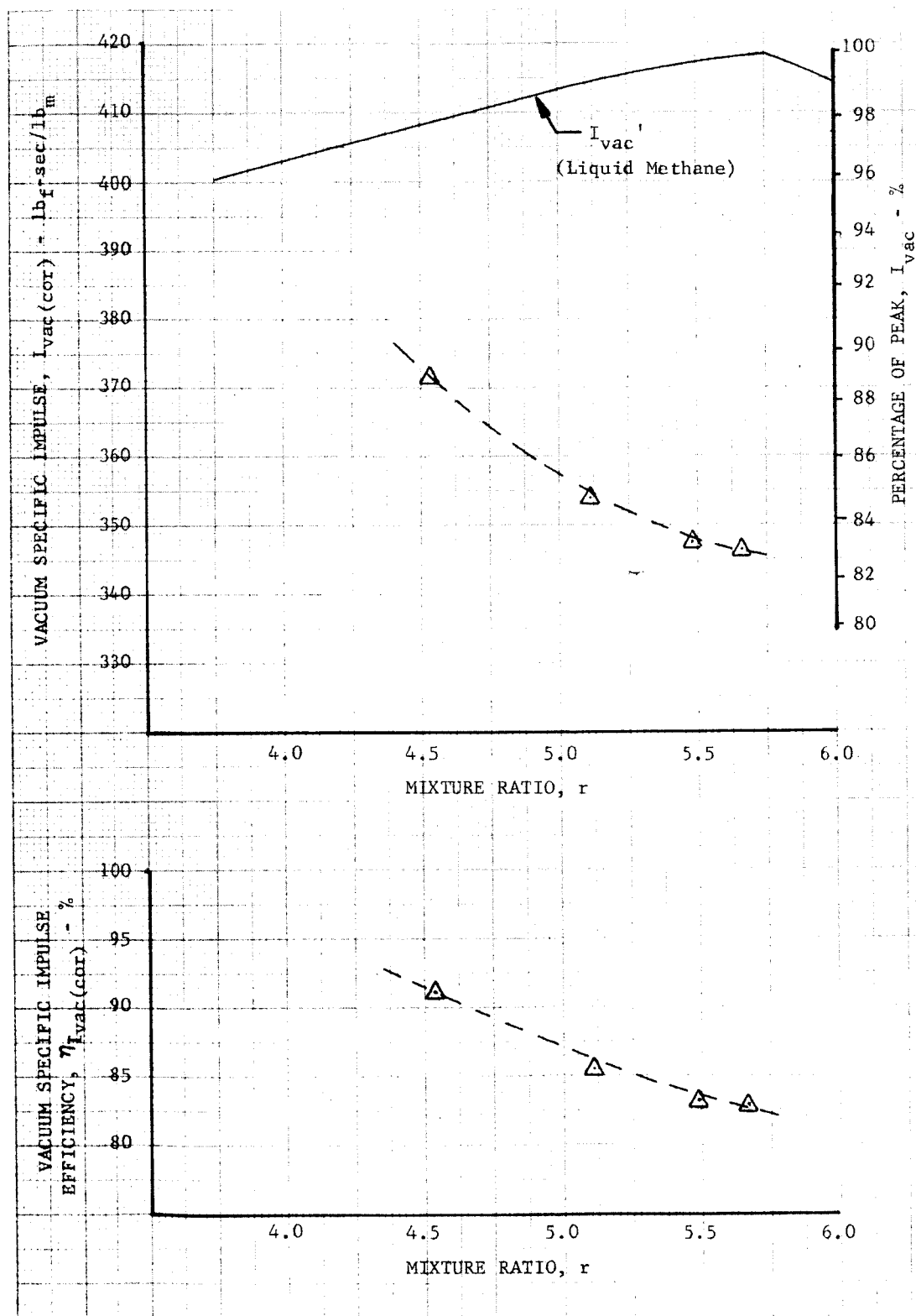


Figure 49. Coaxial Injector - Vacuum Specific Impulse

DF 65069

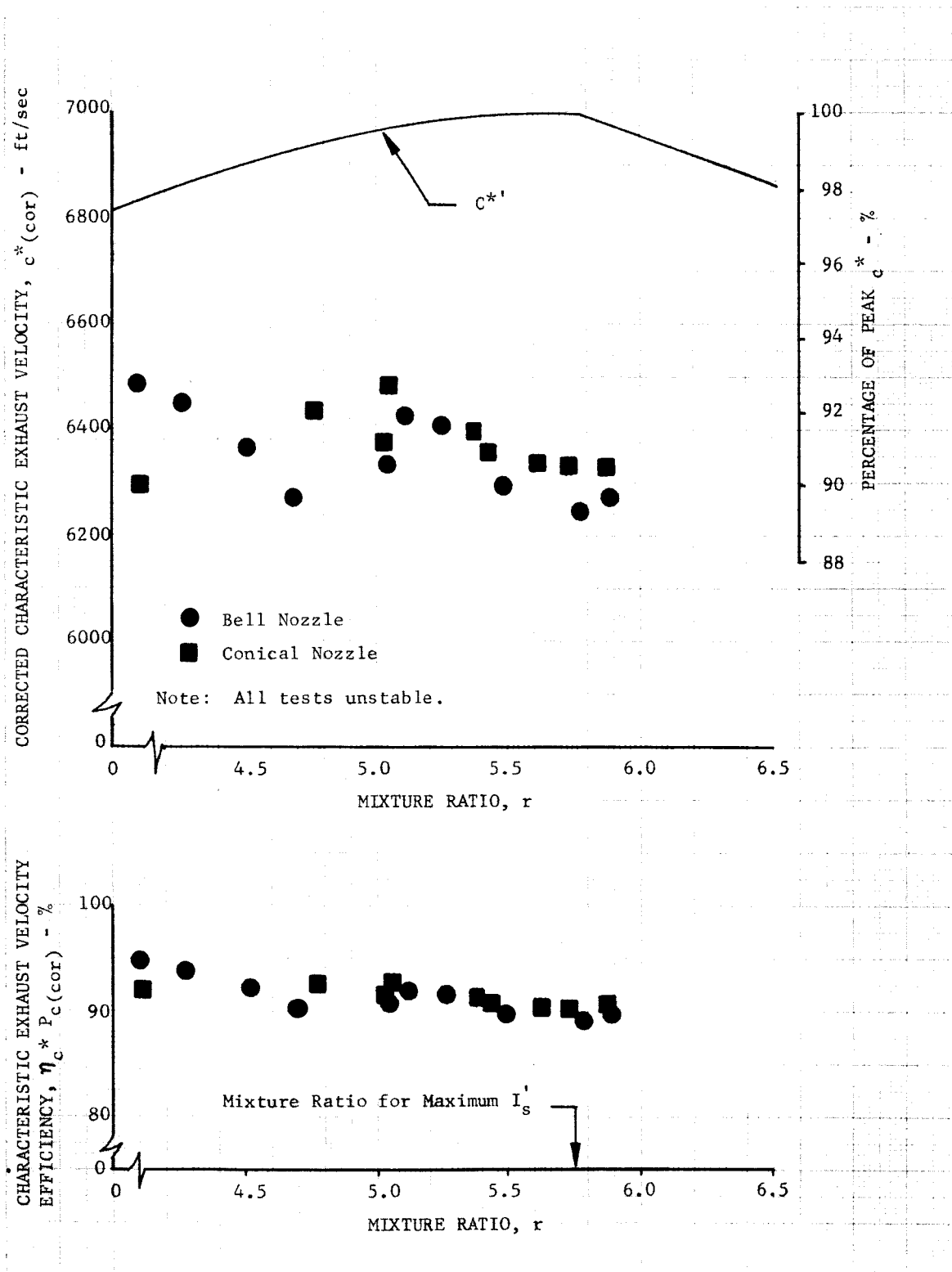


Figure 50. Triplet Injector - Characteristic Exhaust Velocity

DF 65070

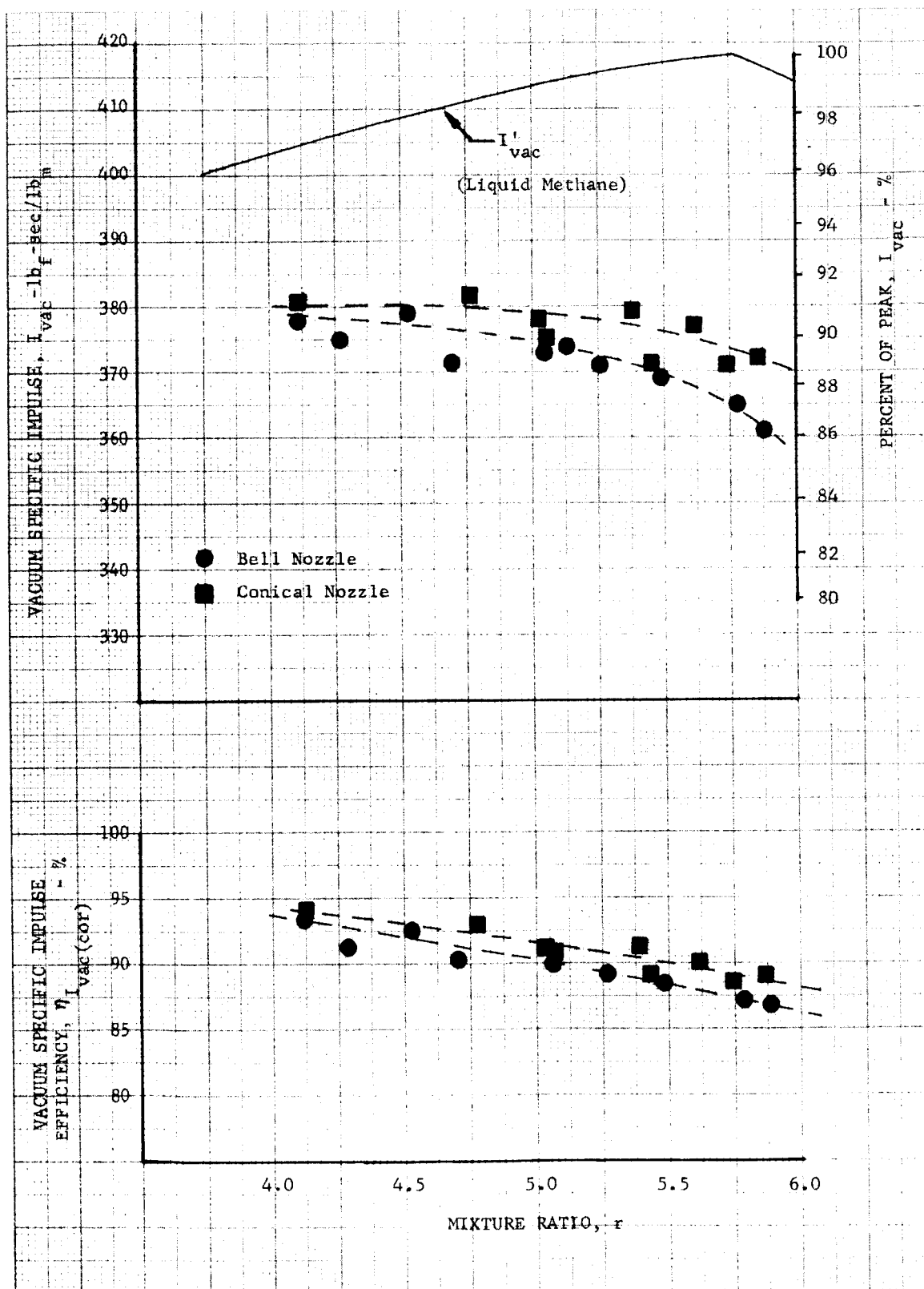


Figure 51. Triplet Injector - Vacuum Specific Impulse

DF 65071

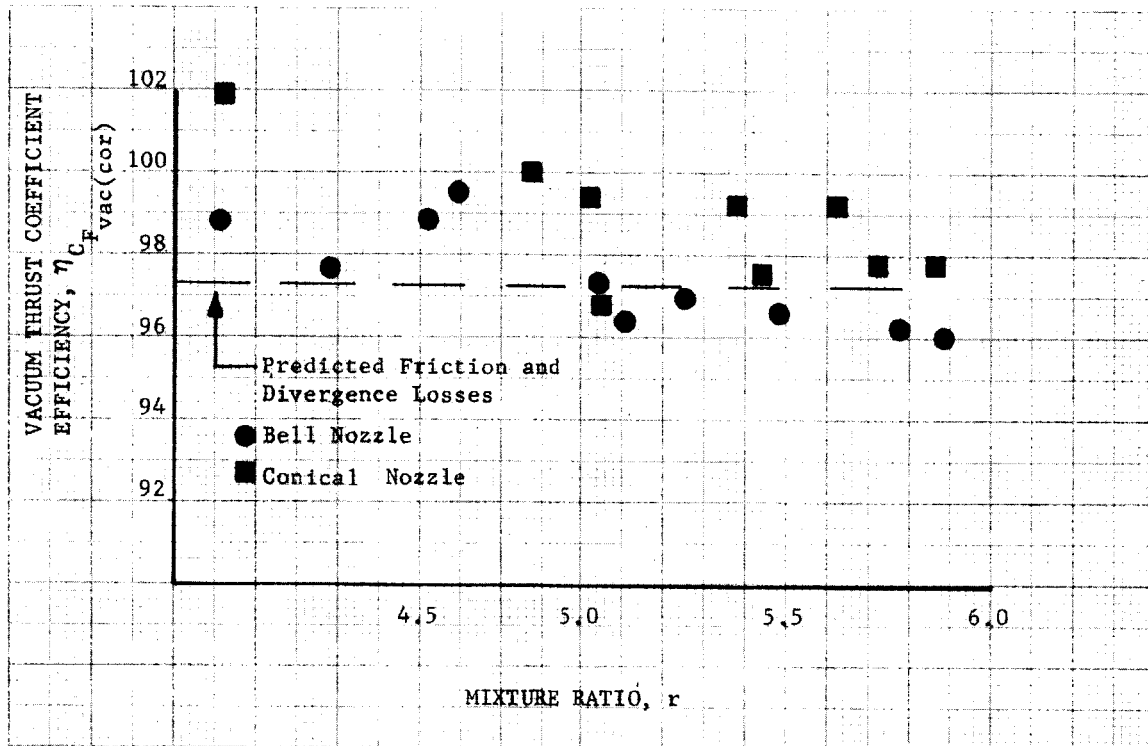


Figure 52. Triplet Injector - Measured Vacuum Thrust Coefficient

DF 65086

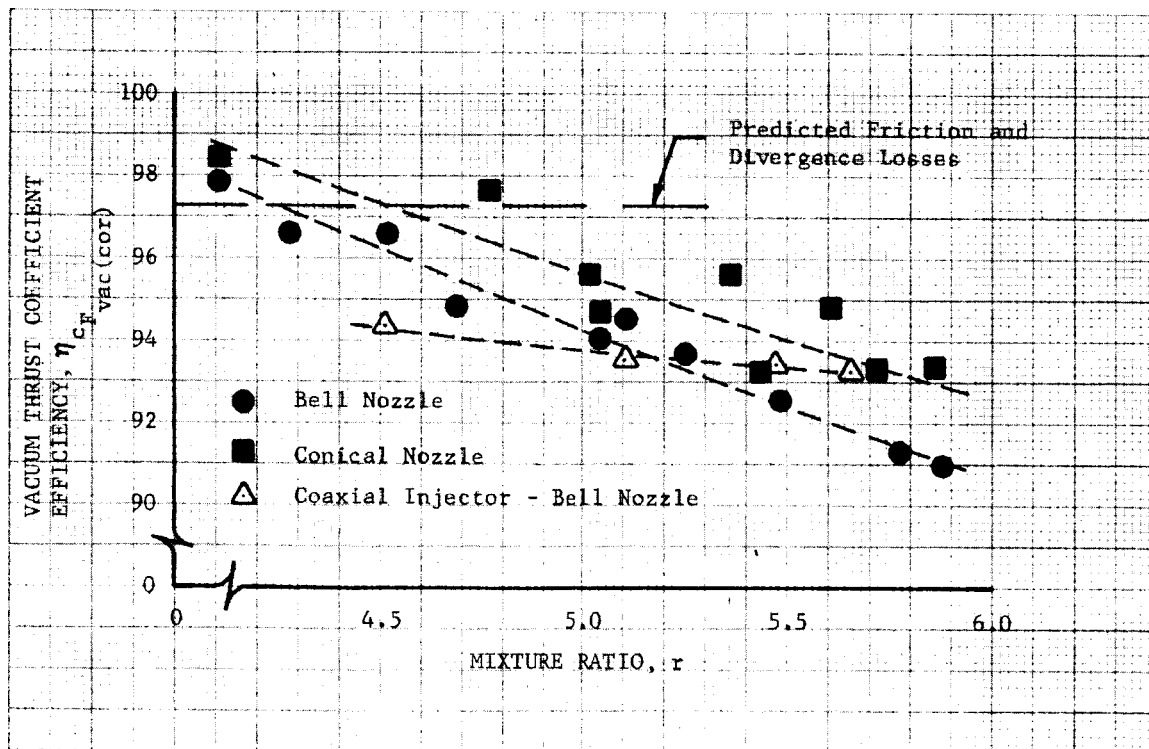


Figure 53. Estimated Triplet Injector Vacuum Thrust Coefficient Based on Constant 95% η_c^* (Measured Coaxial Injector $\eta_c^* F_{\text{vac}}$ Included for Comparison)

DF 65072

The stable coaxial injector thrust coefficient data and unstable triplet data shown in figure 53 indicate that nozzle losses in excess of predicted friction and divergence losses are less than 3.0% below a mixture ratio of 4.5 and less than 6% for the bell nozzle at a mixture ratio of 5.75. These losses are commonly attributed entirely to nonequilibrium chemical recombination, but the effect of combustion efficiency on nozzle performance must also be considered as a possible influence. Previous analytical predictions of nonequilibrium losses (Reference 2) were much higher than indicated by figure 53, e.g., 7% at $r=4.5$ and 10% at $r=5.75$. However, serious doubt has always existed regarding these analytical predictions because of the inadequacy of the available reaction rate data.

While the acoustic instability may leave some doubt regarding the distribution of the c^* and C_F efficiencies, there appears to be no basis for questioning the vacuum specific impulse data shown in figure 51. The peak values of 379 with the bell nozzle and 382 with the conical nozzle (379 and 380 based on a best fit of the data) are more than 10 sec higher than the best previous data obtained (Reference 2) and indicate that much better low pressure performance can be obtained with flox/methane than previously thought possible.

SECTION VII

REGENERATIVELY COOLED ALTITUDE TESTS

A. TEST DESCRIPTION

Seven cooled chamber tests were conducted using the modified RL10 thrust chamber and concentric element injector. As in the uncooled firings, nominal test conditions were 5000-lb vacuum thrust and 100-psia chamber pressure. The first four tests were supplementary cooled, i.e., gaseous ambient temperature methane was used as the fuel and a separate supply of liquid methane was used for cooling. In these tests the coolant flow was initially set approximately 50% in excess of the fuel flow and was systematically reduced to a value equal to the fuel flow. The final three firings were regeneratively cooled.

1. SUPPLEMENTARY-COOLED TESTS

The coolant-valve sequencing in test 1 CA provided for a 9.0-second coolant lead to assure stabilized coolant flow, followed by full fuel flow and a 2.0-second ramp-up in oxidizer flow. A fourth control valve was provided on the cooling jacket discharge line to control the coolant pressure in the jacket. During the start transient this valve was maintained at a fixed position of 70%. This was the calculated position to provide 150-psia jacket pressure during steady-state operation. The valve was kept open with low coolant back pressure to allow escape of the excess coolant in the jacket during the start transient as the coolant density decreased because of heat addition. Fixing the position at 70% would prevent the jacket pressure from becoming too low as steady-state operation was approached.

Test 1 CA was automatically aborted 2.1 seconds into the run because of low indicated coolant flow to the jacket. The indicated coolant flow to the chamber at this time was 1.5 lb/sec. The low coolant flow was produced by high jacket pressures, which reached a peak value of 280 psia at the jacket discharge. The calculated jacket exit flowrate at this time was in excess of 10.0 lb/sec, based on the measured discharge control valve pressure drop. The data clearly indicate that the jacket discharge control valve was unable to accommodate the increased discharge flowrate produced by the sudden coolant density decrease within the coolant jacket and discharge plumbing. This is understandable considering that the reduction in coolant density between prestart and steady-state operation is sufficient to produce a reduction in coolant mass, within the coolant jacket alone, of approximately 10 lb. However, prior to test 1 CA it was expected that the density reduction would occur more gradually.

Inspection of the thrust chamber after test 1 CA indicated 9 tubes had small holes burned through near the injector face. These holes were easily repaired before subsequent testing.

On test 2 CA the oxidizer flow ramp was extended to 10.0 seconds to provide a more gradual change in coolant density, and the coolant discharge control valve was set at 100% open during the start transient to provide less of a restriction to the high coolant discharge flow. The coolant flow lead before start was reduced to 6.0 seconds. A successful start was achieved and the test ran the programmed duration of 20 seconds.

Planned coolant flows for test 2 CA were 3.4 lb/sec for the first 15 seconds and 2.8 lb/sec for the last five seconds; however, cooling system pressure drops prevented the 3.4 lb/sec flowrate from being achieved even with the control valve wide open; therefore, coolant flow during steady-state operation ranged from 2.8 to 3.1 lb/sec. No hardware damage was encountered on this test.

Two additional supplementary cooled tests, tests 3 CA and 4 CA, were conducted using the same start sequence as test 2 CA. Test 3 CA was a 20-second firing, covering a mixture ratio range of 4.0 to 5.5 at a coolant flowrate of approximately 3.0 lb/sec. Test 4 CA was a 30-second firing covering a mixture ratio range of 4.0 to 5.5 at a coolant flow of 2.8 to 2.0 lb/sec. No hardware damage was encountered on test 3 CA; however, after test 4 CA four tubes were observed to have small holes. Closer inspection of the chamber during repair and pressure check located numerous pinhole leaks in 15 to 20 tubes. Damage was located primarily at the start of the convergent section of the chamber.

2. *REGENERATIVE COOLED TESTS*

For test 5 CA the jacket coolant discharge line was connected to the injector fuel inlet to provide conventional regenerative cooling. A tee in the discharge line to the coolant discharge control valve used in the supplementary cooled tests provided a means of bleeding off excess jacket discharge flow during the start transient. This overboard dump valve was set at 70% open for 4.0 seconds after start and then ramped closed over the next 5.0 seconds. A 5.0-second coolant lead before start was used, and the oxidizer control valve was ramped open over a 10-second period in the same manner as tests 2 CA, 3 CA, and 4 CA.

Test 5 CA was aborted at 9.0 seconds after start because of low coolant flow. As with test 2 CA, it was determined that the coolant discharge pressure became excessive as the decrease in coolant density within the jacket produced a high flowrate out of the jacket. No hardware damage was encountered.

For test 6 CA, the 10-second oxidizer ramp was modified to provide a more linear increase in chamber pressure and the coolant dump valve was scheduled to ramp closed from start plus 5 seconds to start plus 15 seconds.

These changes were made to provide a more gradual increase in heat flux (hence a more gradual decrease in jacket coolant density) and to provide increased overboard coolant dump during the critical period from start plus 7.0 seconds to start plus 10.0 seconds. A successful start was achieved and the test ran the programmed duration of 40.0 seconds. During the test a mixture ratio excursion was made from 4.6 to 5.0, the highest value being achieved at the end of the firing.

During test 6 CA, approximately fifty tubes sustained minor damage, consisting of pinhole leaks and short splits in the tubes. The damage was concentrated near the start of the nozzle convergent section. The total leakage area in the damaged tubes was so small that the test data provide no clear indication as to when burnout occurred; however, the most likely time was during the maximum mixture ratio operation at the end of the test. The hardware was again repaired for use in test 7 CA, and the tubes were coated with silver braze in the combustion chamber to increase the cooling margin in that area.

Test 7 CA was made with the repaired chamber. The test ran the scheduled 60 seconds and a mixture ratio excursion from 4.3 to 5.0 was completed; however, the chamber was damaged severely during the start transient. Despite the damage the run continued with chamber pressure stable at approximately 60 psia instead of the desired 100 psia. Post-run inspection of the chamber revealed damage to nearly all of the tubes in the combustion area (the region from about 2 inches from the injector face to the convergent nozzle section). Coincidental with the tube damage, there was a complete absence of the silver braze filler. There was no damage to the throat or the divergent nozzle section of the chamber, nor was there any damage to the injector. No changes had been made to the valve sequencing after test 6 CA that would affect either the start or shutdown transients.

Several factors probably contributed to the chamber failure. Each time the chamber tubes are repaired the question of structural integrity arises, but worth noting is the fact that subsequent tube damage was not in the area of the previous weld repairs (although in some cases there was damage in the same tube at a different axial location). The presence of silver braze in the combustion area presents another variable. Obviously, the theory of using silver to conduct heat from the tube crown to the cooler region between the tubes is sound. The problem is that normal application of the silver braze leaves a buildup similar to a weld bead. This, in turn, would tend to make the boundary layer more turbulent than the smooth chamber wall, which could thereby increase heat transfer rates. Smooth braze application and polishing of the braze material was hampered by the extent of the prior tube repair. Also, under low pressure test conditions, the silver braze melts at a temperature very close to the point of

zero tube wall margin. The braze surface temperature will be approximately the same as the tube crown temperature without braze. Thus, for the silver braze to be effective it must remain solid above the point of zero wall margin as is the case with higher pressure operation (lower tube temperature at zero wall margin).

The severity of the damage encountered during test 7 CA was attributed to a brief period of high frequency instability, which occurred approximately 9.0 seconds into the run. The data show that the chamber failure began about 7.0 seconds into the run, but became severe only after the instability occurred. It is concluded that minor tube damage triggered the instability, which, in turn, caused the more extensive tube failure.

One of the most interesting results of the cooled testing was the minimization of the thrust chamber damage through the use of metering orifices for tube-to-tube flow control. On previous cooled tests with flox-light hydrocarbon propellants, extensive damage was encountered any time a tube failure occurred. The severity of the damage was caused by starvation of coolant in some tubes as flowrate became excessive through the burned tubes. With the use of metering orifices, the slight damage incurred on tests 1, 4, and 6 CA did not lead to severe chamber failure and was readily repaired. Even more impressive was the chamber operation during test 7 CA. Even though the chamber damage incurred during the start transient caused over 90% of the fuel to be diverted through the damaged tubes, the chamber continued to operate without catastrophic failure at over 60% impulse efficiency for 60 seconds. A post-test photograph of the chamber is shown in figure 54. It can be seen that development of tube-to-tube coolant flow control could prove to be a significant contribution to mission safety and reliability in future rocket engines.

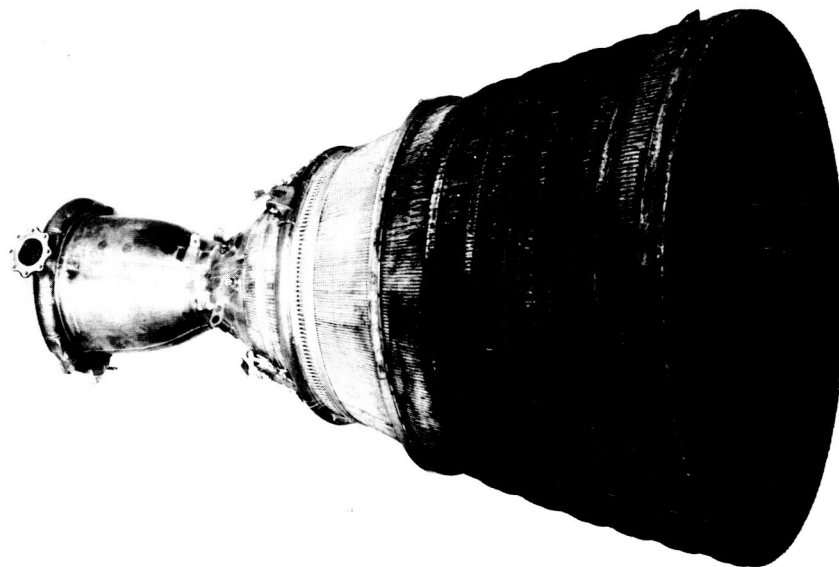


Figure 54. Post-Test View of RL10 Thrust Chamber

GS 7940

B. COOLED CHAMBER PERFORMANCE

Tables 11 and 12 summarize the results obtained in the four cooled tests for which steady-state performance data were obtained. In tests 3 CA, 4 CA, and 5 CA, several steady-state performance points were obtained. As predicted, and as shown in figure 55, the characteristic exhaust velocity efficiency, η_c^* , was substantially improved in the regeneratively cooled test (6 CA) because of the increased fuel momentum.

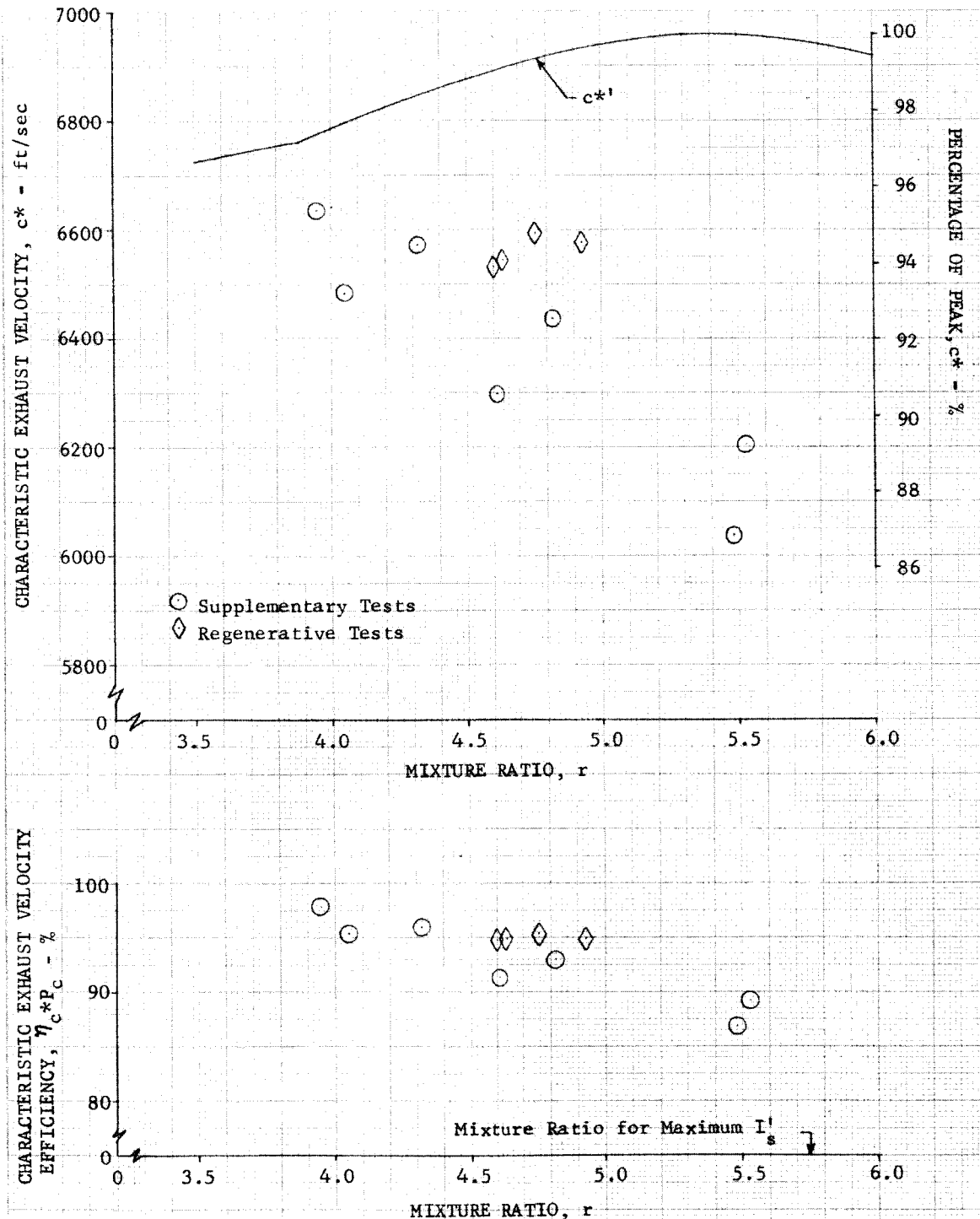


Figure 55. Characteristic Exhaust Velocity Data from Cooled Tests

DF 62643

TABLE II. MEASURED COOLED ALTITUDE TEST DATA

Test No.	Cooling Mode	Test Duration, sec	P _c , psia	F, lb	\dot{w}_o , lb/sec	\dot{w}_f , lb/sec	\dot{w}_c , lb/sec	Coolant Inlet Temperature, °R	Coolant Outlet Temperature, °R	T _o , °R	T _f , °R	ΔP_o , psi	ΔP_f , psi	Remarks
1 CA	Separate													Abort at start, slight tube damage.
2 CA	Separate	20.0	97.3	4767	10.9	2.52	3.01	173	550	174	498	33	84	
3 CA	Separate	20.0	98.4	4847	11.4	2.38	2.96	186	532	168	485	25	75	
			90.7	4446	11.5	2.10	3.07	186	495	183	483	32	62	
			101.8	5064	11.3	2.80	2.90	186	532	157	487	25	93	
4 CA	Separate	30.0	100.6	5015	10.9	2.76	2.21	189	673	170	499	25	97	Small pinhole leaks in approximately 15 tubes.
			91.1	4505	10.7	2.33	2.20	188	695	192	496	53	79	
			92.5	4535	11.4	2.06	2.20	187	610	180	491	27	63	
5 CA	Regenerative	9.0												Abort due to low coolant flow.
6 CA	Regenerative	40.0	97.1	4820	11.0	2.40	*	187	594	183	597	32	109	Small pinhole leaks and splits in approximately 50 tubes. Repaired and silver braze added to combustion chamber for test 7 CA.
			97.9	4891	11.1	2.33	*	187	644	178	650	22	110	
			98.6	4902	11.2	2.41	*	186	682	174	682	26	105	
			98.4	4887	11.2	2.27	*	186	658	172	663	25	99	
7 CA ⁽²⁾	Regenerative	60.0	62.5	3415	11.3	2.33	*	185	560	160	560	27	5	Extensive damage encountered to chamber during start transient.

(1) Values are believed to be in error because of faulty thrust measurement.

(2) Extensive chamber damage was sustained during start transient; values shown are not considered representative.

* Indicates regenerative test.

TABLE 12. CALCULATED PERFORMANCE DATA COOLED ALTITUDE TESTS

Test No.	Injector	r	c^* , ft/sec	I_{vac} , sec	\dot{w}_p , lb/sec	Total Heat Flux, Q , Btu/sec	I_{vac} , sec (1)	$c^*_{p_c}$, sec	$\eta_{c^*p_c}$	$\eta_{c^*p_c}(cor)$	$\eta_{I_{vac}}$ (1)	$C_{F_{vac}}$ (1)	$\eta_{C_{F_{vac}}}$ (1)	ΔT Used, sec
2 CA	Concentric	4.32	6874	410	13.42	993	355	6734	0.980	0.960	0.880	1.6987	0.909	8.1
3 CA		4.82 5.48 4.05	6945 6989 6830	414 419 407	13.78 13.60 14.10	932 887 914	351 328 358	6610 6207 6673	0.952 0.888 0.977	0.930 0.868 0.954	0.854 0.788 0.888	1.7093 1.7005 1.7259	0.914 0.905 0.925	3.0 2.9 3.6
4 CA		3.95 4.61 5.53	6820 6919 6993	406 413 420	13.66 13.03 13.46	857 873 772	367 344 337	6838 6464 6363	1.003 0.934 0.913	0.979 0.914 0.892	0.914 0.842 0.809	1.7281 1.7162 1.6997	0.927 0.918 0.904	4.3 3.0 5.8
6 CA		4.60 4.76 4.64 4.93	6923 6945 6933 6967	413 415 414 416	13.40 13.43 13.61 13.47	818 864 981 860	360 365 361 362	6717 6783 6735 6770	0.970 0.977 0.971 0.972	0.948 0.954 0.949 0.949	0.877 0.888 0.879 0.877	1.7224 1.7324 1.7235 1.7216	0.922 0.927 0.922 0.920	2.7 3.9 4.3 3.0
7 CA (2)		4.86	6943	415	13.33	N/A	249	4000	0.575	0.562	0.607	2.010	1.08	1.0

(1) Values are believed to be in error because of faulty thrust measurement.

(2) Chamber burnout occurred during start transient; values shown are taken at steady-state with extensive chamber damage.

The thrust data for all cooled tests were found to be well below that predicted, based on previous uncooled tests. The problem was determined to be a binding seal between the diffuser and the exhaust nozzle. Figure 56 compares the indicated thrust coefficient efficiency, η_{CF} , for the cooled tests with that measured from previous uncooled tests. All of the flox/methane altitude performance data obtained to date have indicated that, for a given mixture ratio and over the range of η_c^* 's obtained, η_c^* does not have an appreciable effect on η_{CF} . The best estimate of the vacuum specific impulse efficiency for the cooled tests is, therefore, obtained from the product of η_c^* from the cooled tests and η_{CF} from the previous uncooled tests. Vacuum specific impulse and vacuum impulse efficiency calculated in this manner are shown in figure 57.

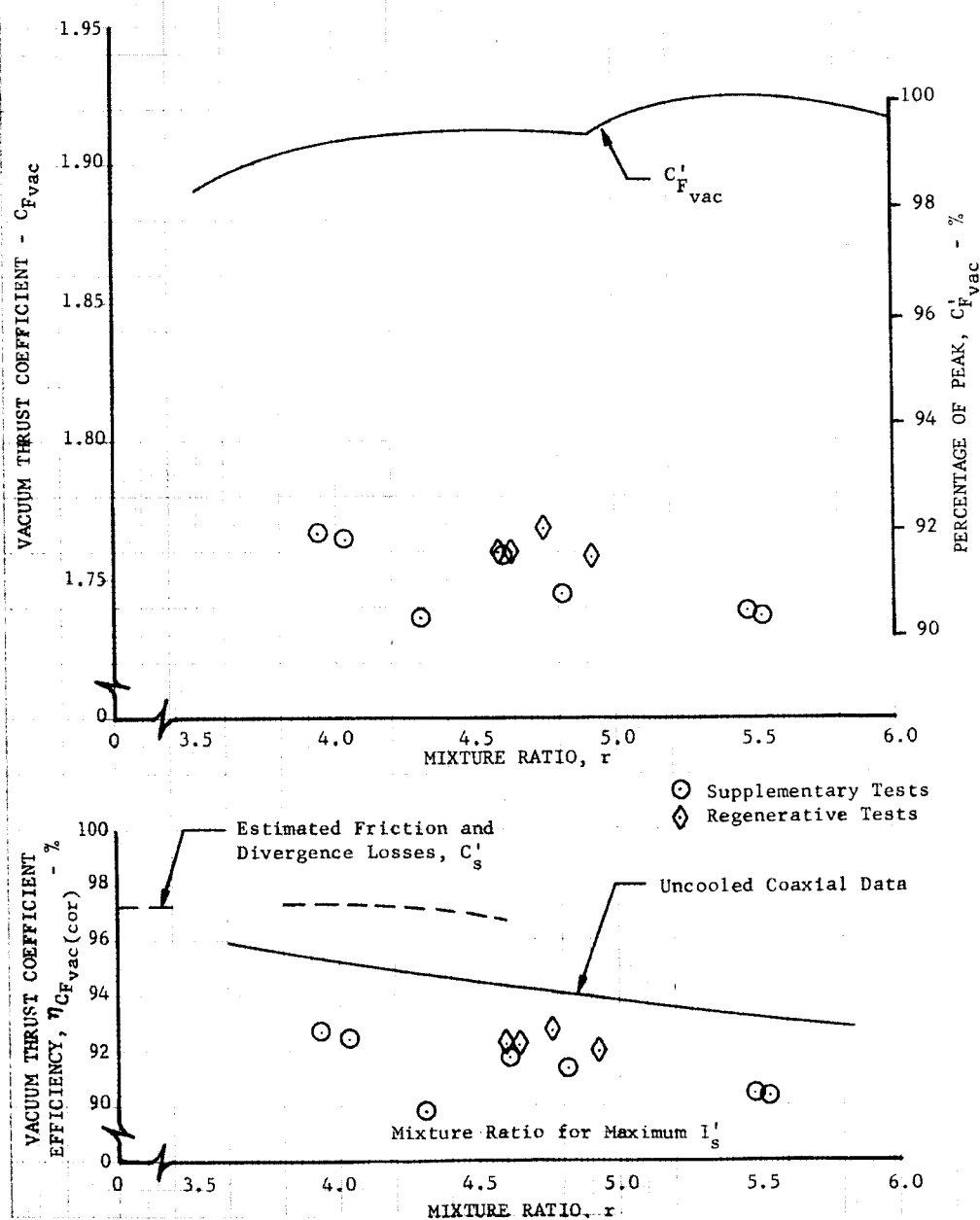


Figure 56. Thrust Coefficient Data From Cooled Tests

DF 65073

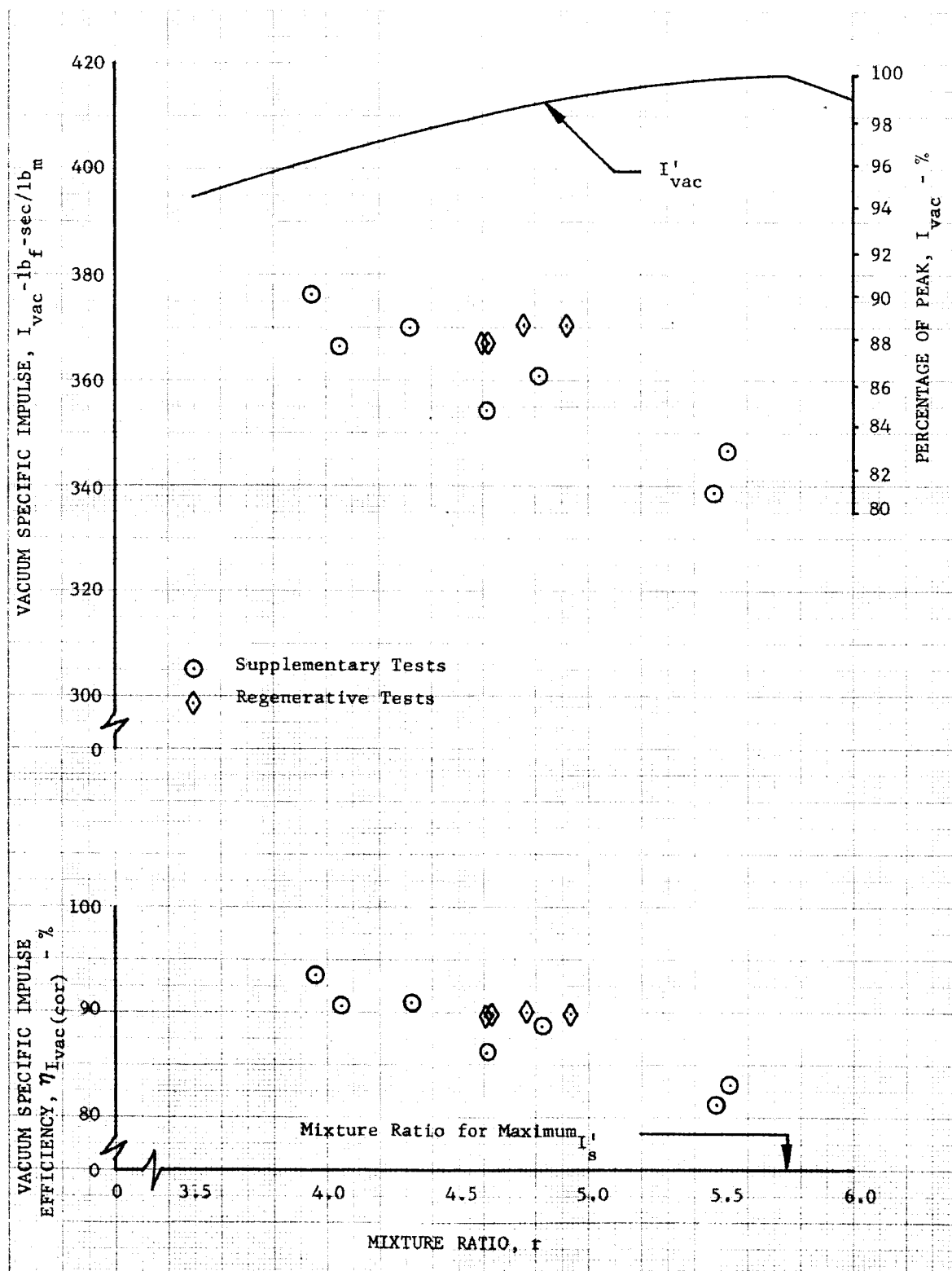


Figure 57. Estimated Vacuum Specific Impulse Data From Cooled Tests

DF 65074

C. ANALYSIS OF COOLING RESULTS

Of the seven supplementary and regeneratively cooled tests conducted, four tests resulted in some degree of damage to the cooling jacket tubes. Except for test 7 CA, all of the tube failures apparently occurred during steady-state operation at mixture ratios above 4.9. Figures 58 and 59 show the predicted combustion side wall temperature profiles based on measured gas film coefficients from the uncooled altitude tests. The peak wall temperatures are almost exactly the same as those predicted based on a constant 80% of the Bartz theoretical values as previously shown in figures 11 and 12, and provide from 350° to 400°R wall margin. These results provide no indication of the cause of the tube burnouts incurred at high mixture ratio.

One possible cause of tube burnout was considered to be flaking-off of the carbon layer during steady-state operation. Figure 60 shows the predicted effect of carbon flake-off for a mixture ratio of 4.5 at the throat and at two axial locations in the combustion chamber. It can be seen that carbon flake-off at the throat would produce a local increase in wall temperature of approximately 900°R. This would increase the wall temperature to above burnout point at the throat. Figure 61 shows the effect of carbon flake-off at the throat for a mixture ratio of 5.6. The effect is shown to be less severe than at the lower mixture ratio because film boiling is nearly complete and the gas velocity is higher. Thus, local carbon flake-off is seen to provide a mechanism for the burnout; however, the predicted location of the burnout and the effect of mixture ratio on possible burnout are contradictory to the cooled test results.

Another possible contribution to tube burnout is condensation of carbon in the boundary layer. While the predicted equilibrium concentration of gaseous carbon in the exhaust products is small (i.e., on the order of 0.1 to 0.01 mole percent) the energy released in carbon condensation is extremely high (approximately 25,000 Btu/lb). Thus, under certain conditions condensation of carbon in the boundary layer could have an appreciable effect on heat transfer. Based on strictly equilibrium calculations, the increase in the chamber heat flux due to carbon condensation would be less than 5%; however, nonhomogeneous distribution of the reaction products could produce local effects wherein the concentration of gaseous carbon would be substantially in excess of theoretical equilibrium predictions. The measured heat flux data from the uncooled tests would include the effect of carbon condensation under equilibrium conditions; however, if carbon flake-off were to occur, the momentary increase in local heat flux to the bare wall could be magnified by a temporary increase in the rate of carbon condensation as the carbon layer reforms.

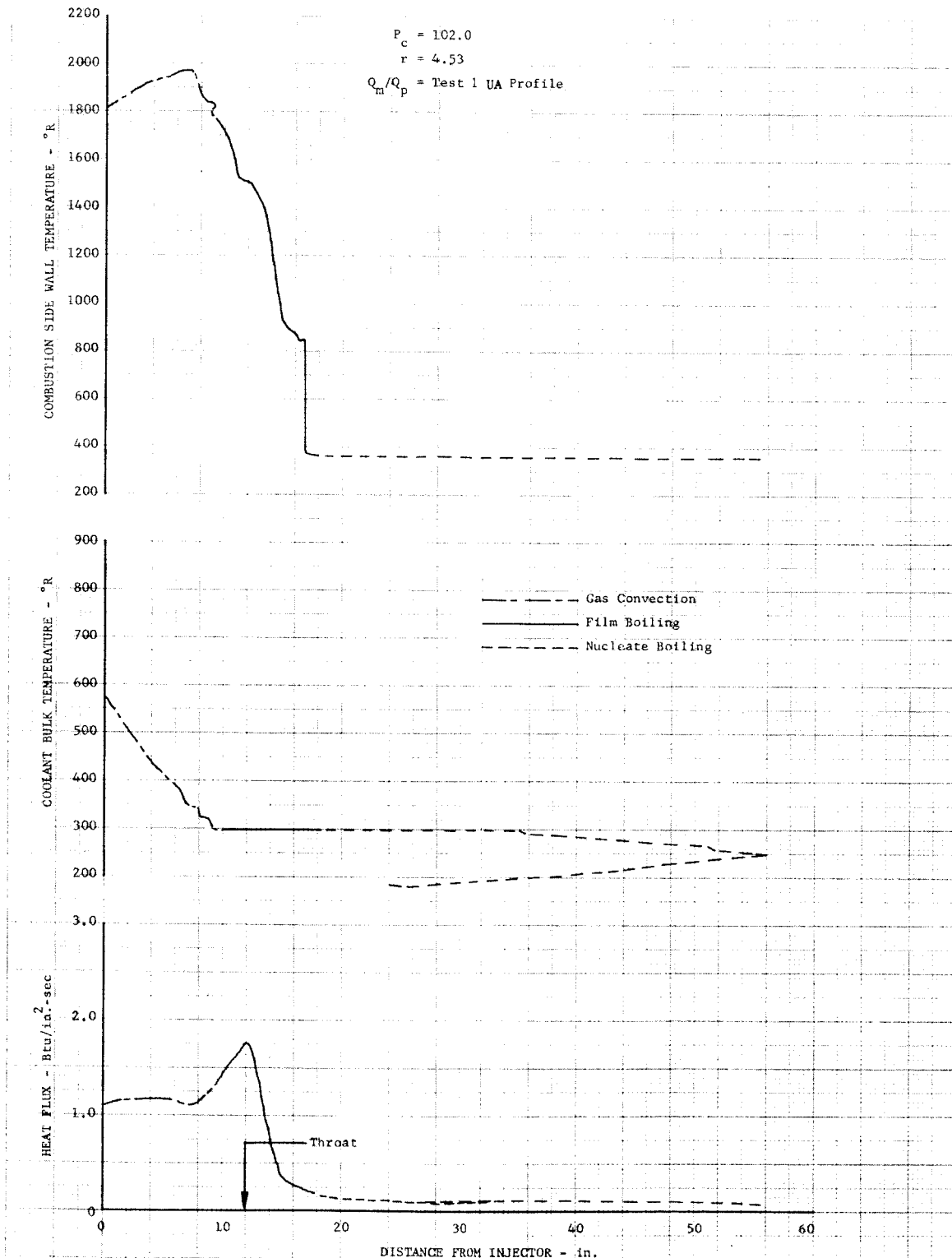


Figure 58. Predicted Regeneratively Cooled Chamber Condition
Based on Measured Uncooled Test Heat Flux Profile,
 $r = 4.53$

DF 65075

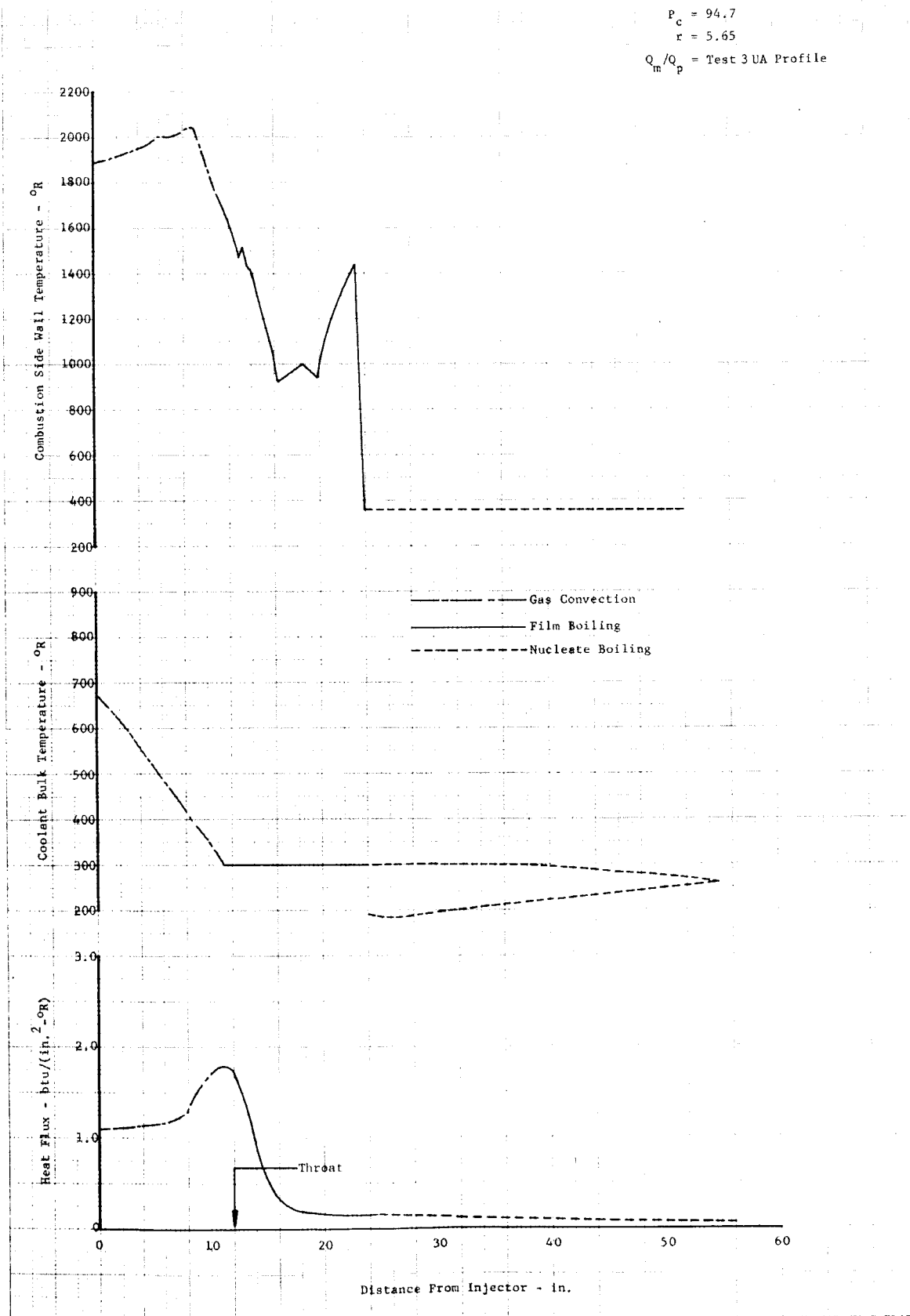


Figure 59. Predicted Regeneratively Cooled Chamber
Condition Based on Measured Uncooled
Test Heat Flux Profile, $r = 5.65$

DF 65076

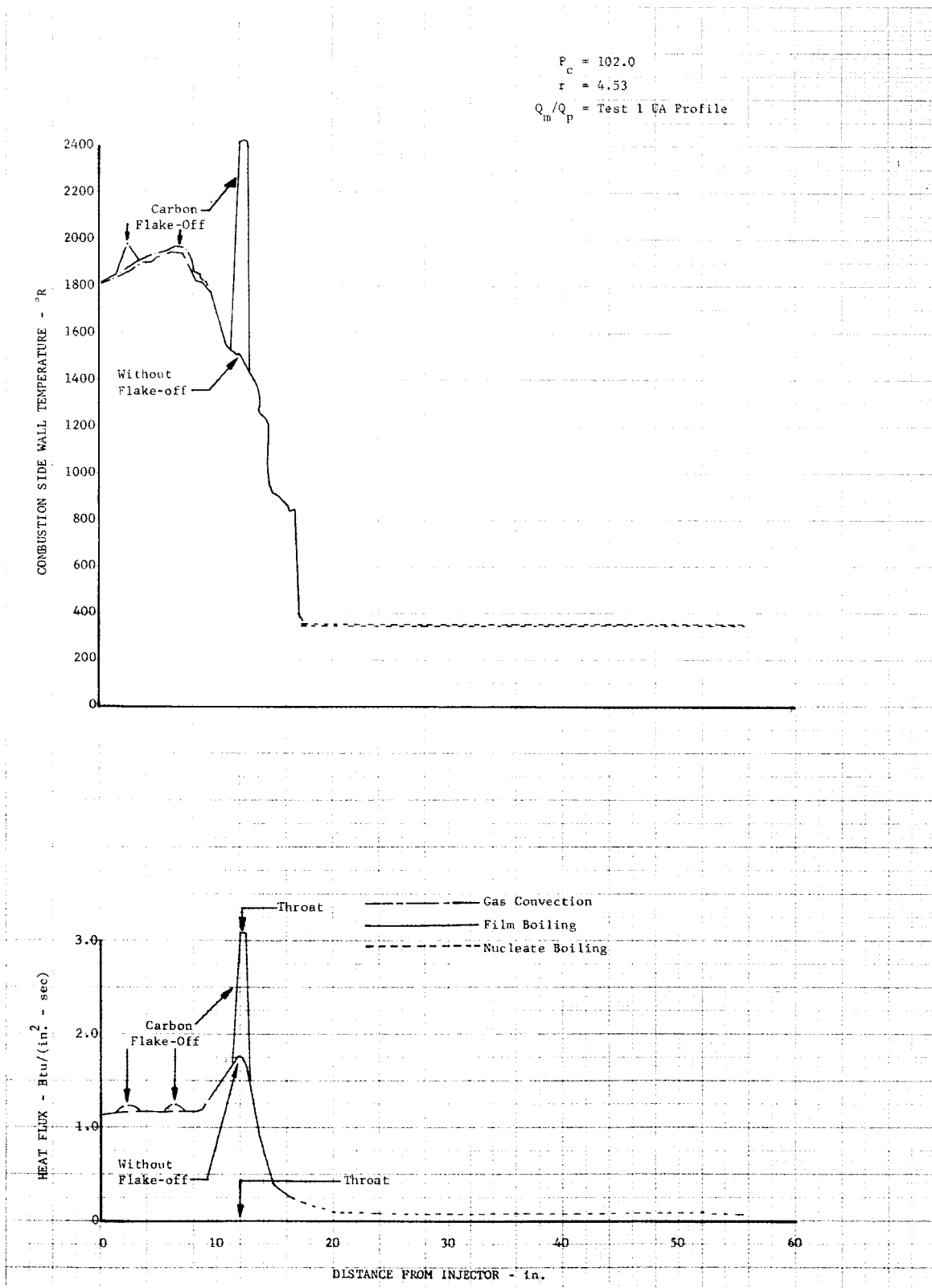


Figure 60. Effect of Carbon Flake-Off on Chamber Cooling, $r = 4.53$

DF 65077

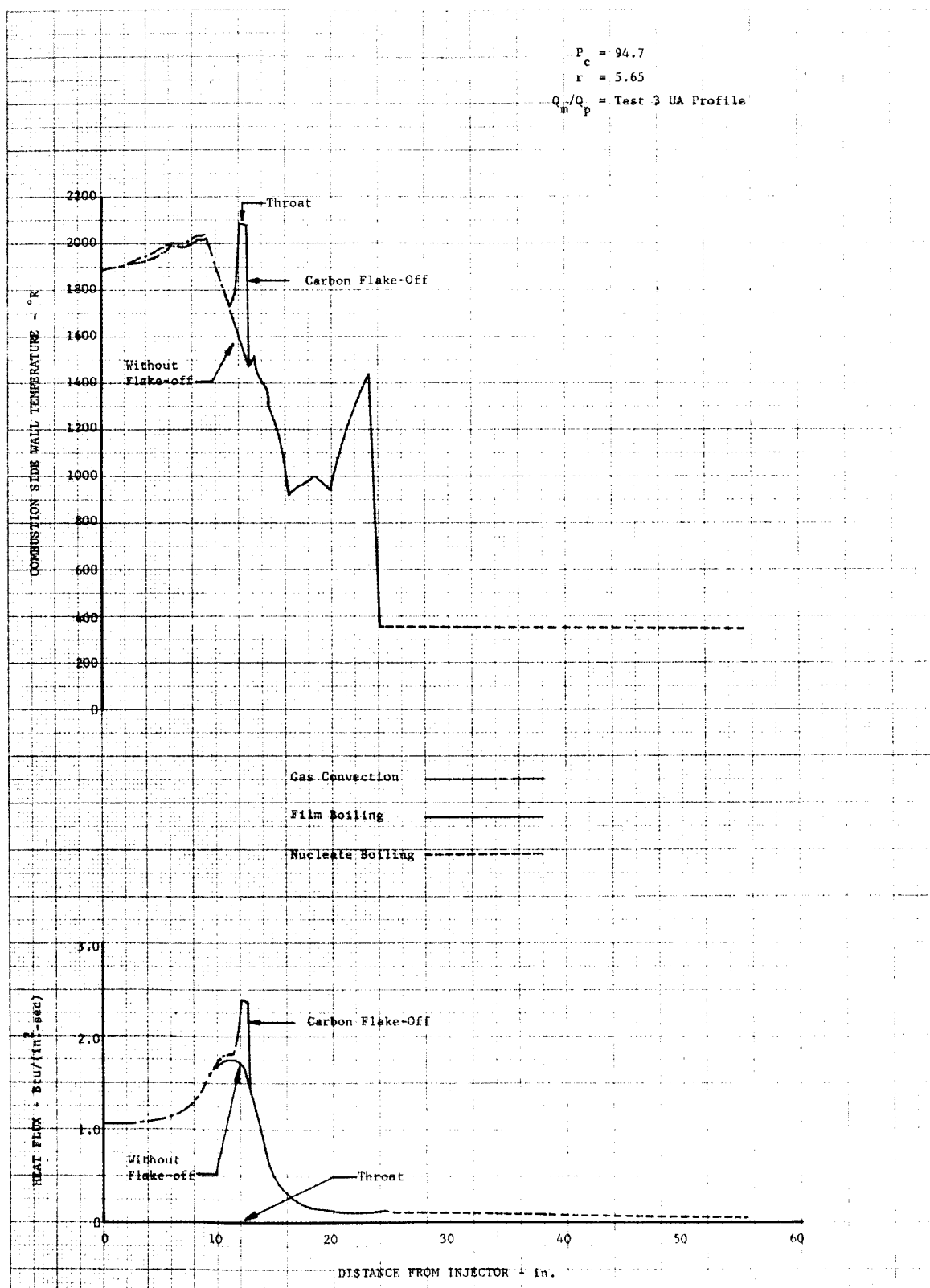


Figure 61. Effect of Carbon Flake-Off on Chamber Cooling, $r = 5.65$

DF 65078

During the start transient, the heat flux to the combustion chamber walls is low, while the coolant flowrate is near the steady-state value. Under these conditions the film boiling region shifts further toward the combustion chamber. An analysis was conducted to determine if under these conditions, film boiling in the combustion chamber could result in tube burnout. This was accomplished by using the steady-state coolant flowrate and reducing the heat flux below the experimental steady-state values. The results, summarized in figure 62, showed no start transient temperature overshoots were to be expected. At 25% of the steady-state heat flux the entire combustion chamber was operating in the film boiling region, but the peak wall temperature was only 58% (1190°R) of the predicted steady-state maximum.

As indicated, several mechanisms regarding the cause of the high mixture ratio tube failure may be postulated, but no completely satisfactory cause may be definitely established. The most likely cause appears to stem from the combined effects of nonuniform heat circumferential heat flux, carbon layer flake-off, and carbon condensation. The correlation of the tube failure with high mixture ratio operation would indicate that the tendency toward carbon flake-off increases with increasing mixture ratio.

While the tube failures at high mixture ratio indicate an area of inadequate knowledge, these failures should not be overemphasized with regard to the applicability of bulk-boiling cooling with methane. In a practical sense methane bulk boiling cooling has been shown to be entirely feasible. Fluid dynamic stability was achieved on all tests, and a satisfactory solution to the start transient control problems was found. Most important, completely satisfactory cooling was demonstrated over the mixture ratio range which provided maximum vacuum specific impulse, i.e., over 380 seconds between a mixture ratio of 4.1 and 4.9.

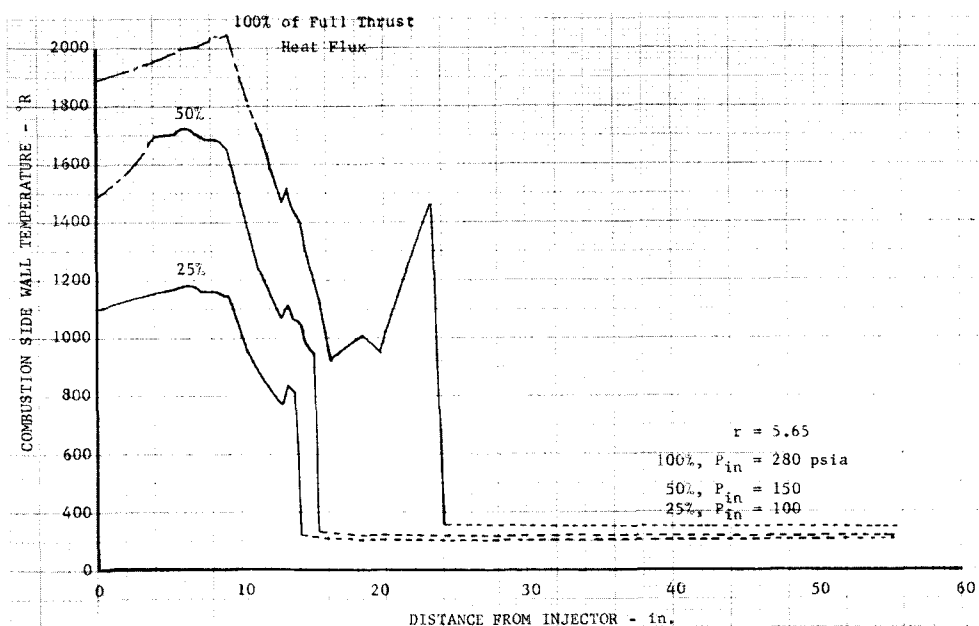


Figure 62. Predicted Start Transient Wall Temperature

DF 65079

SECTION VIII

APPLICABILITY OF METHANE BULK BOILING COOLING — TASK I

A. RANGE OF CONDITIONS

Regenerative cooling with bulk boiling methane offers the advantages of higher specific impulse than provided by other hydrocarbons (i.e., those suited for conventional regenerative cooling), and simpler, lighter weight thrust chamber construction and higher specific impulse than encountered with methane using transpiration or ablation cooling. To complement the experimental investigation at 100-psia chamber pressure and 5000-lb vacuum thrust, a parametric heat transfer study was conducted to establish the chamber pressure and thrust ranges over which regenerative cooling with methane is feasible. Jacket pressure drops and coolant outlet temperatures were determined for the range of conditions shown in table 13.

TABLE 13. RANGE OF CONDITIONS FOR PARAMETRIC STUDY

Propellants	Flox/Methane
Vacuum Thrust	1000 to 20,000 lb
Chamber Pressure (P_c)	100 to 250 psia
Mixture Ratio (r)	3.75 to 5.75
Fuel Inlet Temperature	173°R (FP + 10°R)
Area Ratio	40
Combustion Efficiency (η_c^*)	96%
Characteristic Length, L^*	30 in.
Area Ratio	40
Nozzle Contour	Minimum surface area perfect bell

The assumptions upon which the calculation was based are summarized below.

1. The heat exchangers were constructed of bundles of double tapered round tubes using a pass-and-one-half coolant path.
2. Tubes were sized to provide the minimum pressure drop consistent with a maximum wall temperature of 2400°R. This temperature limit is representative of advanced tube materials such as Hastelloy X or Haynes 25.
3. Based on current manufacturing limitations the minimum tube diameter was set at 0.040 in. ID and the minimum wall thickness at 0.010 in.

4. The combustion gas film coefficients were reduced to 80% of the Bartz theoretical values. This reduction is due to carbon deposits on the chamber wall and is slightly higher than the reduction measured with the coaxial injector test program, but typical of what would be expected in a developed engine.
5. Based on typical injector design practice the following injector inlet pressures (heat exchanger outlet pressures) were assumed:

Chamber Pressure, psia	Jacket Outlet Pressure, psia
100	175
175	275
250	375

The equations employed in the study were identical to those given in Reference 1 except for the saturated film boiling Nussult number. The equation used was,

$$Nu = 0.023(Re)_t^{0.8}(Pr)_t^{0.4}(\rho_b/\rho_g)^{0.5}$$

This equation was used instead of the one reported in Reference 1 because of the following: (1) the equation better correlates the saturated film-boiling data over the range of Reynolds numbers of interest to this study and (2) it permits a smooth transition when calculating heat transfer coefficients in the film-boiling and gas-phase regimes.

B. PREDICTED RANGE OF APPLICABILITY

Figures 63 through 65 present coolant pressure drop, coolant discharge temperature, and minimum tube diameter for the range of conditions of interest. The coolant pressure drop increases with increased chamber pressure. This occurs because the heat flux increases with chamber pressure, thus requiring higher coolant velocities with the accompanying higher pressure drop. In all cases the coolant discharge temperature is above the saturation temperature, indicating that bulk boiling occurred in the jacket. As would be expected, the assumed level of heat flux has a marked effect on the coolant pressure drop. At the lower thrust limit shown for 100-psia chamber pressure (1000-lb thrust, $r = 5.75$) the required coolant pressure drop decreases from 66 psi at an assumed 80% of the Bartz film coefficients to 36 psi at 60%. The 80% level is a maximum for the assumed limits of 0.040 in. minimum tube diameter and 2400°R maximum wall temperature. For comparison, however, this case was run using 100% of the Bartz coefficients with the 0.040 in. minimum diameter tubes. The maximum wall temperature for this condition was 2545°R and the pressure drop increased to 82 psi.

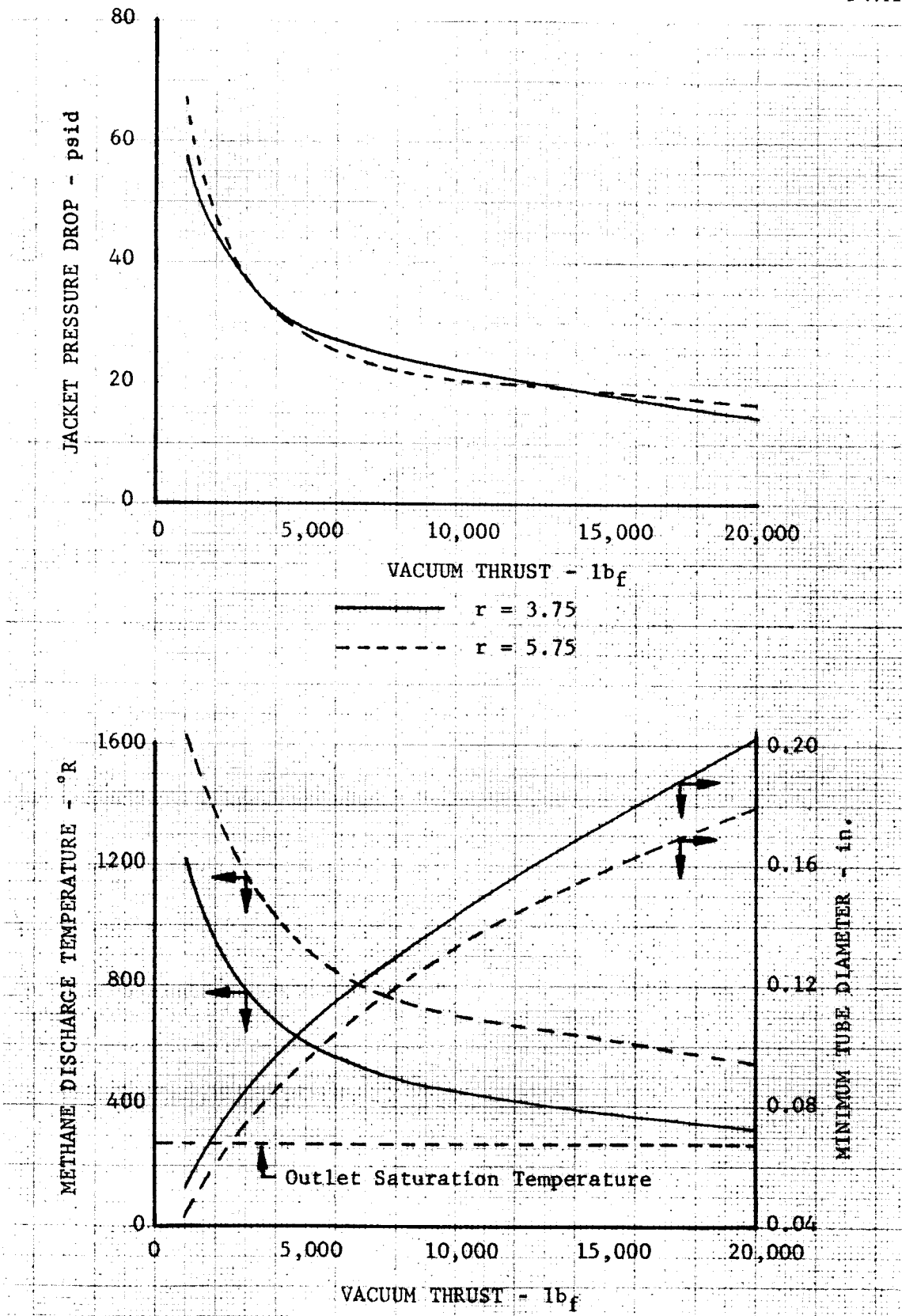


Figure 63. Results of Parametric Heat Transfer Analysis:
Chamber Pressure = 100 psia

DF 66878

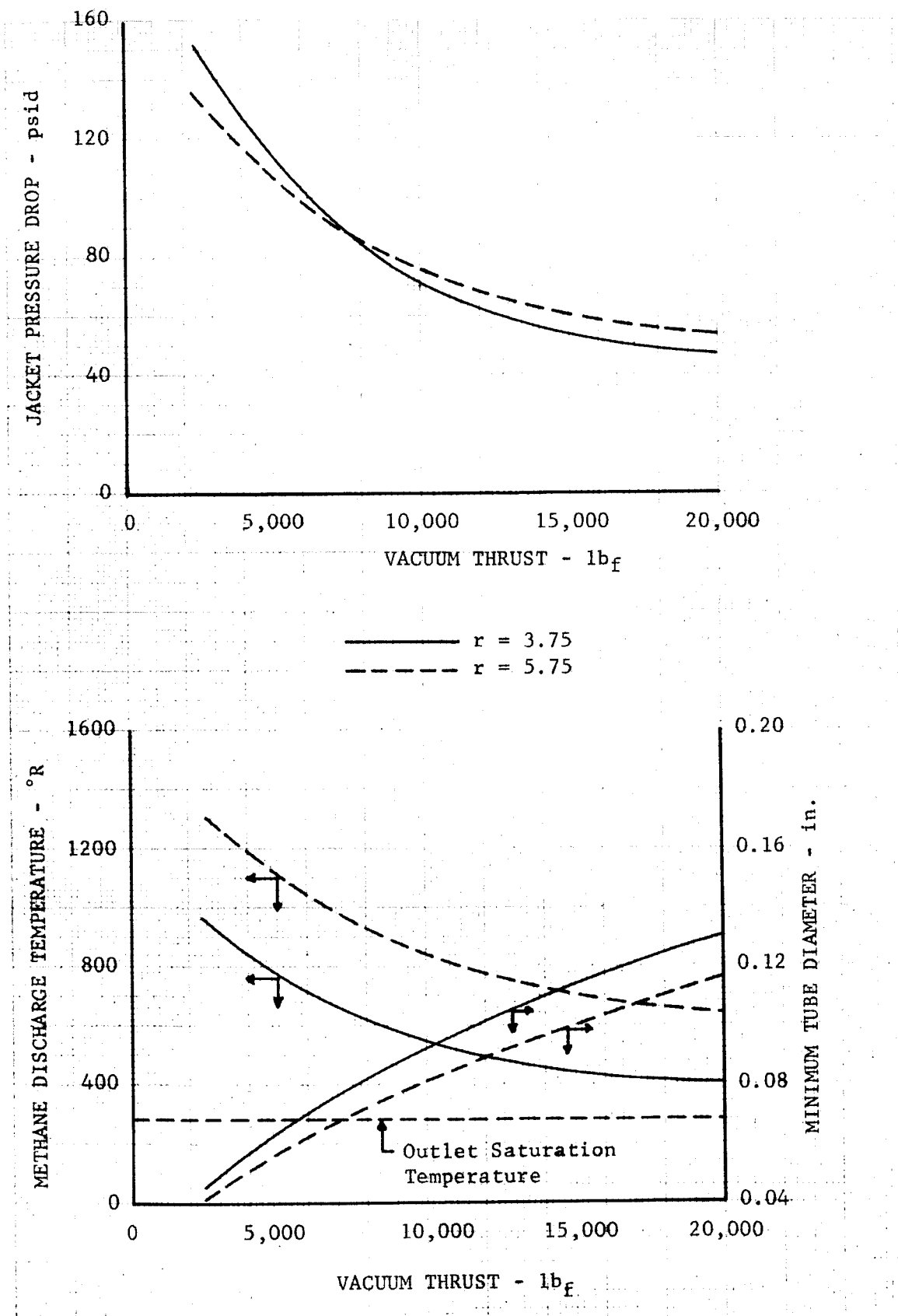


Figure 64. Results of Parametric Heat Transfer Analysis:
Chamber Pressure = 175 psia

DF 66879

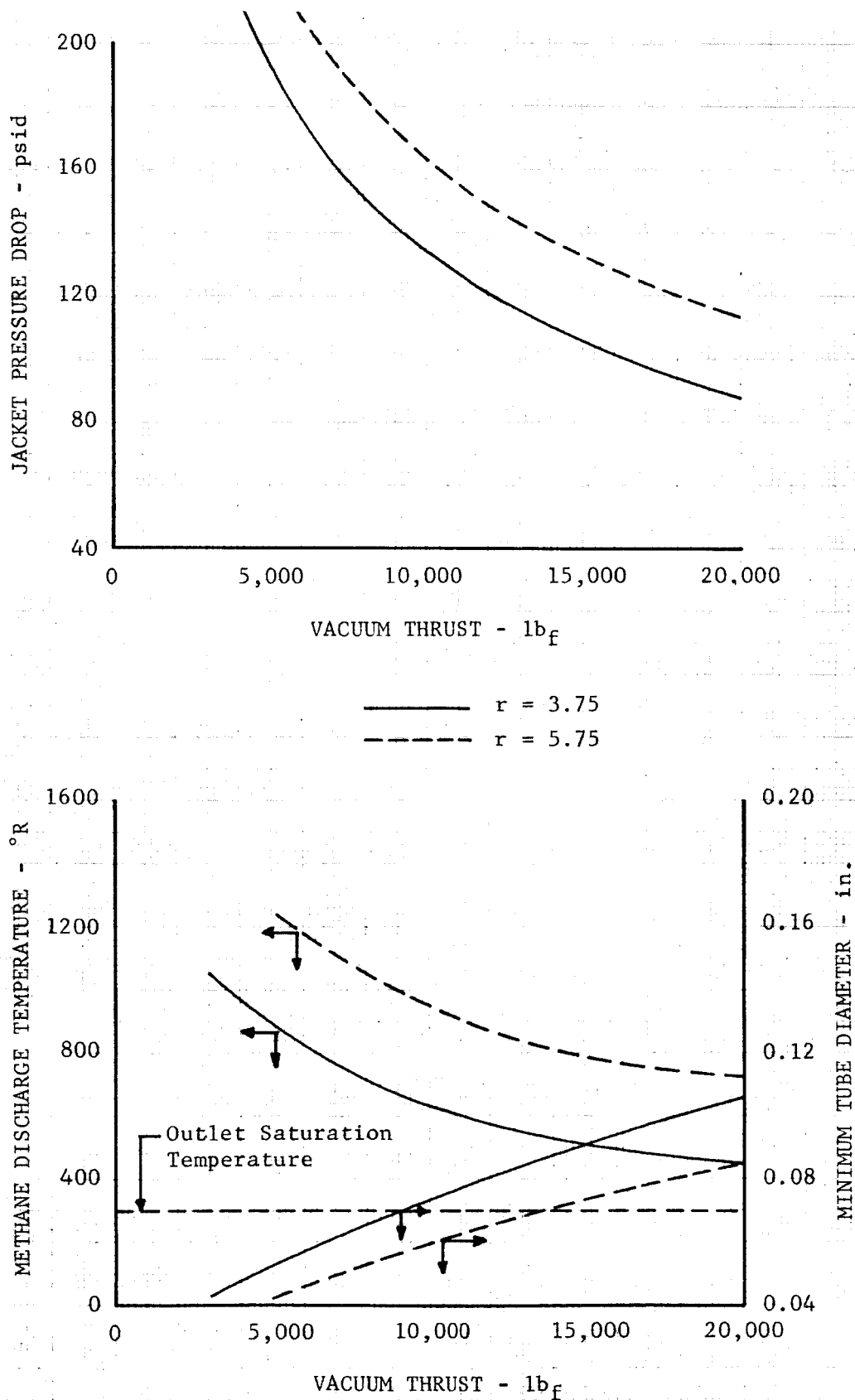


Figure 65. Results of Parametric Heat Transfer Analysis:
Chamber Pressure = 250 psia

DF 66880

Figure 66 shows the thrust/chamber pressure cooling limits for operation at a mixture ratio of 5.75. Based on the minimum tube diameter constraint, regenerative cooling is feasible to below 5000-lb thrust at chamber pressures up to 250 psia; however, at these conditions the coolant pressure drops are unrealistically high. The lower line on figure 66 shows the limits based on pressure drops more representative of engine design practice.

The limits predicted in figures 63 through 66 are based on conventional tube-type construction and existing tube fabrication technology. The limits could probably be exceeded through the use of advanced chamber fabrication technology. Also the percent of theoretical heat flux is conservatively set at 80%, slightly above most current experience. Moderate injector development or the addition of film cooling would be expected to provide lower heat fluxes, thereby further increasing the range of applicability. Based on the experimental results of the cooled test program (Section VII) some cooling problems might be expected above a mixture ratio of 5.0; however, the experimental performance data shown in Section VI indicate that operation at these high mixture ratios is not desirable for maximum performance.

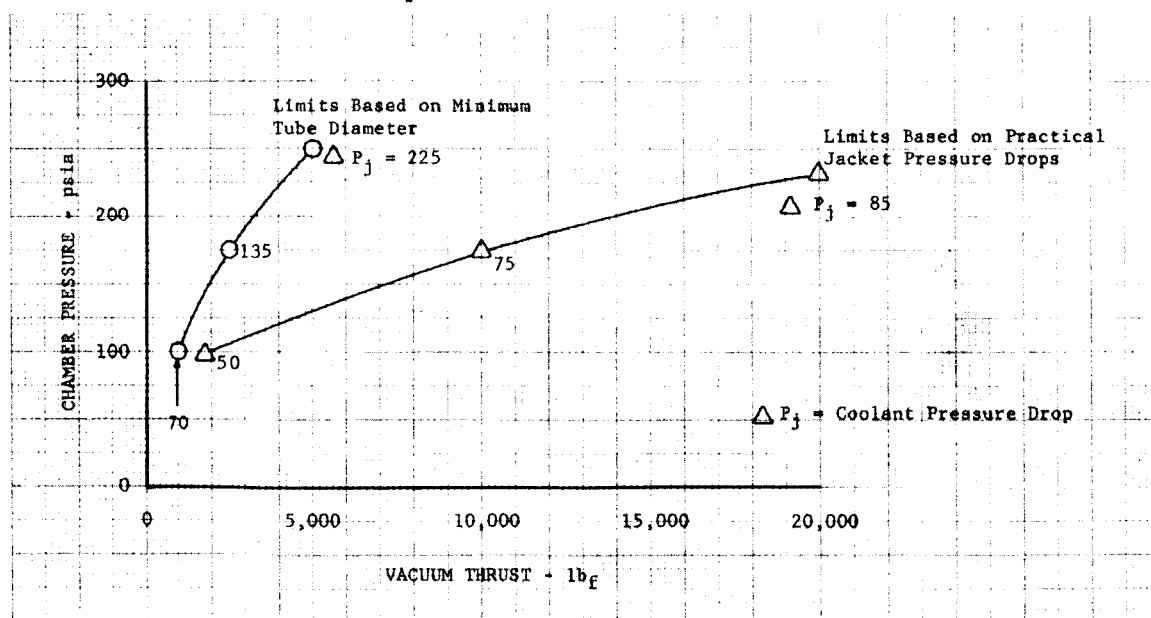


Figure 66. Flox/Methane Regenerative Cooling Limits
for Mixture Ratio of 5.75

DF 68103

SECTION IX

REFERENCES

1. "Investigation of Light Hydrocarbon Fuels With Flox Mixtures as Liquid Rocket Propellants — Final Report," Pratt & Whitney Aircraft, FR-1443, Contract NAS3-4195, NASA CR-54445, 1 September 1965.
2. "Investigation of Light Hydrocarbon Fuels With Fluorine-Oxygen Mixtures as Liquid Rocket Propellants — Final Report," Pratt & Whitney Aircraft, FR-2227, Contract NAS3-6296, NASA CR-72147, 15 September 1967.
3. Bartz, D. R., "A Simple Equation for Rapid Estimation of Rocket Convective Heat Transfer Coefficients," *Jet Propulsion*, January 1957.
4. "Flox/Methane Pump-Fed Engine Study — Final Report," Pratt & Whitney Aircraft Contract NAS3-7950, to be published.
5. "Injector Design Criteria for High Energy Space Storable Propellants," Pratt & Whitney Aircraft, SMR FR-2623, 28 November 1967.
6. Priem, R. J. and M. F. Heidman, "Propellant Vaporization as a Design Criteria for Rocket-Engine Combustion Chambers," NASA TR-R-67, 1960.
7. "System Dynamics Program for Liquid Hydrogen Rocket Engines Final Report," Pratt & Whitney Aircraft, FR-1527, Contract NAS8-5623, 29 October 1965.
8. "Research on a Hydrogen-Fluorine Propulsion System — Final Report," Pratt & Whitney Aircraft, FR-1585, Contract NASw-754, NASA CR-72074, 21 October 1966 (Confidential).

APPENDIX A

DISTRIBUTION LIST

National Aeronautics and Space Administration Lewis Research Center 21000 Brookpark Road Cleveland, Ohio 44135		National Aeronautics and Space Administration Langley Research Center Langley Station Hampton, Virginia 23365	
Attn: Contracting Officer, MS 500-210	1	Attn: Library	1
Liquid Rocket Technology Branch, MS 500-209	8	National Aeronautics and Space Administration Manned Spacecraft Center Houston, Texas 77001	
Technical Report Control Office, MS 5-5	1	Attn: Library	1
Technology Utilization Office, MS 3-16	1	H. J. Brasseaux, PESD-Propulsion	1
AFSC Liaison Office, MS 4-1	2	W. Hammock	1
D. L. Nored, MS 500-209	1		
Library	2	National Aeronautics and Space Administration George C. Marshall Space Flight Center Huntsville, Alabama 35812	
Harold Valentine, MS 501-2	1	Attn: Library	1
Office of Reliability & Quality Assurance, MS 500-203	1	Keith Chandler, R-P&VE-PA	1
Rudolph A. Duscha, MS 500-209	1	Lee W. Jones, R-PVE-PAS	1
E. W. Conrad, MS 100-1	1		
Larry H. Gordon, MS 500-209	1	National Aeronautics and Space Administration Western Operations Office 150 Pico Boulevard Santa Monica, California 90406	
National Aeronautics and Space Administration Washington, D. C. 20546		Attn: Library	1
Attn: Code MT	1	Jet Propulsion Laboratory 4800 Oak Grove Drive Pasadena, California 91103	
RPX	2	Attn: Library	1
RPL	2	W. B. Powell	1
SV	1		
Robert F. Schmidt	1	Office of the Director of Defense Research & Engineering Washington, D. C. 20301	
RPX, Frank W. Stephenson, Jr.	1	Attn: Dr. H. W. Schulz, Office of Asst. Dir. (Chem. Technology)	1
Scientific and Technical Information Facility P. O. Box 33 College Park, Maryland 20740		Defense Documentation Center Cameron Station Alexandria, Virginia 22314	
Attn: NASA Representative	6	RTD(RTNP) Bolling Air Force Base Washington, D. C. 20332	1
Code CRT		Arnold Engineering Development Center Air Force Systems Command Tullahoma, Tennessee 37389	
National Aeronautics and Space Administration Ames Research Center Moffett Field, California 94035		Attn: AEOIM	1
Attn: Library	1	Advanced Research Projects Agency Washington, D. C. 20525	
C. A. Syvertson	1	Attn: D. E. Mock	1
National Aeronautics and Space Administration Flight Research Center P. O. Box 273 Edwards, California 93523		Aeronautical Systems Division Air Force Systems Command Wright-Patterson Air Force Base Dayton, Ohio	
Attn: Library	1	Attn: D. L. Schmidt,	1
National Aeronautics and Space Administration Goddard Space Flight Center Greenbelt, Maryland 20771		Code ASRCNC-2	
Attn: Library	1		
C. R. Gunn, Delta	1		
National Aeronautics and Space Administration John F. Kennedy Space Center Cocoa Beach, Florida 32931			
Attn: Library	1		
R. A. Raffaelli	1		

Pratt & Whitney Aircraft

PWA FR-2872

Air Force Missile Test Center Patrick Air Force Base, Florida Attn: L. J. Ullian	1	Air Force Aero Propulsion Laboratory Research & Technology Division Air Force Systems Command United States Air Force Wright-Patterson AFB, Ohio 45433 Attn: APRP (C. M. Donaldson)	1
Air Force Systems Command (SCLT/Capt. S. W. Bowen)	1		
Andrews Air Force Base Washington, D. C. 20332	1	Aerojet-General Corporation P. O. Box 296 Azusa, California 91703 Attn: Librarian	1
Air Force Rocket Propulsion Laboratory (RPR) Edwards, California 93523	1		
Air Force Rocket Propulsion Laboratory (RPM) Edwards, California 93523	1	Aerojet-General Corporation 11711 South Woodruff Avenue Downey, California 90241 Attn: F. M. West, Chief Librarian	1
Air Force Office of Scientific Research Washington, D. C. 20333 Attn: SREP, Dr. J. F. Masi	1		
Office of Research Analyses (OAR) Holloman Air Force Base, New Mexico 88330 Attn: RRRT	1	Aerojet-General Corporation P. O. Box 1947 Sacramento, California 95809 Attn: Technical Library 2484-2015A	1
Maj. R. E. Brocken, Code MDGRT	1	Dr. C. M. Beighley	1
U. S. Air Force Washington 25, D. C. Attn: Col. C. K. Stambaugh, Code AFRST	1	D. T. Bedsole	1
Commanding Officer U. S. Army Research Office (Durham) Box CM, Duke Station Durham, North Carolina 27706	1	Aeronutronic Division of Philco Corporation Ford Road Newport Beach, California 92600 Attn: Dr. L. H. Linder, Manager	1
U. S. Army Missile Command Redstone Scientific Information Center Redstone Arsenal, Alabama 35808 Attn: Chief, Document Section	1	Technical Information Department	1
Dr. W. Wharton	1		
Bureau of Naval Weapons Department of the Navy Washington, D. C. Attn: J. Kay, Code RTMS-41	1	Aeroprojects, Incorporated 310 East Rosedale Avenue West Chester, Pennsylvania 19380 Attn: C. D. McKinney	1
Commander U. S. Naval Missile Center Point Mugu, California 93041 Attn: Technical Library	1		
Commander U. S. Naval Ordnance Test Station China Lake, California 93557 Attn: Code 45	1	Aerospace Corporation P. O. Box 95085 Los Angeles, California 90045 Attn: Library	1
Code 753	1		
W. F. Thorm, Code 4562	1	Arthur D. Little, Inc. Acorn Park Cambridge 40, Massachusetts Attn: A. C. Tobey	1
Commanding Officer Office of Naval Research 1030 E. Green Street Pasadena, California 91101	1		
Director (Code 6180) U. S. Naval Research Laboratory Washington, D. C. 20390 Attn: H. W. Carhart	1	Astropower, Incorporated Subs. of Douglas Aircraft Company 2968 Randolph Avenue Costa Mesa, California Attn: Dr. George Moc Director, Research	1
Picatinny Arsenal Dover, New Jersey Attn: I. Forsten, Chief	1	Astrosystems, Incorporated 1275 Bloomfield Avenue Caldwell Township, New Jersey Attn: A. Mendenhall	1
Liquid Propulsion Laboratory	1	ARO, Incorporated Arnold Engineering Development Center Arnold AF Station, Tennessee 37389 Attn: Dr. B. H. Goethert Chief Scientist	1

Pratt & Whitney Aircraft
PWA FR-2872

Atlantic Research Corporation Shirley Highway & Edsall Road Alexandria, Virginia 22314 Attn: A. Scurlock Security Office for Library	1 1	Fairchild Stratos Corporation Aircraft Missiles Division Hagerstown, Maryland Attn: Library	1
Battelle Memorial Institute 505 King Avenue Columbus, Ohio 43201 Attn: Report Library, Room 6A	1	General Dynamics/Astronautics P. O. Box 1128 San Diego, California 92112 Attn: F. Dore Library & Information Services (128-00)	1 1
Beech Aircraft Corporation Boulder Facility Box 631 Boulder, Colorado Attn: J. H. Rodgers	1	General Electric Company Re-Entry Systems Department P. O. Box 8555 Philadelphia, Pennsylvania 19101 Attn: F. E. Schultz	1
Bell Aerosystems, Inc. Box 1 Buffalo, New York 14205 Attn: T. Reinhardt W. M. Smith	1 1	General Electric Company Flight Propulsion Lab. Department Cincinnati 15, Ohio Attn: D. Suichu	1
Bendix Systems Division Bendix Corporation Ann Arbor, Michigan Attn: John M. Bureger	1	Grumman Aircraft Engineering Corporation Bethpage, Long Island, New York Attn: Joseph Gavin	1
The Boeing Company Aero Space Division P. O. Box 3707 Seattle, Washington 98124 Attn: Ruth E. Peerenboom (1190) J. D. Alexander	1 1	Hercules Powder Company Allegheny Ballistics Laboratory P. O. Box 210 Cumberland, Maryland 21501 Attn: Library	1
Chemical Propulsion Information Agency Applied Physics Laboratory 8621 Georgia Avenue Silver Spring, Maryland 20910	1	IIT Research Institute Technology Center Chicago, Illinois 60616 Attn: Library	1
Chrysler Corporation Missile Division Warren, Michigan Attn: John Gates	1	Kidde Aero-Space Division Walter Kidde & Company, Inc. 675 Main Street Belleville 9, New Jersey Attn: R. J. Hanville, Director of Research Engineering	1
Chrysler Corporation Space Division New Orleans, Louisiana Attn: Librarian	1	Lockheed Missiles & Space Company P. O. Box 504 Sunnyvale, California Attn: Y. C. Lee, Power Systems R&D Technical Information Center	1 1
Curtiss-Wright Corporation Wright Aeronautical Division Woodridge, New Jersey Attn: G. Kelley	1	Lockheed-California Company 10445 Glen Oaks Blvd., Pacoima, California Attn: Library	1
University of Denver Denver Research Institute P. O. Box 10127 Denver, Colorado 80210 Attn: Security Office	1	Lockheed Propulsion Company P. O. Box 111 Redlands, California 92374 Attn: Miss Belle Berlad, Librarian H. L. Thackwell	1 1
Douglas Aircraft Company, Inc. Santa Monica Division 3000 Ocean Park Blvd. Santa Monica, California 90405 Attn: J. L. Waisman R. W. Hallet G. W. Burge	1 1 1	Lockheed Missiles & Space Company Propulsion Engineering Division (D.55-11) 1111 Lockheed Way Sunnyvale, California 94087	1 1

Pratt & Whitney Aircraft

PWA FR-2872

Marquardt Corporation 16555 Saticoy Street Box 2013 — South Annex Van Nuys, California 91404 Attn: Librarian W. D. Boardman, Jr.	1 1	Stanford Research Institute 333 Ravenswood Avenue Menlo Park, California 94025 Attn: Thor Smith	1
Martin-Marietta Corporation Martin Division Baltimore 3, Maryland Attn: John Calathes (3214)	1	Texaco Experiment, Incorporated P. O. Box I-T Richmond, Virginia 23202 Attn: E. B. Monteath Librarian	1 1
McDonnell Aircraft Corporation P. O. Box 6101 Lambert Field, Missouri Attn: R. A. Herzmark	1	Thiokol Chemical Corporation Alpha Division, Huntsville Plant Huntsville, Alabama 35800 Attn: Technical Director	1
North American Aviation, Inc. Space & Information Systems Division 12214 Lakewood Boulevard Downey, California 90242 Attn: Technical Information Center, D/096-722 (AJ01) H. Storms	1 1	Thiokol Chemical Corporation Reaction Motors Division Denville, New Jersey 07834 Attn: A. Sherman Librarian	1 1
Northrop Space Laboratories 1001 East Broadway Hawthorne, California Attn: Dr. William Howard	1	Thiokol Chemical Corporation Redstone Division Huntsville, Alabama Attn: John Goodloe	1
Purdue University Lafayette, Indiana 47907 Attn: Technical Librarian	1	TRW Systems, Incorporated 1 Space Park Redondo Beach, California 90200 Attn: G. W. Elverum STL Tech. Lib. Doc. Acquisitions H. L. Burge	1 1 1
Radio Corporation of America Astro-Electronics Division Defense Electronic Products Princeton, New Jersey Attn: S. Fairweather	1	TRW, Incorporated TAPCO Division 23555 Euclid Avenue Cleveland, Ohio 44117 Attn: P. T. Angell	1
Republic Aviation Corporation Farmingdale, Long Island New York Attn: Dr. William O'Donnell	1	United Aircraft Corporation Corporation Library 400 Main Street East Hartford, Connecticut 06118 Attn: Dr. David Rix Erle Martin	1 1
Rocket Research Corporation 520 South Portland Street Seattle, Washington 98108	1	United Aircraft Corporation Pratt & Whitney Division Florida Research & Development Center P. O. Box 2691 West Palm Beach, Florida 33402 Attn: R. J. Coar Library	1 1
Rocketdyne Division of North American Aviation, Inc. 6633 Canoga Avenue Canoga Park, California 91304 Attn: Library, Department 596-306 S. Clapp, Research Dept.	1 1	United Aircraft Corporation United Technology Center P. O. Box 358 Sunnyvale, California 94088 Attn: Librarian	1
Rohm and Haas Company Redstone Arsenal Research Division Huntsville, Alabama 35808 Attn: Librarian	1	Vought Astronautics Box 5907 Dallas 22, Texas Attn: Warren C. Trent	1